
Doctoral Dissertations

Student Theses and Dissertations

Spring 2018

Research on additive manufacturing of metallic glass alloy

Yiyu Shen

Follow this and additional works at: https://scholarsmine.mst.edu/doctoral_dissertations



Part of the [Mechanical Engineering Commons](#)

Department: **Mechanical and Aerospace Engineering**

Recommended Citation

Shen, Yiyu, "Research on additive manufacturing of metallic glass alloy" (2018). *Doctoral Dissertations*. 2688.

https://scholarsmine.mst.edu/doctoral_dissertations/2688

This thesis is brought to you by Scholars' Mine, a service of the Missouri S&T Library and Learning Resources. This work is protected by U. S. Copyright Law. Unauthorized use including reproduction for redistribution requires the permission of the copyright holder. For more information, please contact scholarsmine@mst.edu.

RESEARCH ON ADDITIVE MANUFACTURING OF METALLIC GLASS ALLOY

By

YIYU SHEN

A DISSERTATION

Presented to the Faculty of the Graduate School of the
MISSOURI UNIVERSITY OF SCIENCE AND TECHNOLOGY

In Partial Fulfillment of the Requirements for the Degree

DOCTOR OF PHILOSOPHY

in

MECHANICAL ENGINEERING

2018

Approved by:

Dr. Hai-Lung Tsai, Advisor

Dr. Ming Leu

Dr. Anthony Okafor

Dr. Heng Pan

Dr. John Story

© 2018

Yiyu Shen

All Right Reserved

PUBLICATION DISSERTATION OPTION

This dissertation consists of the following five articles that have been published or submitted for publication as follows:

PAPER I: Pages 9-45 have been published in Material and Design.

PAPER II: Pages 46-71 have been published in Journal of Non-Crystalline Solids.

PAPER III: Pages 72-104 are intended for submission in Journal of Materials Processing Technology.

PAPER IV: Pages 105-126 are intended for submission in Journal of Additive Manufacturing.

ABSTRACT

The required rapid cooling has limited the dimension of the Bulk Metallic glasses (BMGs) produced by traditional method, and hence has seriously limited their applications, despite their remarkable mechanical properties. In this present project, a detailed study is conducted on the methodology and understanding of manufacturing large Zr- based metallic glass part by laser based additive manufacturing technology, which breaks the size limitation. The first research issue proposes and develops a new additive manufacturing technology, named Laser-Foil-Printing (LFP). Sheet foils of LM105 ($Zr_{52.5}Ti_5Al_{10}Ni_{14.6}Cu_{17.9}$ (at. %)) metallic glass are used as feed stock. Fully amorphous 3D structures are successfully achieved. The second research issue focus on investigating the temperature evolution during laser-BMG interaction. By combining experimental measurement and mathematical model, the dynamic temperature field evolution during laser-BMG interaction is simulated. The developed model not only optimizes the LFP process, but also helps us in further understanding the fundamental crystallization mechanism during laser-BMG interaction. The crystalline phase evolution during laser-MG interaction is studied in the third research issue, using the classical nucleation theory (CNT). Combining with the temperature model, the volume fraction of crystallized BMG is calculated. The result successfully explains the observation of crystalline phase within both the fusion zone (FZ) and the heat-affected-zone (HAZ) of laser processed BMG. This thesis is a proven road map for developing metallic glass structures using additive manufacturing technology. The research results of this dissertation can benefit a wide range industry, such as 3D printing, material science, medical and aerospace.

ACKNOWLEDGMENTS

First and foremost, I am indebted to my advisor, Dr. Hai-lung Tsai, for everything that he has done for me during my PhD study at Missouri University of Science and Technology. Dr. Tsai led me to the area of Additive Manufacturing, and later suggested I get into the field of metallic glass alloy, which helped me get to where I am. He generously offered me tremendous freedom to explore the project and always supported me with solid fundamental knowledges. It has been a great honor to have worked with him.

I would also like to appreciate all the dissertation committee members, Dr. Ming C. Leu, Dr. A. Okafor, Dr. H. Pan, and Dr. J.G. Story, for their valuable comments and suggestions for me to complete my dissertation.

All the staff at Missouri S&T that once helped me are acknowledged. They are: Mr. Mitchell Cottrell, Mr. Brian Bullock, Mrs. Michele Warren, Dr. Jinging Qing, Dr. Clarissa Wisner, Dr. Eric Bohannon, and Dr. Jeremy Watts. Also, I would like to extend my appreciation to lab-mates in our group, Mr. Chen Chen, Ms. Yingqi Li, and Mr. Chia-Hung Hung, for all their help and support for both my research and life in Rolla.

The research work of the dissertation was supported by the Laser Based Manufacturing Lab at Missouri S&T. I am grateful for the financial support from the Department of Energy (Grant Number: DE-FE0012272), the UM Fast Track Funding Program, and the Intelligent System Center (ISC) of Missouri S&T.

Last but not the least, I thank my family for supporting me through my life: my father, Guohua Shen; and my mother, Youfang Li. I would also like to thank my girlfriend, Yi Yang. I would never have reached such an achievement without her love and help.

TABLE OF CONTENTS

	Page
PUBLICATION DISSERTATION OPTION	iii
ABSTRACT	iv
ACKNOWLEDGMENTS	v
LIST OF ILLUSTRATIONS	ix
LIST OF TABLES	xi
 SECTION	
1. INTRODUCTION	1
1.1. BACKGROUND	1
1.2. BULK METALLIC GLASS.....	2
1.3. ADDITIVE MANUFACTURING OF METALLIC GLASSES	3
1.4. RESEARCH OBJECTIVES	5
1.5. ORGANIZATION OF DISSERTATION	7
 PAPER	
I. 3D PRINTING OF LARGE, COMPLEX METALLIC GLASS STRUCTURES .	9
ABSTRACT	9
1. INTRODUCTION	10
2. THE LASER FOIL PRINTING (LFP) TECHNOLOGY	16
3. EXPERIMENT AND TESTING	20
3.1. LASER WELDING OF AMORPHOUS FOILS	20
3.2. SAMPLE AND TEST RESULTS	23
4. THERMAL ANALYSIS	29

4.1 MATHEMATICAL MODELING	29
4.2 COMPARISON AND ANALYSIS	30
4.3 COOLING AND HEATING RATES	31
5. AS-FABRICATED PARTS	36
6. CONCLUSIONS	38
ACKNOWLEDGEMENTS	39
REFERENCES	40
II. EVOLUTION OF CRYSTALLINE PHASE DURING LASER PROCESSING OF ZR-BASED METALLIC GLASS	46
ABSTRACT	46
1. INTRODUCTION	47
2. EXPERIMENTAL	49
3. RESULTS AND DISCUSSION	50
4. MODELING AND ANALYSIS	54
5. CONCLUSIONS	66
ACKNOWLEDGEMENTS	67
REFERENCES	68
III. THE EFFECT OF PRE-EXISTING NUCLEUS DENSITY ON CRYSTALLIZATION BEHAVIOR DURING LASER PROCESSING OF ZR-BASED METALLIC GLASS AND THE CORRESPONDING QUALITY FACTOR	72
ABSTRACT	72
1. INTRODUCTION	73
2. EXPERIMENTAL	76
3. EXPERIMENTS AND DISCUSSION	79

4. NUCLEATION KINETICS	82
5. RESULTS AND DISCUSSION	87
6. CRYSTALLINE EVOLUTION DURING LASER WELDING	96
7. CONCLUSIONS	100
ACKNOWLEDGEMENTS	101
REFERENCES.....	102
IV. THE EFFECT OF OVERLAP ON CRYSTALLIZATION OF BULK METALLIC GLASS DURING ADDITIVE MANUFACTURING	105
ABSTRACT	105
1. INTRODUCTION	106
2. EXPERIMENT	108
3. RESULTS	109
4. DISCUSSION	114
5. CONCLUSION	122
ACKNOWLEDGEMENTS	123
REFERENCES	124
SECTION	
2. CONCLUSION	127
BIBLIOGRAPHY	130
VITA	134

LIST OF ILLUSTRATIONS

PAPER I	Page
Figure 1. Schematic of the LFP process and the LFP system setups at the Laser-Based Manufacturing Lab, Missouri S&T.....	17
Figure 2. Top surface profile of laser welding of foils on plates	21
Figure 3. Cross-sections of laser weld beads	22
Figure 4. XRD test of printed sample	24
Figure 5. Optical microscope photos of the 10 mm thick test sample	26
Figure 6. DSC curves (heating rate = 20 °C/min) for the tested MG samples	26
Figure 7. Comparison of temperature history processed at laser power of 100 W and scan speed of 50 mm/s by experimental measurements and modeling	32
Figure 8. Plots of calculated temperature histories in the fusion zone, HAZ and un-affected zone for three cases	33
Figure 9. As-fabricated amorphous 3D parts by LFP	36
PAPER II	
Figure 1. Top and cross-sectional OM images of a laser scanned MG; inset in Fig. 1(b) is an SEM image (X 2500); $P = 100$ W and $v = 10$ mm/s	51
Figure 2. Cross-sectional OM images of laser-processed MG; $P = 100$ W, (a) $v = 30$ mm/s, (b) $v = 50$ mm/s, and (c) $v = 100$ mm/s	53
Figure 3. The calculated nucleation rate ($I(T)$) and crystalline growth rate ($U(T)$) as a function of temperature	57
Figure 4. Calculated evolution of volume fraction of crystalline phase in FZ	59
Figure 5. Calculated evolution of volume fraction of crystalline in HAZ at different depths	61
Figure 6. Calculated final volume fraction of crystalline as a function of depth at different laser scan speeds	63
Figure 7. Calculated maximum crystalline VF at different laser scan speeds	64

Figure 8. Calculated and measured depth of fusion zone (FZ) and thickness of heat-affected zone (HAZ) as a function of laser scan speed at a fixed laser power $P = 100$ W	64
--	----

PAPER III

Figure 1. (a) Experimental setup, (b) XRD test results for Sample 1 & 2, and (c) and (d) TEM images for Sample 1 and Sample 2 before the experiment	77
Figure 2. OM images of cross-sectional view of laser scanned a) Sample 1 and b) Sample 2.....	80
Figure 3. The calculated TTT curves of a “perfect” amorphous and “imperfect” amorphous LM105 with different pre-existing nucleus densities	88
Figure 4. The calculated quality factors Q_t and Q_x against pre-existing nucleus density for LM105 alloy	93
Figure 5. The effect of cooling rate on the quality factors and nucleus density during cast process from molten LM105	94
Figure 6. Calculated crystalline phase evolution in HAZ during laser welding	97

PAPER IV

Figure 1. OM photography on cross-section of laser welded LM105 sample with 200 W laser power and 20, 50, 100 and 200 mm/s scan speed	110
Figure 2. OM photography on cross-section of ‘multi- laser track’ on LM105 sample with 200 W laser power, 100 mm/s scan speed and different interspaces	111
Figure 3. Schematic experimental setup and the orientation of ‘multi- laser track’	111
Figure 4. Calculated temperature history with 200 W laser power and 20, 50, 100 and 200 mm/s scan speed	118
Figure 5. Calculated crystalline volume fraction in HAZ against laser scan speed	118
Figure 6. Calculated temperature history and corresponding crystallization for interspace of (a) 20 μm , (b) 200 μm and (c) 250 μm	120

LIST OF TABLES

	Page
PAPER I	
Table 1. Calculated heating/cooling rates at different locations	33
PAPER IV	
Table 1. Selected parameters applied in the experiments	108

1. INTRODUCTION

1.1. BACKGROUND

Bulk Metallic glasses (BMGs), or called amorphous metal alloys, has gain much research interest since they were discovered in 1960s because of their unique mechanical properties including extraordinary tensile strength, hardness and toughness [1–5]. These properties are inherited from disorder/randomness of atoms in the BMG that is different from crystallized metals. The main challenge of producing large metallic glass product is that a certain high cooling rate must be reached otherwise the alloy would be crystallized before it cools down to room temperature. This is named as the critical cooling rate (R_c). Limited by the law of heat transfer, during casting the material who is away from the surface cools less faster compare to that close to the outer surface. Thus this is equivalent to say that there is an upper limit of casting thickness. Additive manufacturing, however, build up the designed part layer by layer. Thus the cooling in additive manufacturing has also been separate into each individual layer. As a result, once the feasibility of AM for metallic glass in proved, the limitation of dimension in manufacturing metallic glass product can be broken through.

In this proposed project, we will develop a new additive manufacturing method specifically for BMG materials. It is named as Laser-Foil-Printing (LFP). Unlike the commercialized AM methods such as selective laser melting (SLM) who use metal powder as raw material, metal foil are used as feed stork in LFP which shows its significant advantages in manufacturing metallic glass products. LM105 ($Zr_{52.5}Ti_5Al_{10}Ni_{14.6}Cu_{17.9}$ (at. %)) metallic glass foils is used in this project. Zr- based metallic glass is a relatively new class of metallic glass family. It is recently commercialized due to its low critical cooling

rate ($R_c < 20$ K/s), high mechanical strength (yielding stress > 1500 MPa) and high corrosion/scratch resistance on surface.

1.2. BULK METALLIC GLASS

When a liquid is cooled from its melting temperature so quickly that the supercooled liquid does not have enough time to crystallize, a glass with an amorphous structure is formed. In this process, nucleation of crystalline phases can be suppressed by sufficiently high cooling rate. In 1950, Banner et al. [6] produced Ni-P metallic glass coating by electrophoretic deposition (EPD). In 1958, Turnbull and Cohen [7] reported the supercooled phenomenon of Hg liquid at 20% of its solidification temperature. This work laid the foundation for thermodynamic theory of BMG forming [8,9]. Another milestone in the BMG history came in 1960 when Klement et al. produced a 20 μm -thick BMG foil [10]. This was the first time the thickness of BMG reached a micro-level and made BMG useable for practical applications. Not a long after, electric transformer materials were gradually replaced by BMG foils due to their good thermal and magnetic properties.

While earlier researchers aimed at increasing R_c during BMG forming process, material scientists focused their attentions on improving the alloy's glass forming ability (GFA), the required condition for an alloy transition from liquid phase to amorphous solid phase, which usually includes critical cooling rate (R_c) and glass transition temperature (T_g). Since 1980s more than thousands of Zr-, Co-, Cu-, Pt-, Pd-, Ti-, Ni- or Fe-based amorphous alloys have been successfully developed, and R_c was decreased from approximately 10^6 K/s to less than 10 K/s [11,12]. Three empirical component rules for the stabilization of a supercooled metallic liquid were proposed, including 1) the multicomponent system should consist of three or more elements, 2) there should be a

significant difference (greater than 12%) in the atomic sizes of the main constituent elements, and 3) the elements should have negative heats of mixing [13]. Recently, several types of BMGs which require low R_c have been commercially available, such as Vitreloy 1 ($Zr_{41.2}Ti_{13.8}Cu_{12.5}Ni_{10.0}Be_{22.5}$ (at. %), $R_c = 1$ K/s [14]); Vitreloy 106a ($Zr_{58.5}Cu_{15.6}Ni_{12.8}Al_{10.3}Nb_{2.8}$ (at. %), Be-free, $R_c = 1.75$ K/s [15,16]); and Vitreloy 101 ($Cu_{47}Ti_{34}Zr_{11}Ni_8$ (at. %), $R_c = 250$ K/s [17, 18]).

1.3. ADDITIVE MANUFACTURING OF METALLIC GLASSES

Since the commercialization of the first machine for 3D printing or additive manufacturing (AM) in 1987, several new AM technologies have been proposed and commercialized. Nowadays, AM technologies are widely accepted by the industries, such as aerospace and medical, and their application scopes are continuously expanding [19–25]. The reported AM techniques include stereo-lithography apparatus (SLA), fused deposition modeling (FDM), laminated object manufacturing (LOM), selective laser sintering (SLS), selective laser melting (SLM), laser engineered net shaping (LENS), direct metal deposition (DMD), electron beam melting (EBM), etc. Materials being used include resin, wax, polymer, plastic, ABS, polycarbonate material, metal powder, and others.

The AM techniques for manufacturing metal parts mainly include SLS/SLM, LENS, LOM, and DMD [26–30]. SLS, LENS, and DMD are powder-based processes. In SLS, powders at a specific location are sintered or fused by a laser beam, layer by layer, according to the design of 3D models. The main advantage of SLS is that a wide range of materials can be used and the disadvantages are that the manufacturing accuracy is limited by the size of particles and the mechanical strength of as-fabricated parts is normally lower than that of the counterpart bulk material [28]. In LENS (or DMD), a part is built by melting

metal powders, which are injected into a specific location, with a high-power laser beam. This process permits the use of a large variety of metals and the combination of them, such as stainless steel, nickel alloys, tooling steel and copper alloys [27,29]. The LENS process can also be used for part repairing. An important issue in this process is the residual stresses induced by uneven heating and cooling processes. Also, the finished parts by LENS usually have a poor surface quality and need an additional milling process. LOM is a foil-based manufacturing process, which combines additive and subtractive techniques to build a part layer upon layer. In the LOM process, initially papers were used and they were bonded together by glues/binders with pressure and/or heat. The technology was later extended to metal foils and the use of ultrasonic solid-state welding to fuse foils. Then, a milling tool was used to cut or trim the foil to the desired shape. The advantages of LOM are low cost, less deformation, and the possibility of building large parts. The disadvantages are that the subtracted material cannot be reused and the fabricated parts are directionally dependent for mechanical properties, usually the vertical strength (in the direction perpendicular to foil surface) of the part is much less than the transverse strength [30].

However, there is not yet a fully density & fully amorphous BMG part been successfully manufactured by AM ever reported. Recently, Sun [31] studied the microstructure evolution of Vitreloy 106a BMGs processed by LENS technology. He pointed out that the crystallization phenomenon in the heat-affected zone (HAZ) took place even at an R_c of 10^4 K/s due to complex thermal history. Hence, preventing crystallization in the HAZ is the main challenge rather than in the melting zone. Zhang et al. [32] have found a similar phenomenon in powder-based AM process. Pauly et al. [33] studied the SLM process on iron-based BMG powders ($\text{Fe}_{74}\text{Mo}_4\text{P}_{10}\text{C}_{7.5}\text{B}_{2.5}\text{Si}_2$). Their results have

shown that a certain degree of amorphous phase exists on corners and sides of the complex geometry printed by SLM 250HL station but the 3D part itself was not fully dense. There are some studies on laser welding of BMGs [34–36], while none of these results leads to 3D BMG structures. On one hand, powders are the main reason causing the existence of micro-pores/cracks in the fabricated parts and, on the other hand, the light weight of powders makes the application of cooling media (e.g., liquid/vapor nitrogen or argon) difficult to achieve rapid cooling.

1.4. RESEARCH OBJECTIVES

The main objective of this research is to develop an additive manufacturing based technology for producing large, complex, and functional metallic glass part. At the same time, fundamental understanding on the laser-BMG interaction during AM process is studied. To achieve this purpose, four research tasks are carefully studied to achieve this overall objective.

Specifically, the research task 1 focuses on developing the additive manufacturing system. The commercialized AM technology SLM may have the ability of producing fully amorphous BMG part after intense researches have been conducted. While as a powder bed fusion (PBF) process, the following drawbacks would always exist: 1. high cost on the powder itself and its handling; 2. high tendency of oxidization due to the high surface-volume ratio; and 3. extra care need to be taken on the generation of pores. Considering the above drawbacks, we will develop a new AM technology, Laser-Foil-Printing, for this particular research. The whole system will be designed and developed from scratch, including a welding laser, a beam expander, a scanner system, a motion stage, a shielded working chamber, a cutting laser, an optical path, and a computer. The developed LFP

system will be able to build large 3D objectives layer by layer from metal foil feed stock (~50 – 200 μm thick).

Research task 2 addresses the fundamental question of how the amorphous metallic glass alloy get crystallized. The crystallization theory for cooling from molten status is well developed for the casting case. However, the heating of a casted ‘real-world’ metallic glass has shown a different crystallization behavior from what has been developed. By studying and analyzing the heating of BMG under different conditions, the crystallization behavior of such BMG will be addressed. Based on these analysis, the classical nucleation theory (CNT) will be modified in order to better describe the crystallization behavior of a ‘real-world’ metallic glass. The developed model will be important for further investigation of BMG phase evaluation during additive manufacturing.

In task 3, research will be conducted on how crystallization phase in BMG evolves during laser welding. First, the temperature evolution of metallic glass during laser welding will be studied. In a 3D domain with a focused input energy source, the temperature field will be highly time and location dependent. Experiments and numerical models will be carried out in order to understand the temperature field evolution as respect to laser parameters. Then, by combining the temperature history with the outcomes form task 2, the evolution of crystalline phase can be calculated numerically. In addition, tests will be carried out in character amorphous and/or crystallized metallic glass phases, including polishing, etching, optical microscope, XRD, DSC, SEM, TEM.

Research task 4 aims to connect fundamental study to the practical AM process. The practical AM process involves more parameters besides laser-BMG interaction such as laser track interspace and layer thickness. In this task, we will carry out study on how

the laser track interspace will affect the processing parameters. The results should offer a comprehensive understanding of how a BMG part been developed by the practical AM process.

The outcomes of above research tasks are expected to advance the knowledge of applying additive manufacturing technology in producing BMG structures. The technical develops may benefit not only the areas of additive manufacturing and materials, but also the areas that desire high properties materials such like civil engineering, aerospace engineering,

1.5. ORGANIZATION OF DISSERTATION

In this dissertation, there are four major developments been presented. Paper I focus on the development of the Laser-Foil-Printing additive manufacturing technology for producing large metallic glass structures. This study lays the foundation of the work presented in this dissertation. Paper II and III study the theory behind the crystallization behavior during laser-BMG processing from material point of view. A comprehensive numerical model is developed that simulate the crystallization process of BMGs during both heating and cooling. Paper IV presented a detailed parametric study on the AM process. This work links the typical processing parameters to the crystallization evolution during additive manufacturing.

All of the four articles share a same core research topic: additive manufacturing of metallic glass parts, while each of them has a different focus. In Paper I, we have a detailed introduction on the methodology and hardware system of Laser-Foil-Printing developed in Laser based manufacturing lab in Missouri S&T. This method is able to produce fully amorphous, fully density metallic glass with complex geometry. Also in Paper I, a

temperature model is developed to calculate the evolution of temperature field during laser-BMG interaction. The typical heating and cooling rate with the BMG is estimated. In Paper II, a comprehensive study for understanding on the crystallization behavior of BMG is conducted. Experiments are conducted to study the crystalline phase evolution, particularly in the heat-affected zone (HAZ), during laser processing of LM105 ($Zr_{52.5}Ti_5Al_{10}Ni_{14.6}Cu_{17.9}$ (at. %)) MG plates. Within the framework of classical nucleation theory, the crystallization behavior of BMG is explained. Modeling predictions on the depth of fusion zone (FZ) and thickness of HAZ for different laser processing parameters were validated by comparing with the experimental measurements. Paper III takes the research in Paper II one step further. In Paper III, the effects of both pre-existing and quenched-in nuclei over the crystallization behavior of Zr- based BMG are investigated. We find that a small amount of pre-existing nuclei in a BMG can change the time-temperature-transformation (TTT) curve from a well-known 'C shape' to a 'ε shape.' This means even for a same alloy, the tendency of crystallization can be different if the quantity of pre-existing nuclei density varies. Based on the experimental observation and theoretical discussion, two quality factors were proposed that can quantify the effect of pre-existing nucleus density on the further crystallization. In Paper IV, we link the fundamental research of laser-BMG interaction to the practical additive manufacturing process. The effect of overlap on the crystallization behavior of Zr- based metallic glass ($Zr_{52.5}Ti_5Al_{10}Ni_{14}Cu_{17.9}$, at. %) during laser based additive manufacturing is investigated.

PAPER

I. 3D PRINTING OF LARGE, COMPLEX METALLIC GLASS STRUCTURES

Yiyu Shen, Yingqi Li, Chen Chen, and Hai-Lung Tsai

Department of Mechanical and Aerospace Engineering

Missouri University of Science and Technology, Rolla, Missouri 65409, U.S.A.

ABSTRACT

Metallic glasses (MGs) or amorphous alloys although have superior mechanical properties their products are limited to simple geometries such as foils/plates or rods with thin section-thickness due to the requirement of high cooling rates. In this study, 3D, large dimensions of amorphous structures with complex geometry are manufactured by our newly developed Laser Foil Printing (LFP) technology. Zr-based (LM105, provided by Liquidmetal Technologies, Inc.) amorphous foils of 100 μm thickness are used as feedstock, and they are laser welded, layer-by-layer, to become 3D amorphous structures. Test results by X-Ray diffraction (XRD), differential scanning calorimetry (DSC), and micro-hardness confirm that the printed structures at selected process parameters achieve the same or better degree of amorphization as the raw foils. A mathematical model was developed to calculate the heating and cooling rates during structure manufacturing which helps the selection of process parameters. This study expands MG products to 3D arbitrary geometries with large dimensions due to the inherited advantages of the LFP technology which would open many potential applications.

Keywords: Bulk Metallic Glasses (BMGs), Amorphous Alloys, Additive Manufacturing, 3D printing

1. INTRODUCTION

Metallic glasses (MGs) or amorphous alloys can be produced by rapid quenching and solidification of molten metals to bypass crystallization. Atoms in amorphous metals exist in a random/disordered manner much like atoms in the liquid phase. Compared to traditional crystalline metals, MGs have superior properties such as high tensile strength, hardness, wear resistance, and corrosion resistance [1–5]. These properties are inherited from randomness/disorder of atoms in the MG which is different from crystallized metals in which periodic arrays of atoms, called crystal lattices, are arranged in an organized, structured manner. In a crystalline metal, however, mainly due to multi-directional slow cooling and solidification, defects/dislocations/segregations always exist between grains/crystals (grain boundaries or interfaces) which are the “weak spots” and could initiate “cracks” when subjected to external loading, propagating and eventually leading to the failure of the entire structure. Hence, tensile strength, for example, for a “normal” crystalline metal can only be a fraction of otherwise “perfect” crystal lattices of the same metal composition.

As heat can only be dissipated from the outer surface of a metal to its surroundings, the metal cooling rate (CR) depends on the outer surface area, the convective heat transfer coefficient between the metal outer surface and its surroundings, and the temperature of the cooling medium. Generally, the size and geometry of the metal part should have a large surface-to-volume ratio in order to rapidly dissipate heat from the metal surface to its surroundings. For thick parts, as thermal energy at the internal locations must be transferred by conduction to the outer surface, CRs inside the metal are controlled by the metal thermophysical properties (e.g., thermal conductivity). High CRs can be achieved by

improved production technologies, such as melt spinning or copper-mold casting. On the other hand, with novel and advanced alloy ingredients, the required critical cooling rate (R_c) to achieve amorphous phases can be significantly decreased which effectively increases the casting thickness from micrometers to millimeters, even centimeters [6,7]. When the thickness of amorphous alloys is greater than 1 millimeter they are commonly called “bulk” metallic glasses (BMGs). Although significant progresses have been made, amorphous parts produced today are still limited to simple geometries, such as ribbons/foils/thin plates or wires/slim rods, but not 3D large structures with complex geometry, which limits the scope of their applications [8].

In 1950, Banner et al. [9] produced Ni-P metallic glass coating by electrophoretic deposition (EPD). In 1958, Turnbull and Cohen [10] reported the supercooled phenomenon of Hg liquid at 20% of its solidification temperature. This work laid the foundation for thermodynamic theory of MG forming [11,12]. Another milestone in the MG history came in 1960 when Klement et al. produced a 20 μm -thick MG foil [13]. This was the first time the thickness of MG reached a micro-level and made MG useable for practical applications. Not a long after, electric transformer materials were gradually replaced by MG foils due to their good thermal and magnetic properties.

While earlier researchers aimed at increasing CR during BMG forming process, material scientists focused their attentions on glass forming ability (GFA), the required condition for an alloy transition from liquid phase to MG phase, which usually includes a critical cooling rate (R_c) and glass transition temperature (T_g). Since 1980s more than thousands of Zr-, Co-, Cu-, Pt-, Pd-, Ti-, Ni- or Fe-based amorphous alloys have been successfully developed, and R_c was decreased from approximately 10^6 K/s to less than 10

K/s [14,15]. Three empirical component rules for the stabilization of a supercooled metallic liquid were proposed, including 1) the multicomponent system should consist of three or more elements, 2) there should be a significant difference (greater than 12%) in the atomic sizes of the main constituent elements, and 3) the elements should have negative heats of mixing [16]. Recently, several types of MGs which require low CRs have been commercially available, such as Vitreloy 1 ($Zr_{41.2}Ti_{13.8}Cu_{12.5}Ni_{10.0}Be_{22.5}$ (at. %), $R_c = 1$ K/s [17]); Vitreloy 106a ($Zr_{58.5}Cu_{15.6}Ni_{12.8}Al_{10.3}Nb_{2.8}$ (at. %), Be-free, $R_c = 1.75$ K/s [18,19]); and Vitreloy 101 ($Cu_{47}Ti_{34}Zr_{11}Ni_8$ (at. %), $R_c = 250$ K/s [20,21]). Although the required R_c to achieve fully amorphous has been significantly reduced for the newly developed alloys, the thickness of amorphous parts does not “proportionally” increase due to the fact that, for example, the Zr-based alloys have a very low thermal conductivity (~ 7 W/m·K) as compared to that of the major elements in the alloy, e.g., zirconium (~ 23 W/m·K). “Heat” at the internal locations cannot be rapidly conducted to the surface and then dissipated to the surrounding cooling medium, which, as a result, limits the CR and consequently the thickness of the amorphous part. Generally, amorphous alloys have a lower melting temperature and lower thermal conductivity than those of the major individual elements of the alloys.

BMGs can be reheated and formed in the supercooled liquid region in which the glass relaxes into metastability and exhibits considerable softening which can be used for thermoplastic forming (TPF) [22]. In addition to the melt spinning and direct casting technologies, several processing methods based on TPF have been proposed including compression and injection molding, extrusion, rolling, blow molding, nano-forming, nano-imprinting, etc. Some of these processing technologies (e.g., blow molding) can fabricate

net-shape complex 3D parts; however, the maximum section-thickness of these parts is still limited up to a few millimeters due to very high viscosity of the supercooled metastable liquid and the CR requirement [22]. So far no manufacturing technology available to build MG structures in complex geometry with more than a few centimeters of section-thickness [23,24].

Since the commercialization of the first machine for 3D printing or additive manufacturing (AM) in 1987, several new AM technologies have been proposed and commercialized. Nowadays, AM technologies are welcomed by industry, such as aerospace and medical, and their application scopes are continuously expanding [25–31]. The reported AM techniques include stereo-lithography apparatus (SLA), fused deposition modeling (FDM), laminated object manufacturing (LOM), selective laser sintering (SLS), selective laser melting (SLM), laser engineered net shaping (LENS), direct metal deposition (DMD), electron beam melting (EBM), etc. Materials being used include resin, wax, polymer, plastic, ABS, polycarbonate material, metal powder, and others. In this paper, we focus on the additive manufacturing of metal parts.

The AM techniques for manufacturing metal parts mainly include SLS (including SLM), LENS, LOM, and DMD [32–36]. SLS, LENS, and DMD are powder-based processes. In SLS, powders at a specific location are sintered or fused by a laser beam, layer by layer, according to the design of 3D models. The main advantage of SLS is that a wide range of materials can be used and the disadvantages are that the manufacturing accuracy is limited by the size of particles and the mechanical strength of as-fabricated parts is normally lower than that of the counterpart bulk material [34]. In LENS (or DMD), a part is built by melting metal powders, which are injected into a specific location, with a

high-power laser beam. This process permits the use of a large variety of metals and the combination of them, such as stainless steel, nickel alloys, tooling steel and copper alloys [33,35]. The LENS process can also be used for part repairing. An important issue in this process is the residual stresses induced by uneven heating and cooling processes. Also, the finished parts by LENS usually have a poor surface quality and need an additional milling process. LOM is a foil-based manufacturing process, which combines additive and subtractive techniques to build a part layer upon layer. In the LOM process, initially papers were used and they were bonded together by glues/binders with pressure and/or heat. The technology was later extended to metal foils and the use of ultrasonic solid-state welding to fuse foils. Then, a milling tool was used to cut or trim the foil to the desired shape. The advantages of LOM are low cost, less deformation, and the possibility of building large parts. The disadvantages are that the subtracted material cannot be reused and the fabricated parts are directionally dependent for mechanical properties, usually the vertical strength (in the direction perpendicular to foil surface) of the part is much less than the transverse strength [36].

In laser material processing, as a large amount of energy is tightly focused onto a very small area, the heating rate (HR) and CR of the processed part are very high ($10^4 \sim 10^5$ K/s) [37]. This makes laser-based AM technologies naturally a promising method in building large MG parts [38]. Recently, Sun [24] studied the microstructure evolution of Vitreloy 106a MGs processed by LENS technology. He pointed out that the crystallization phenomenon in the heat-affected zone (HAZ) took place even at a CR of 10^4 K/s due to complex thermal history. Hence, preventing crystallization in the HAZ is the main challenge rather than in the melting zone. Zhang et al. [39] have found a similar

phenomenon in powder-based AM process. Pauly et al. [40] studied the SLM process on iron-based MG powders ($\text{Fe}_{74}\text{Mo}_4\text{P}_{10}\text{C}_{7.5}\text{B}_{2.5}\text{Si}_2$). Their results have shown that a certain degree of amorphous phase exists on corners and sides of the complex geometry printed by SLM 250HL station but the 3D part itself was not fully dense. There are some studies on laser welding of MGs [41–43], while none of these results leads to 3D MG structures. On one hand, powders are the main reason causing the existence of micro-pores/cracks in the fabricated parts and, on the other hand, the light weight of powders makes the application of cooling media (e.g., liquid/vapor nitrogen or argon) difficult to achieve rapid cooling.

In this study, we use the newly developed laser foil printing (LFP) technology to weld amorphous foils, layer-by-layer, via laser to construct 3D MG parts of complex geometry. Different methods were used to examine the crystallization or the degree of amorphization for printed parts. A mathematical model was also developed to calculate the temperature distribution in the part during the processing in order to understand and explain the phenomena observed in the experiment.

2. THE LASER FOIL PRINTING (LFP) TECHNOLOGY

Details of the LFP technology can be found in Ref. [44]. However, in order to understand how a part is manufactured, which will affect the formation of crystalline, and also to discuss the effect of process parameters, the method, system and procedure for the LFP technology are briefly described below.

A schematic of the LFP process is given in Fig. 1. Like most of other AM technologies, the procedure starts with a 3D CAD model (STL file) of the desired part. Then, the model is transferred to a set of layer data by a slicing software. Finally, the set of layer data is translated by the control program into machine instructions and executed layer by layer. The manufacturing process is mainly realized by two alternative processes: foil-welding by a continuous wave (CW) fiber laser and foil-cutting by a pulsed UV laser. When a fresh foil is fixed by spot-welding on the substrate, the program controls the scanner to scan a specified pattern path of the CW laser beam on the foil to weld the foil to the substrate. Depending upon the desired R_c for different amorphous alloys, welding can be accomplished via line-welding or spot-welding. The welding path/pattern should be designed (which depends on the geometry of the part) to achieve symmetrical welding in order to minimize possible thermal stress/part distortion, and at the maximum separations in time and in space between two consecutive weldings to avoid heat accumulation and achieve high CRs. For example, for a spot-welding at location A, the next spot-welding at location B should be as far as possible from A. After the welding process is done, an X-Y motion stage shifts the part to the location under the UV laser beam. Then, the program controls the X-Y motion stage and the UV laser to cut the welded foil along the outer and/or inner circumferences of the part. After the laser cutting is completed, the redundant foil is

removed and another fresh foil is placed and fixed on the top of the sample. The aforementioned entire process can be fully automatic. This procedure is repeated until the whole desired 3D part is built. Note, in the two alternative processes, laser welding can be done ahead of laser cutting or vice versa.

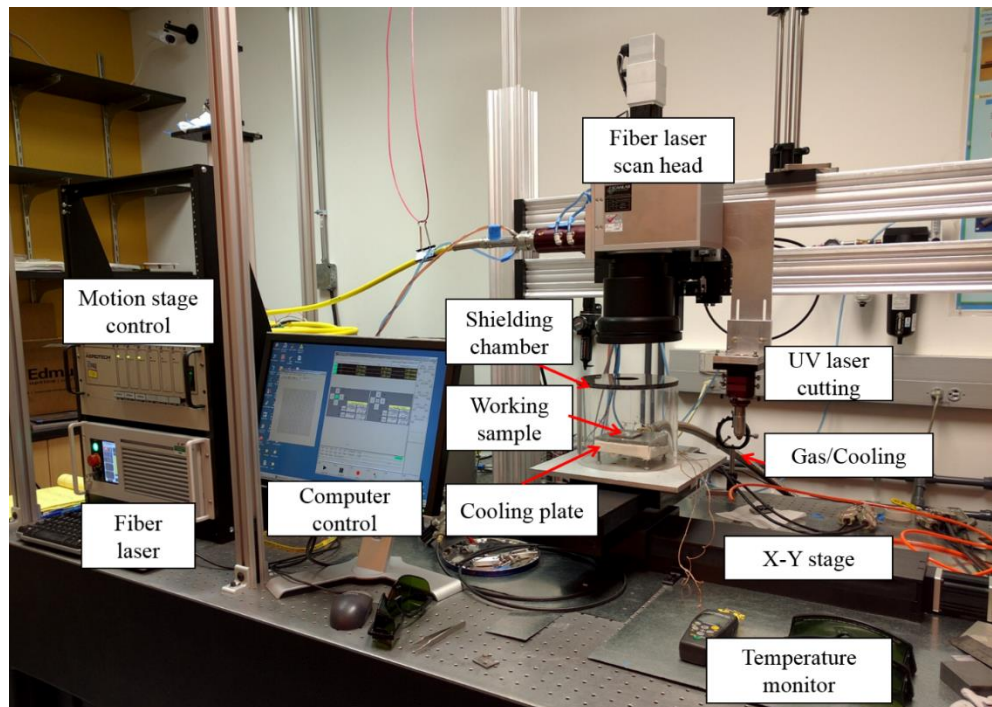
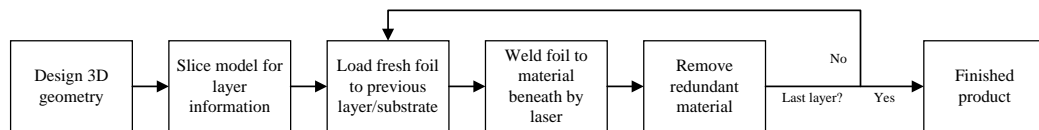


Figure 1. Schematic of the LFP process and the LFP system setups at the Laser-Based Manufacturing Lab, Missouri S&T.

Figure 1 also shows the LFP setup developed at the Laser-Based Manufacturing Lab, Missouri S&T. The welding laser is an IPG YLR-1000 CW (continuous wave) fiber laser with a wavelength of 1070 nm and a maximum output power of 1000 W. The cutting laser is a Coherent AVIA-355X laser with 355 nm UV wavelength, Q-switched, 30 ns pulse duration and 10 W maximum power. Note, the UV laser, not shown in the figure, is located in another room. The welding laser beam passes through an optical fiber, enters a collimator to become an expanded parallel beam, then enters the scanner (hurrySCAN25, SCANLAB), and finally is focused on the foil through an F-theta lens with an effective focal length of 33 cm. The cutting UV laser beam passes through several turning mirrors and is focused by a focusing lens with a 10-cm focal length. A cooling chamber with a heat exchanger plate at the bottom by passing through liquid nitrogen or liquid argon is designed to achieve rapid cooling while the amorphous structure is being manufactured. Liquid nitrogen has the boiling temperature of $-195.79\text{ }^{\circ}\text{C}$, while liquid argon is $-185.87\text{ }^{\circ}\text{C}$. As some of the amorphous alloys (e.g., Zr-based or Ti-based) may be sensitive to nitrogen, liquid nitrogen (much cheaper than liquid argon) is used for the cooling plate while liquid argon is used in the cooling chamber. The cooling chamber, filled up with argon vapors, provides the needs of both cooling and shielding simultaneously. A coaxial compressed assisting/shielding/cooling argon gas is used for the UV laser to achieve clean cuts. The collimator and scanner for the fiber laser, and the focusing lens for the UV laser are mounted on a Z (vertical) motion stage. The foil is first positioned and fixed onto the substrate via spot-welding using a mold plate with predetermined hole-pattern, and the entire structure is placed on an X-Y (horizontal) motion stage (Aerotech). The two lasers, scanner and three-axis motion stage are integrated through control programs to a computer.

The use of two lasers in this study, one for welding and the other for cutting, is to achieve simultaneously high processing speeds and good part quality. For welding, the CW fiber laser coupled with a scanner provides high speeds and flexibility for selecting desired welding paths. However, any laser, pulsed or CW, with any wavelength can be used for welding, and the scanner can be replaced by a stationary focused beam. For cutting, the UV, Q-switched laser with stationary focusing lens and coaxial assisting gas will provide high peak power for clean cuts. However, a scanner with any type of laser or even a CNC machine, can be used for the cutting purpose. In fact, for the entire welding and cutting processes, a laser with a 3-axis motion stage can be used to achieve the objective, although the manufacturing speed and quality of the part would have to be sacrificed.

This technology is able to produce metal parts directly from 3D models with laser welding and cutting of metal foils [44]. The LFP technology shows its unique advantages on processing 3D parts of amorphous over other methods. First, it is easy to achieve a full-density 3D part by the LFP technology. This is not hard to understand because raw foils have no pores inside, while powders have gaps/voids in between. Second, CRs in the LFP technology should be higher than those in powder-based methods at the same laser process condition because the thermal contacts between powders are poor. Third, liquid/vapor nitrogen or argon can be used as cooling and/or shielding media in the LFP technology which, however, may blow powders away in powder-based AM technologies such as SLM and LENS. The liquid/vapor nitrogen or argon will increase the CR and decrease the working temperature to below the crystallization temperature of the foils. Thus, crystallization is less likely to occur in LFP technology than in powder-based technology at the same/similar laser processing condition.

3. EXPERIMENT AND TESTING

In this study, 100 μm -thick LM105 ($\text{Zr}_{52.5}\text{Ti}_5\text{Al}_{10}\text{Ni}_{14.6}\text{Cu}_{17.9}$ (at. %)) amorphous foils were selected for welding onto 0.75 mm-thick LM105 amorphous plates, both are provided by Liquidmetal Technologies, Inc. Sample parts obtained from experiments were sectioned, mounted, ground and polished (LECO spectrum system 2000) at 150, 400, 800 and 1200 grits and etched by a solution of 100 ml H_2O , 2 ml H_2O_2 and 0.1 ml HF for 10 seconds. The prepared samples were examined by an optical microscope (OM), differential scanning calorimetry (DSC, TA Instruments DSC 2010), X-ray diffraction (XRD, Philips X-Pert) and micro-hardness (Struers Inc., Duramin 5) to analyze the amorphous phase.

3.1. LASER WELDING OF AMORPHOUS FOILS

The quality of laser welding is the key step for the quality and success for a large size of MG structure by the LFP process. Hence, we need to first understand the characteristics of laser welding of foils and the effect of process parameters on weld quality. Laser power is a major parameter determining the thermal history and, hence, the crystallization behavior of the part to be fabricated. Once the HR or CR in the weld fusion zone (WFZ) or heat-affected zone (HAZ) drop below some critical values (which are material dependent), nano- or micro-size crystals start to grow, leading to the decrease of amorphous phase percentage in the part [45–49]. Also, “bad” welding parameters may cause poor bonding strength, micro pores, geometry deformation or other defects and, as a result, the final mechanical properties of the part.

Figure 2 shows two typical weld surface profiles for laser welding of foils on substrates. For Fig. 2(a) the laser was in a continuous wave (CW) mode, the laser power

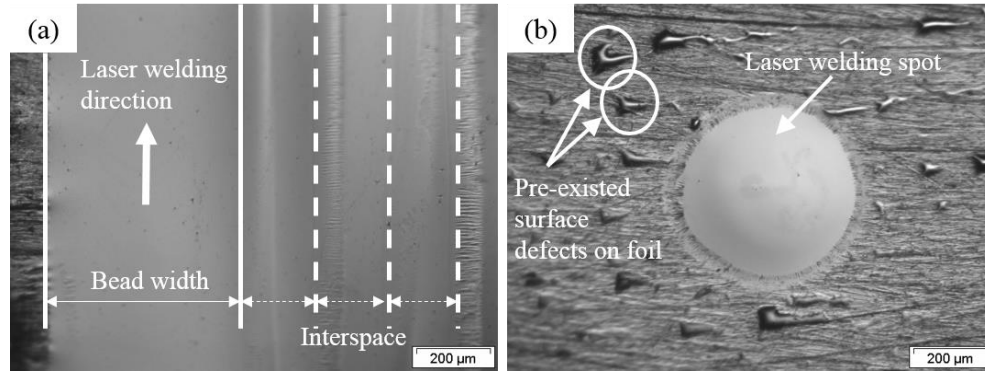


Figure 2. Top surface profile of laser welding of foils on plates: (a) continuous wave (CW) laser line-welding and (b) pulsed laser spot-welding.

(P) was 200 W, the laser scan speed (v) was 150 mm/s and the beam diameter (D) at the welding plane was about 430 μm . It is seen in Fig. 2(a) that a smooth weld surface profile was achieved with a width of around 450 μm and the interspace between two welding tracks was 200 μm (i.e., ~55 % overlap). For Fig. 2(b) the laser was in a pulsed mode, $P = 200$ W, pulse duration (Δt) was 4 ms, and $D = 430$ μm . No welding defect was found at the top surface. It is worth noting that in Fig. 2(b) the original surface of the foil contains pre-existing defects which may be caused by its manufacturing process. Laser surface re-melting could be an effective way to enhance the surface quality and repair/eliminate existing surface crystallization/defects.

Figure 3(a) shows cross-section profiles for the line-welding of a foil on a substrate. In order to understand the importance and the effect of process parameters on crystallization, Fig. 3(a) shows an example of a “bad” weld which is a line-weld and the cross-section is perpendicular to the welding direction. The parameters are $P = 400$ W, $v = 100$ mm/s, $D = 430$ μm and the interspace between two scans was 200 μm . The micro crystalline phases away from the top surface are clearly visible after etching.

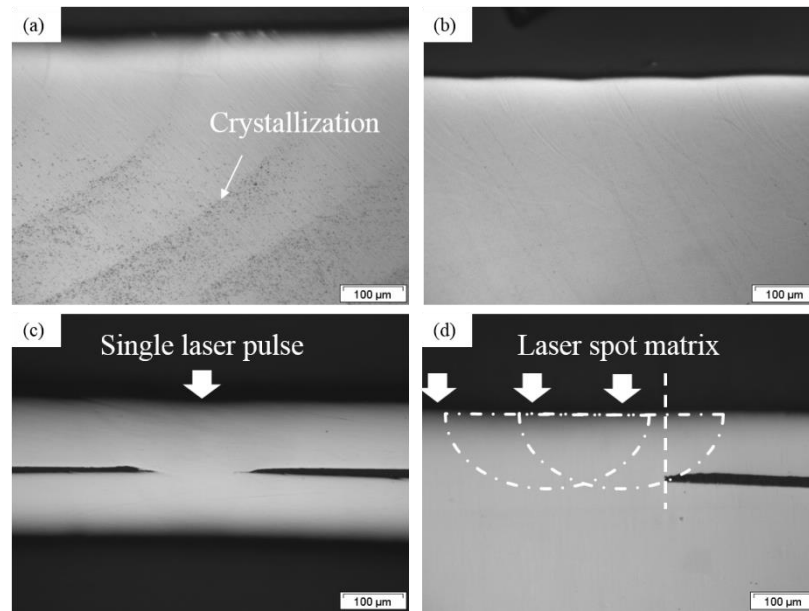


Figure 3. Cross-sections of laser weld beads: (a) cross-section perpendicular to the welding direction for a CW laser welding with crystallization, (b) cross-section perpendicular to the welding direction for a CW laser welding without crystallization, (c) cross-section of single spot laser welding between two foils, and (d) cross-section for laser spot (matrix) welding.

As compared to the process parameters for Fig. 2(a) ($P = 200$ W and $v = 150$ mm/s; energy deposition rate is 1.33 J/mm), the energy deposition rate for Fig. 3(a) is 4 J/mm = 400 W / 100 mm/s. Apparently, the energy deposition rate is higher here which is believed to be the cause of crystallization. Figure 3(b) is the cross-section perpendicular to the welding direction for the process parameters given in Fig. 2(a) and no crystalline phase was observed. A good join between the foil and the substrate was obtained without cracks or pores. Generally, for laser welding of thin foils, v must be high enough to maintain a high HR/CR; however, P should be high enough to be able to weld the foil to the substrate below. In other words, laser energy input should be minimized to avoid crystallization and also possible foil distortion.

Laser spot-welding is another possible method to avoid crystallization during welding. Figure 3(c) shows the cross-section of a single spot-welding of two foils. The parameters are $P = 200$ W, $\Delta t = 4$ ms and $D = 430$ μm . Figure 3(d) is the cross-section image of a series of laser spot-welding (matrix, also see Fig. 5(a)) of a foil on the substrate with the same processing parameters as in Fig. 3(c). The interspace between the centers of two welding spots was 140 μm and the overlap was about 67%. It is almost impossible to see the overlaps between two welding spots and the deformation of the top foil is not noticeable. For thin foil welding, extra care must be taken on the control of total laser energy input; over input of laser energy may cause foil deformation or material vaporization/ejection.

3.2. SAMPLE AND TEST RESULTS

Based on the provided literature, the critical temperatures for LM105 are: glass transition temperature $T_g = 399$ °C, crystallization temperature $T_x = 468$ °C, solidus temperature $T_s = 785$ °C, and melting temperature $T_m = 858$ °C. As shown above, the use of either line-welding or spot-welding can achieve fully amorphous, in this study we chose spot-welding to print parts because it can achieve higher CRs. In order to confirm if crystallization takes place during the LFP process, a 10-mm (100 layers of foils) cubic test sample was fabricated by spot-welding and the overlap between two laser spots was about 67%, as shown in Fig. 4. The 100-layer sample was fabricated under the same conditions as Fig. 3(d): laser pulsed mode with $\Delta t = 4$ ms, $P = 200$ W and $D = 430$ μm in the argon shielded chamber at room temperature. The inset in Fig. 5 illustrates the sequence of the spot-welding for each layer. The laser pulse repetition rate was set to 1 Hz to minimize heat accumulation at the same location. All foils and substrates were slightly polished to a

400-grit finish right before welding in order to remove possible oxidization. All welding processes were conducted under argon shielding environment. However, we found that liquid argon cooling was not necessary in this study due to the high glass forming ability (GFA) and the required slow CR of LM105.

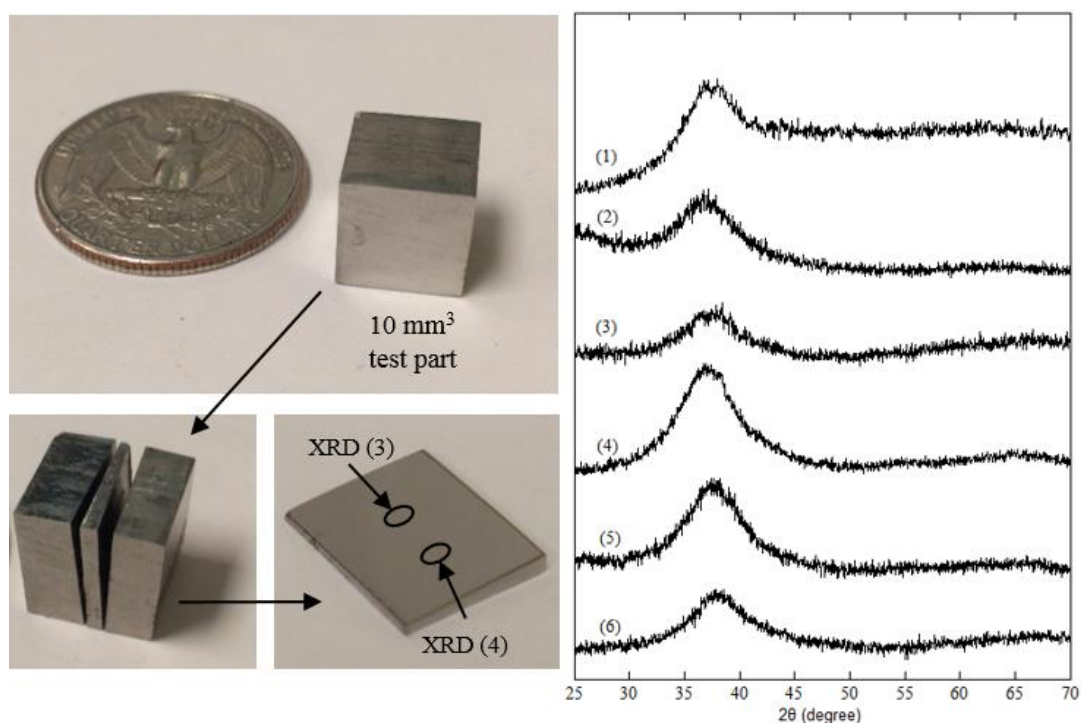


Figure 4. XRD test of printed sample. Left: photo of the 3D test sample; right: XRD patterns of the 3D printed part; Curve (1) top surface; Curve (2) 0.5 mm below the top surface; Curve (3) & Curve (4) cross-section as shown in the figure, and Curve (5) as received 0.75 mm plate top surface, and Curve (6) as received 100 μm foil top surface.

Figure 4 also shows the XRD results at different locations of the test sample. Curves (1) through (4) are, respectively, the XRD patterns for the test sample's top surface (1), the parallel plane 0.5 mm below the top surface and along the centerline (2), and the cross-

section (3) and (4) along the centerline and at 1/3 and 2/3, respectively, from the top surface. For comparison, Curve (5) is the XRD pattern of the original substrate and Curve (6) is the XRD pattern of the foil. All of the XRD curves contain only broad halo diffraction peaks, which indicates that the amount of crystalline phase, if any, is within the detection limit (~2%) of XRD [50].

Figure 5 illustrates the top and cross-section views of the 10 mm sample as shown in Fig. 4. As can be seen in Fig. 5(a), the overlap of two laser spots is about 67%. The inset of Fig. 5(a) shows the welding “jumping” sequence which was designed to prevent heat accumulation at any location (i.e., increase the CR). From Fig. 5(b), no cracks or pores are found. The density of the tested part was measured using the Archimedes’ method which is 6.607 g/cm³. This value is close to the original foil density of 6.57 g/cm³ provided by Liquidmetal Technologies, Inc and 6.599 g/cm³ tested by us.

Figure 6 shows the comparison of DSC test results between the as-received plate and the LFP fabricated test part at a heating rate of 20 °C/min from room temperature to 600 °C. The sample part (Curve 2) shows $T_g \approx 400$ °C and $T_{x1} \approx 469$ °C and $T_{x2} \approx 479$ °C. They are close to what were reported from Liquidmetal Technologies, Inc: $T_g = 399$ °C and $T_x = 468$ °C, respectively. The original plate was tested under the same condition, and T_g was measured as 400 °C and two sharp crystallization peaks are detected at $T_{x1} = 472$ °C and $T_{x2} = 478$ °C, respectively. It is noted that the shapes of the two DCS curves for temperatures greater than 470 °C are slightly different which can be caused either by the formation of crystals or by the change of atom arrangement (initial free volume) in the MG system [51–53].

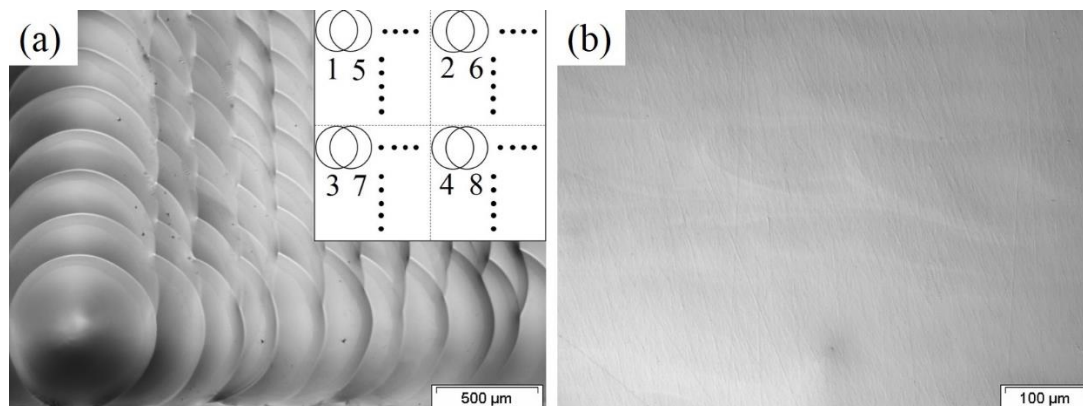


Figure 5. Optical microscope photos of the 10 mm thick test sample: (a) top surface and (b) cross- section as shown in Fig. 4.

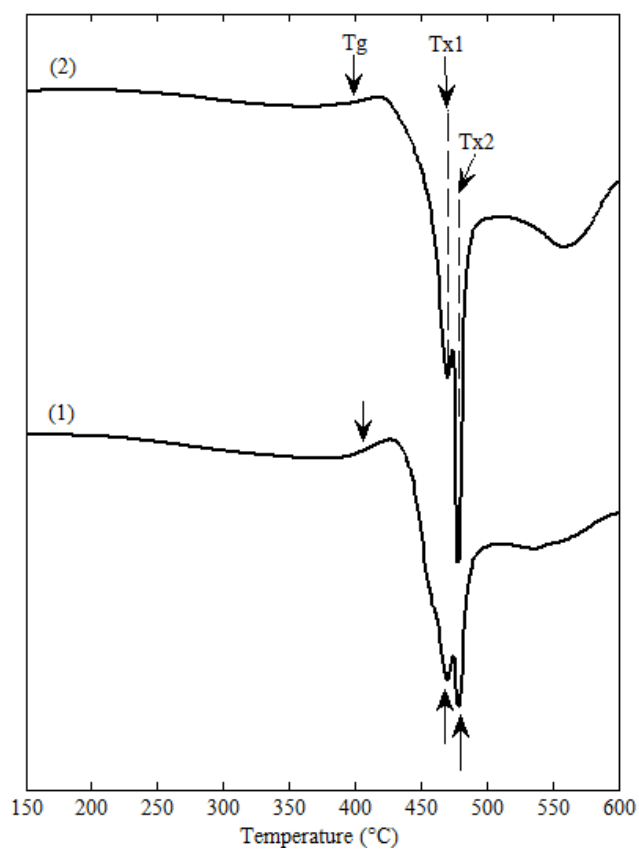


Figure 6. DSC curves (heating rate = 20 °C/min) for the tested MG samples: (1) as-received LM105 plate and (2) 10-mm cubic test sample.

As the XRD results in Fig. 4 have confirmed that there is no or little crystals in the printed 3D part, the change of initial free volume in LM105 may be the main reason that leads to the variation of the DSC curve. However, there are always possibilities that other unknown mechanisms taking place. For example, element vaporization during laser welding may occur and this can slightly shift the percentage of an element in the MG alloys. Since MG systems are very sensitive to their components and percentages, the crystallization behavior might be changed (as that in DSC curve) in a laser welding process [51]. As shown in Fig. 6 for temperatures above 500 °C, an extra peak is observed at around 560 °C for both the original plate and the sample part. This implies there may exist further crystallization behavior. Nevertheless, as in this study we are interested in finding the existence of amorphous phase, the consistency/similarity between Curve 1 and Curve 2 in Fig. 6 for temperatures below 470 °C has confirmed that the LFP fabricated 3D part has the same amorphous phase as the original plate.

Micro-hardness tests were conducted for both the original plate and the cross-section of the test part. The load applied was 0.1 kgf and the indenting time was 10 seconds. The micro-hardness of the original plate was 588.56 ± 25.5 Hv which is very close to 570 ± 30.6 Hv for the test part. Hence, the micro-hardness data has also confirmed that the LFP fabricated 3D test part remains at its amorphous nature.

To conclude from all the aforementioned test results, it is evidence that amorphous 3D parts can be fabricated by the LFP method, layer by layer, from 100 μm foils at selected processing parameters.

It would be worth comparing the test results from this study by LFP with the results studied previously by LENS and SLM [23,24,40]. In LENS, the focused laser beam first

generates a melting pool on the substrate. Simultaneously, powders are blown towards the pool and they are melted, fused and become a portion of the part to be fabricated. Thus, laser scan speed, v , needs to be slow enough that would maintain a certain powder deposition rate. However, a lower v means more laser energy is deposited onto the substrate and a lower CR. This can be the major limitation of the LENS technology in MG structure manufacturing. For example, the highest v in Sun's study is ~ 21 mm/s (50 inch/min) and $P = 150$ W (energy deposition rate = 7.1 J/mm) [24]. This set of parameters is even higher than the case presented in Fig. 3(a), at which $P = 400$ W and $v = 100$ mm/s (energy deposition rate = 4 J/mm). A large amount of crystal phases were observed in Fig. 3(a). In an AM process, the current layer will become the next layer's substrate and, hence, if a part is manufactured by the conditions used in Fig. 3(a) the entire final part will be crystalline-rich except the very top layer which is also the final layer.

In SLM, metal powders are first evenly spread on the substrate, which is similar to the foil in LFP. Then, a laser is employed to melt the powders onto the substrate selectively. One of the major challenges in SLM is to avoid the formation of pores in the part [23,40]. The pores originated from the inter-powder gaps and because the existence of gaps, the mean thermal conductivity of powder bed is less than 2% of the bulk metal [54]. Hence, in order to avoid the formation of pores, more laser energy is required to melt the powder bed which leads to a low CR. In addition, the powders surrounding the melted part actually provide good insulation for the part being built, which also contributes to the low CR of the part.

4. THERMAL ANALYSIS

4.1. MATHEMATICAL MODELING

In order to better understand how temperature field evolves in the part during laser welding, a mathematical model was developed. As laser energy used in this study is low ($P \sim 200$ W) and the scan speed is high ($v > 100$ mm/s), the melting layer thickness is very thin (~ 150 μm), we can assume it is a heat conduction mode (instead of keyhole mode) welding. In other words, possible fluid flows in the metal and their effects on heat transfer are ignored. Also, because of rapid heating and solidification, the latent heat absorption and release due to phase changes are assumed to be negligible.

For heat conduction, the governing differential equation can be written as:

$$\frac{\partial}{\partial x} \left(k \frac{\partial T}{\partial x} \right) + \frac{\partial}{\partial y} \left(k \frac{\partial T}{\partial y} \right) + \frac{\partial}{\partial z} \left(k \frac{\partial T}{\partial z} \right) = \rho C_p \frac{\partial T}{\partial t} \quad (1)$$

where T denotes the temperature, t is the time, k is the thermal conductivity, ρ is the material density and C_p is the specific heat. The temperature dependent material properties including thermal conductivity, specific heat and density of LM105 are obtained from Refs. [55–57].

The heat losses from the part's surfaces to the surroundings are assumed to be thermal radiation and heat convection, and they are:

$$-k \frac{\partial T}{\partial n} = \epsilon \sigma (T^4 - T_\infty^4) + h(T - T_\infty) \quad (2)$$

where n is the normal direction to the surface which can be the x -, y - or z -direction, ϵ is the surface emissivity, σ is the Stefan-Boltzmann constant and h is the convective heat transfer coefficient.

The laser power is assumed to be a Gaussian distribution at the top surface (z -plane) which is expressed as:

$$I = \alpha * \frac{2*P}{\pi r^2} * e^{\frac{-2[(x-vt)^2+y^2]}{r^2}} \quad (3)$$

where I represents the laser power density, α is the surface absorptivity, P is the laser power, r is the laser beam radius and v is the laser scan speed.

The initial condition is $T = T_{\infty}$ where T_{∞} is also the ambient temperature which is set at 300 K. The convective heat transfer coefficient is assume to be 50 W/ m²·K. The differential equation with all boundary conditions and initial condition was solved by the commercial software COMSOL Multiphysics 5.1. In this model, in addition to the aforementioned assumptions, there are two major sources which may contribute to inaccuracy of the modeling predictions and they are: 1) the assumption of a Gaussian distribution of the laser beam and 2) the amount of laser energy absorption by the surface (i.e., absorptivity, α in Eq. (3)). A laser beam profiler (OPHIR Inc.) was used to measure the beam power distribution and it was found that the assumption of a Gaussian profile is reasonable. In addition, as the beam size in the present study is about 430 μ m, which is very small as compared to the sample, the effect of beam energy profile is not very critical for the overall temperature profile. The laser absorption coefficient, in general, can be a function of the surface condition and temperature, but in this study it is assumed to be a constant. In order to find a proper laser energy absorption coefficient, numerical experiments were conducted to determine a suitable value of α which is described below.

4.2. COMPARISON AND ANALYSIS

The mathematical model is “validated” by comparing the calculated results with the experimental measurements. In the experiment, a $D = 430 \mu$ m laser beam scanned over the top surface along the centerline of a 0.75 mm thick, 10 mm by 10 mm LM105 plate. The $P = 100$ W and $v = 50$ mm/s. A K-type thermocouples was fixed by a thermal joint

compound (Type 120, Wakefield Thermal Solution) at the bottom of the plate center directly beneath the laser scan path. Experiments were conducted for nine times and very consistent temperature measurements were obtained. In the model, the same processing parameters were used. The calculated domain was: x (-5 mm, 5 mm), y (-5 mm, 5 mm), and z (0 mm, -0.75 mm). The laser scanned from (-5 mm, 0, 0) toward the positive x direction. The value of α was varied. The temperature history for both experimental measurements and modeling calculations are presented in Fig. 7. There are three curves corresponding to three different absorption coefficients. The results for $\alpha = 0.136$ appear to be closer to the measurements and is a reasonable choice in our study. The average HR and CR at the location measured by thermocouples are 1163 and 225 K/s, respectively and the calculated are, respectively, 1225 and 236 K/s. Here, the average HR is calculated by the difference of the highest temperature and room temperature and then divided by the time lapsed (0.32 s to 0.38 s), and the CR is calculated from 0.38 s to 0.6 s. The differences between the modeling predictions and the experimental measurements are about 5% which from engineering point of view is acceptable. In an AM process, HR and CR are a function of time and space which are difficult to measure directly. It should be pointed out that our objective here is not to rigorously validate the model, but to obtain some reasonably accurate values of HRs and CRs during part fabrication so that we can explain possible crystallization and how that related to the selected laser processing parameters.

4.3. COOLING AND HEATING RATES

The temperature histories for bead-on-plate in laser line-welding or spot-welding are presented in Fig. 8. Three different cases, corresponding to the same process parameters used for Fig. 3(a), 3(b) and 3(c), were computed. In Case 1, shown as solid-lines in Fig. 8,

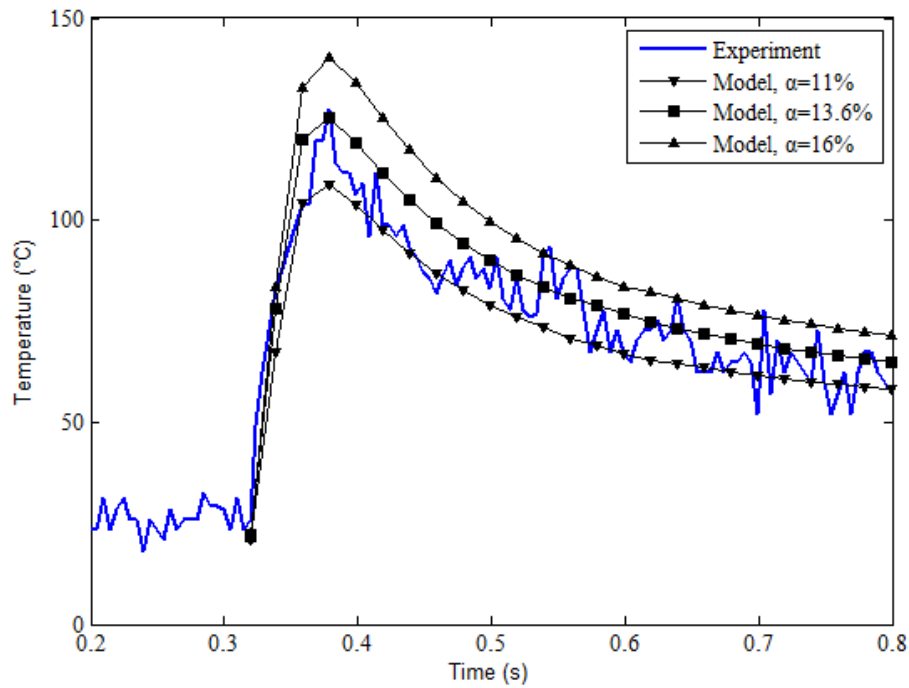


Figure 7. Comparison of temperature history processed at laser power of 100 W and scan speed of 50 mm/s by experimental measurements and modeling.

$v = 100$ mm/s and $P = 400$ W (the same parameters as in Fig. 3(a)). The three solid curves, from top to bottom represent, respectively, the temperature history in the middle of fusion zone, in the middle of HAZ (above T_g), and in the un-affected zone, as indicated in the inset, where the photo is a cross-section image perpendicular to the welding direction. The crystalline phase in HAZ can be clearly seen after chemical etching. In fusion zone, it takes about 20 ms for the molten alloy to be cooled from T_m to T_g and the CR can be estimated as 3×10^4 K/s. This is much higher than the R_c of LM105 (10 K/s). In HAZ, potential crystallization starts when the temperature exceeds T_x and ends when the temperature dropping below T_g , which is called annealing time. Thus, for HAZ the annealing time is about 18 ms, and the HR is calculated as 2.7×10^4 K/s. Note, the HR was computed as

follows: the temperature rise from T_g to the maximum temperature divided by the time lapsed. Similarly, the CR was computed by the temperature drop from the highest temperature to T_g , and then divided by the time lapsed.

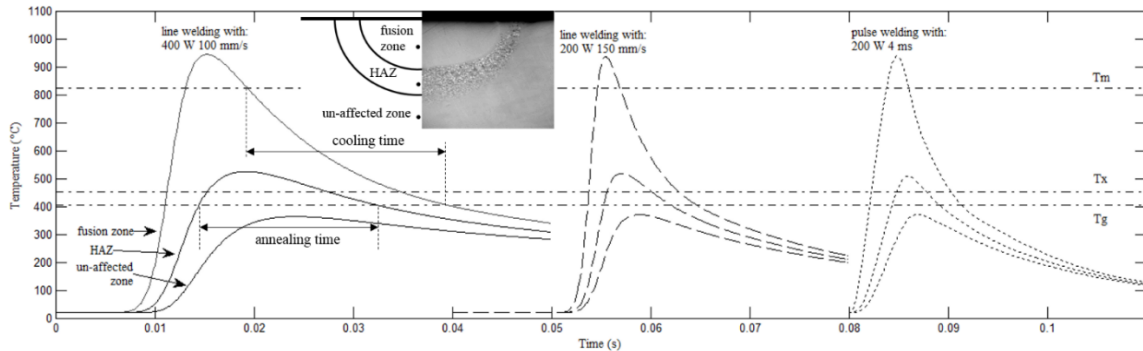


Figure 8. Plots of calculated temperature histories in the fusion zone, HAZ and un-affected zone for three cases: (a) laser line-welding shown in Fig. 3(a); (b) laser line-welding shown in Fig. 3(b); (c) laser spot-welding shown in Fig. 3(c).

Table 1. Calculated heating/cooling rates at different locations.

Case	Processing parameters	Cooling rate in fusion zone (K/s)	Cooling rate in HAZ (K/s)	Heating rate in HAZ (K/s)
1	400 W, 100 mm/s	3×10^4	9×10^3	2.7×10^4
2	200 W, 150 mm/s	5.4×10^4	2.3×10^4	6.4×10^4
3	200 W, 4 ms	1.4×10^5	3.2×10^4	1×10^5

In Case 2, shown as dashed-lines in Fig. 8, $P = 200$ W and $v = 150$ mm/s (also the same parameters as Fig. 3(b)). As can be seen, both the HR and CR in Case 2 are much higher as compared to those in Case 1. The CR in the fusion zone is calculated to be $5.4 \times$

10^4 K/s. This is much higher than R_c of LM105. In HAZ, the annealing time is 6.8 ms and the HR is calculated as 6.4×10^4 K/s.

In Case 3, shown as dotted-lines in Fig. 8, laser spot-welding at $P = 200$ W and $\Delta t = 4$ ms (also the same parameters as Fig. 3(c) and Fig. 4). The CR in fusion zone is calculated as 1.4×10^5 K/s. The annealing time is 5 ms for HAZ and the HR is calculated as 1×10^5 K/s.

The model predicts the HRs and CRs at different regions during different LFP processes; they are summarized in Table 1. It is noted that all these values are far higher than the reported critical HR and CR which are approximately 1×10^3 K/s and 10 K/s, respectively [7,19,21,24]. Based on these reported critical HR and CR, no crystallization should have occurred in all these welding cases. However, from the experiment, crystallized phases were clearly observed at Case 1, conditions in Fig. 3(a). In fact, crystallization phenomena under sufficient HRs/CRs have also been observed in previous studies [41,42,46]. Hence, the use of a HR and/or CR as criteria may not be accurate for predicting the formation of crystalline, at least in the case of laser welding.

There are two main reasons; first, the isothermal time-temperature-transformation (TTT) curves, from which the critical HR/CR were obtained, are detected under the steady-states condition. The shape of the TTT curve can be shifted, or even deformed, at different temperature gradients ($\partial T/\partial t$). For example: the T_x shifts from 740 K to 880 K at a HR from 0.2 K/s to 5 K/s under DSC test for the Vitreloy 1 alloys [24]. Another example is that Zhang et al. [58] have reported the observation of pressure dependent crystallization behavior of Zr-based MGs. In laser welding, very high temperature gradients and high

instantaneous pressure pulses (shock waves) could be generated and, as a result, the actual material behavior under laser processing still remains unknown.

Second, element vaporization during laser processing can further affect the crystallization behavior of MGs. For example, in LM105, a low-vaporization temperature element such as Al will have a stronger tendency to be vaporized as compared to the high-vaporization temperature element, Ti, while heated by a laser. It leads to an imbalance of element percentage after laser welding. Because MGs are very sensitive to relative element weights, elements losses during laser welding can be significantly affecting their crystallization behavior. It appears new criteria for the crystallization behavior of MGs in laser welding may be needed.

5. AS-FABRICATED PARTS

A fully amorphous 10-mm cubic sample was successfully built by spot-welding as shown in Fig. 4, and the same parameters were used to construct several large 3D MG parts as shown in Fig. 9. The laser pulse repetition rate was set at 1 Hz in order to avoid heat accumulation in the part. For the material removal process, a UV laser with pulse duration of 30 ns, pulse energy of 100 mJ and repetition rate of 5 kHz were used in order to achieve smooth and clean cutting edges. Though the cutting process determines the quality on the sides of the final part, as shown in Fig. 9, generally it has little effect on the amorphous percentage in the as-fabricated part. Thus the detail of laser cutting is not discussed in this paper.

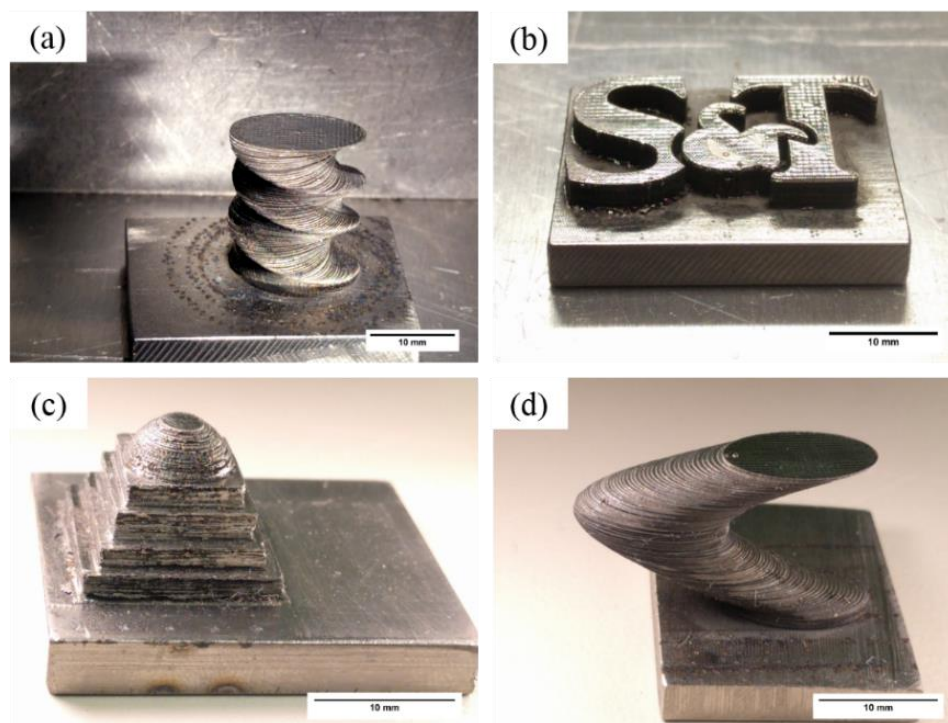


Figure 9. As-fabricated amorphous 3D parts by LFP.

The sample shown in Fig. 9(a) is a side-view of a “metal fusilli pasta” part created by a continuous rotation of an ellipse pattern. Figure 9(b) shows a 3-mm thick amorphous “S&T” logo of the Missouri University of Science and Technology. A 5-stage 3D table, includes 4-square stages and a semi-spherical cover on the top is shown in Fig. 9(c). The overall height of the part was measured to be 11.3 mm. Figure 9(d) is a slipped cylinder with overall displacement of 13 mm.

The above examples have proved that the proposed LFP process is able to build large size of complex 3D amorphous structures. However, defects such as cracks, pores, crystallization or discontinuity, may occur if processing parameters are not well selected. In dealing with multi-layer large 3D parts, weld surface flatness, gas shielding/cooling and heat accumulation also need to be considered. The system of LFP technology can be easily scaled-up for amorphous structures up to meters in dimensions.

6. CONCLUSIONS

A system, method and procedure for constructing 3D amorphous structures with complex geometry have been successfully developed. The new technology involves the integration of LFP technology with a cooling/shielding system. Several amorphous samples are fabricated and the amount of amorphous content was evaluated to validate that fully amorphous phase is achieved. The welding quality including weld pool profiles and mechanical properties were also examined. A mathematical model was developed to predict the HRs and CRs during the part manufacturing which subsequently help us understand and determine if amorphous or crystalline phases would be formed. The model will also help us select laser processing parameters to achieve an amorphous phase. The developed new technology would expand the scope of applications for amorphous alloys.

ACKNOWLEDGEMENTS

This work was supported by the Department of Energy (Grant No. DE-FE0012272) and the UM Fast Track Funding Program. The authors acknowledge the valuable comments on this paper made by Dr. Stephanie O’Keeffe at Liquidmetal Technologies, Inc.

REFERENCES

- [1] W.L. Johnson, Bulk metallic glasses – a new engineering material, *Current Opinion in Solid State and Materials Science* 1 (3) (1996) 383-386. DOI [http://dx.doi.org/10.1016/S1359-0286\(96\)80029-5](http://dx.doi.org/10.1016/S1359-0286(96)80029-5).
- [2] E.S. Park, D.H. Kim, Design of bulk metallic glasses with high glass forming ability and enhancement of plasticity in metallic glass matrix composites: A review, *Metals and Materials International* 11 (1) (2005) 19-27. DOI <http://dx.doi.org/10.1007/BF03027480>.
- [3] W.L. Johnson, Bulk amorphous metal – An emerging engineering material, *The Journal of The Minerals, Metals & Materials Society* 54 (3) (2002) 40-43. DOI <http://dx.doi.org/10.1007/BF02822619>.
- [4] J.F. Löffler, Bulk metallic glasses, *Intermetallics* 11 (6) (2003) 529-540. DOI [http://dx.doi.org/10.1016/S0966-9795\(03\)00046-3](http://dx.doi.org/10.1016/S0966-9795(03)00046-3).
- [5] M. Telford, The case for bulk metallic glass, *Materials Today* 7 (3) (2004) 36-43. DOI [http://dx.doi.org/10.1016/S1369-7021\(04\)00124-5](http://dx.doi.org/10.1016/S1369-7021(04)00124-5).
- [6] A. Takeuchi, A. Inoue, Evaluation of glass-forming ability for metallic glasses from time-reduced temperature-transformation diagram, *Materials Transactions* 42 (11) (2001) 2374-2381. DOI <http://doi.org/10.2320/matertrans.42.2374>.
- [7] W.H. Wang, C. Dong, C.H. Shek, Bulk metallic glasses, *Materials Science and Engineering R* 44 (2-3) (2004) 45-89. DOI <http://dx.doi.org/10.1016/j.mser.2004.03.001>.
- [8] K.J. Laws, B. Gun, M. Ferry, Large-scale production of $\text{Ca}_{65}\text{Mg}_{15}\text{Zn}_{20}$ bulk metallic glass samples by low-pressure die-casting, *Materials Science and Engineering: A* 475 (1-2) (2008) 348-354. DOI <http://dx.doi.org/10.1016/j.msea.2007.04.059>.
- [9] A. Brenner, D.E. Couch, E.K. Williams, Electrodeposition of Alloys of Phosphorus with Nickel or Cobalt, *Journal of Research of the National Bureau of Standards* 44 (1) (1950) 109. DOI <http://dx.doi.org/10.6028/jres.044.009>.
- [10] D. Turnbull, M.H. Cohen, Concerning reconstructive transformation and formation of glass, *The Journal of Chemical Physics* 29 (5) (1958) 1049-1054. DOI <http://dx.doi.org/10.1063/1.1744654>.

- [11] M.H. Cohen, D. Turnbull, Molecular transport in liquids and glasses, *The Journal of Chemical Physics* 31 (5) (1959) 1164-1169. DOI <http://dx.doi.org/10.1063/1.1730566>.
- [12] D.R. Uhlmann, Glass formation, *Journal of Non-Crystalline Solids* 23 (1-3) (1977) 42-85. DOI [http://dx.doi.org/10.1016/0022-3093\(77\)90090-4](http://dx.doi.org/10.1016/0022-3093(77)90090-4).
- [13] W. Klement, R.H. Willens, P. Duwez, Non-crystalline structure in solidified gold-silicon alloys, *Nature* 187 (4740) (1960) 869-870. DOI <http://dx.doi.org/10.1038/187869b0>.
- [14] W.L. Johnson, Bulk glass-forming metallic alloys: Science and technology, *MRS Bulletin* 24 (10) (1999) 42-56. DOI <http://dx.doi.org/10.1557/S0883769400053252>.
- [15] A. Inoue, Stabilization of metallic supercooled liquid and bulk amorphous alloys, *Acta Materialia* 48 (1) (2000) 279-306. DOI [http://dx.doi.org/10.1016/S1359-6454\(99\)00300-6](http://dx.doi.org/10.1016/S1359-6454(99)00300-6).
- [16] A. Inoue, B. Shen, N. Nishiyama, Development and applications of late transition metal bulk metallic glasses, in: *Bulk Metallic Glasses*, Springer US, (2008) 1-25. DOI http://dx.doi.org/10.1007/978-0-387-48921-6_1.
- [17] A. Peker, W.L. Johnson, A highly processable metallic glass: $Zr_{41.2}Ti_{13.8}Cu_{12.5}Ni_{10.0}Be_{22.5}$ *Applied Physics Letters* 63 (17) (1993) 2342-2344. DOI <http://dx.doi.org/10.1063/1.110520>.
- [18] C.C. Hays, J. Schroers, W.L. Johnson, T.J. Rathz, R.W. Hyers, J.R. Rogers, M.B. Robinson, Vitrification and determination of the crystallization time scales of the bulk metallic-glass-forming liquid $Zr_{58.5}Nb_{2.8}Cu_{15.6}Ni_{12.8}Al_{10.3}$, *Applied Physics Letters* 79 (11) (2001) 1605-1607. DOI <http://dx.doi.org/10.1063/1.1398605>.
- [19] C.C. Hays, J. Schroers, U. Geyer, S. Bossuyt, N. Stein, W.L. Johnson, Glass forming ability in the Zr-Nb-Ni-Cu-Al bulk metallic glasses, *Journal of Metastable and Nanocrystalline Materials* 8 (2000) (2000) 103-108. DOI <http://dx.doi.org/10.4028/www.scientific.net/MSF.343-346.103>
- [20] C.C. Hays, W.L. Johnson, Undercooling of bulk metallic glasses processed by electrostatic levitation, *Journal of Non-Crystalline Solids* 250 (2) (1999) 596-600. DOI [http://dx.doi.org/10.1016/S0022-3093\(99\)00139-8](http://dx.doi.org/10.1016/S0022-3093(99)00139-8).
- [21] X.H. Lin, W.L. Johnson, Formation of Ti-Zr-Cu-Ni bulk metallic glasses, *Applied Physics Letters* 78 (11) (1995) 6514-6519. DOI <http://dx.doi.org/10.1063/1.360537>.

- [22] J. Schroers, Processing of bulk metallic glass, *Advanced Materials* 22 (2010) 1566-1597. DOI <http://dx.doi.org/10.1002/adma.200902776>.
- [23] H.Y. Jung, S.J. Choi, K.G. Prashanth, M. Stoica, S. Scudino, S. Yi, U. Kühn, D.H. Kim, K.B. Kim, J. Eckert, Fabrication of Fe-based bulk metallic glass by selective laser melting: A parameter study, *Materials & Design* 86 (2015) 703-708. DOI <http://dx.doi.org/10.1016/j.matdes.2015.07.145>.
- [24] H. Sun, Microstructure evolution of bulk metallic glasses via laser processing Doctoral dissertation, The Ohio State University (2010). https://etd.ohiolink.edu/pg_10?0::NO:10:P10_ACCESSION_NUM:osu1287025216.
- [25] T. Terry, G. Tim, History of additive manufacturing, Wohlers Report Wohlers Associates, Inc. <https://wohlersassociates.com/>.
- [26] K.V. Wong, A. Hernandez, A review of additive manufacturing, *ISRN Mechanical Engineering* (2012). DOI <http://dx.doi.org/10.5402/2012/208760>.
- [27] M. Vaezi, H. Seitz, S. Yang, A review on 3D micro-additive manufacturing technologies, *The International Journal of Advanced Manufacturing Technology* 67 (5) (2013) 1721-1754. DOI <http://dx.doi.org/10.1007/s00170-012-4605-2>.
- [28] R.M. Miranda, G. Lopes, L. Quintino, J.P. Rodrigues, S. Williams, Rapid prototyping with high power fiber lasers, *Materials & Design* 29 (10) (2008) 2072-2075. DOI <http://dx.doi.org/10.1016/j.matdes.2008.03.030>.
- [29] ASTM F2792-12a, "Standard terminology for additive manufacturing technologies," ASTM International, West Conshohocken, PA, 2012. DOI <http://dx.doi.org/10.1520/F2792-12A>.
- [30] M. He, K. Song, H. Mo, J. Li, D. Pan, Z. Liang, Progress on photosensitive resins for 3D printing, *Journal of Functional Polymers* 28 (2015) 102-108. DOI <http://dx.doi.org/10.14133/j.cnki.1008-9357.2015.01.018>.
- [31] M. He, Y. Zhao, B. Wang, Q. Xi, J. Zhou, Z. Liang, 3D printing fabrication of amorphous thermoelectric materials with ultralow thermal conductivity, *Small* 11 (44) (2015) 5889-5894. DOI <http://dx.doi.org/10.1002/sml.201502153>.
- [32] G. Tapia, A. Elwany, A review on process monitoring and control in metal-based additive manufacturing, *Journal of Manufacturing Science and Engineering* 136 (6) (2014) 060801. DOI <http://dx.doi.org/10.1115/1.4028540>.

- [33] W.E. Frazier, Metal additive manufacturing: a review, *Journal of Materials Engineering and Performance* 23 (6) (2014) 1917-1928. DOI <http://dx.doi.org/10.1007/s11665-014-0958-z>.
- [34] J.P. Kruth, A.P. Mercelis, A.J. Van Vaerenbergh, A.L. Froyen, A.M. Rombouts, Binding mechanisms in selective laser sintering and selective laser melting, *Rapid Prototyping Journal* 11 (1) (2005) 26-36. DOI <http://dx.doi.org/10.1108/13552540510573365>.
- [35] X. Gong, T. Anderson, K. Chou, Review on powder-based electron beam additive manufacturing technology, *Manufacturing Review* 1 (2014) 507-515. DOI <http://dx.doi.org/10.1051/mfreview/2014001>.
- [36] S. Kumar, J.P. Kruth, Composites by rapid prototyping technology, *Materials & Design*, 31 (2) (2010) 850-856. DOI <http://dx.doi.org/10.1016/j.matdes.2009.07.045>.
- [37] D.D. Gu, W. Meiners, K. Wissenbach, R. Poprawe, Laser additive manufacturing of metallic components: materials, processes and mechanisms, *International Materials Reviews* 57 (3) (2012) 133-164. DOI <http://dx.doi.org/10.1179/1743280411Y.0000000014>.
- [38] P. Skoglund, A. Langlet, Method of producing objects containing nano metal or composite metal, U.S. Patent No. 8333922 B2.
- [39] Y.Y. Zhang, X. Lin., L.L. Wang, L. Wei, F.G. Liu, W.D. Huang, Microstructural analysis of Zr₅₅Cu₃₀Al₁₀Ni₅ bulk metallic glasses by laser surface remelting and laser solid forming *Intermetallics* 66 (2015) 22-30. DOI <http://dx.doi.org/10.1016/j.intermet.2015.06.007>.
- [40] S. Pauly, L. Löber, R. Petters, M. Stoica, S. Scudino, U. Kühn, J. Eckert, Processing metallic glasses by selective laser melting, *Materials Today* 16 (1) (2013) 37-41. DOI <http://dx.doi.org/10.1016/j.mattod.2013.01.018>.
- [41] B. Li, Z.Y. Li, J.G. Xiong, L. Xing, D. Wang, Y. Li, Laser welding of Zr₄₅Cu₄₈Al₇ bulk glassy alloy, *Journal of Alloys and Compounds* 413 (1-2) (2006) 118-121. DOI <http://dx.doi.org/10.1016/j.jallcom.2005.07.005>.
- [42] J.H. Kim, C. Lee, D.M. Lee, J.H. Sun, S.Y. Shin, J.C. Bae, Pulsed Nd: YAG laser welding of Cu₅₄Ni₆Zr₂₂Ti₁₈ bulk metallic glass, *Materials Science and Engineering: A* 449 (2007) 872-875. DOI <http://dx.doi.org/10.1016/j.msea.2006.02.323>.

- [43] G. Wang, Y.J. Huang, M. Shagiev, J. Shen, Laser welding of $\text{Ti}_{40}\text{Zr}_{25}\text{Ni}_3\text{Cu}_{12}\text{Be}_{20}$ bulk metallic glass, *Materials Science and Engineering: A* 541 (2012) 33-37. DOI <http://dx.doi.org/10.1016/j.msea.2012.01.114>.
- [44] C. Chen, Y. Shen, H.L. Tsai, A foil-based additive manufacturing technology for metal parts, *ASME Journal of Manufacturing Science and Engineering*, 139 (2) (2016) 024501-1 – 024501-6. DOI <http://dx.doi.org/10.1115/1.4034139>.
- [45] Y. Kawahito, T. Terajima, H. Kimura, T. Kuroda, K. Nakata, S. Katayama, A. Inoue, High-power fiber laser welding and its application to metallic glass $\text{Zr}_{55}\text{Al}_{10}\text{Ni}_5\text{Cu}_{30}$, *Materials Science and Engineering: B* 148 (1) (2008) 105-109. DOI <http://dx.doi.org/10.1016/j.mseb.2007.09.062>.
- [46] H.S. Wang, H.G. Chen, J.S.C. Jang, M.S. Chiou, Combination of a Nd: YAG laser and a liquid cooling device to $(\text{Zr}_{53}\text{Cu}_{30}\text{Ni}_9\text{Al}_8)\text{Si}_{0.5}$ bulk metallic glass welding, *Materials Science and Engineering: A* 528 (1) (2010) 338-341. DOI <http://dx.doi.org/10.1016/j.msea.2010.09.014>.
- [47] H.S. Wang, H.G. Chen, J.S.C. Jang, Microstructure evolution in Nd: YAG laser-welded $(\text{Zr}_{53}\text{Cu}_{30}\text{Ni}_9\text{Al}_8)\text{Si}_{0.5}$ bulk metallic glass alloy, *Journal of Alloys and Compounds* 495 (1) (2010) 224-228. DOI <http://dx.doi.org/10.1016/j.jallcom.2010.01.132>.
- [48] H.S. Wang, M.S. Chiou, H.G. Chen, J.S.C. Jang, J.W. Gu, Microstructure evolution of the laser spot welded Ni-free Zr-based bulk metallic glass composites, *Intermetallics* 29 (2012) 92-98. DOI <http://dx.doi.org/10.1016/j.intermet.2012.05.013>.
- [49] J. Kim, D. Lee, S. Shin, C. Lee, Phase evolution in $\text{Cu}_{54}\text{Ni}_6\text{Zr}_{22}\text{Ti}_{18}$ bulk metallic glass Nd: YAG laser weld, *Materials Science and Engineering: A* 434 (1) (2006) 194-201. DOI <http://dx.doi.org/10.1016/j.msea.2006.06.118>.
- [50] B.A. Sarsfield, M. Davidovich, S. Desikan, M. Fakes, S. Futernik, J.L. Hilden, J.S. Tan, S. Yin, G. Young, B. Vakkalagadda, K. Volk, Powder X-ray diffraction detection of crystalline phases in amorphous pharmaceuticals, *Powder Diffraction* 20 (02) (2005) 178-178. DOI: <http://dx.doi.org/10.1154/1.1968282>.
- [51] M.F. Haque, Effect of continuous wave laser irradiation on structural relaxation and mechanical properties of iron-silicon-boron amorphous ribbon, M.S. dissertation, Oklahoma State University, (2013). <https://shareok.org/handle/11244/14870>.

- [52] Y. Huang, B. Zhou, Y. Chiu, H. Fan, D. Wang, J. Sun, J. Shen, The structural relaxation effect on the nanomechanical properties of a Ti-based bulk metallic glass, *Journal of Alloys and Compounds* 608 (2014) 148-152. DOI <http://dx.doi.org/10.1016/j.jallcom.2014.04.112>.
- [53] R. Raghavan, P. Murali, U. Ramamurty, Influence of cooling rate on the enthalpy relaxation and fragility of a metallic glass, *Metallurgical and Materials Transactions A* 39 (7) (2008) 1573-1577. DOI <http://dx.doi.org/10.1007/s11661-007-9262-y>.
- [54] M. Rombouts, L. Froyen, A.V. Gusarov, E.H. Bentefour, C. Glorieux, Photopyroelectric measurement of thermal conductivity of metallic powders, *Journal of Applied Physics* 97 (2) (2005) 024905. DOI <http://dx.doi.org/10.1063/1.1832740>.
- [55] W.H. Wang, L.L. Li, M.X. Pan, R.J. Wang, Characteristics of the glass transition and supercooled liquid state of the $Zr_{41}Ti_{14}Cu_{12.5}Ni_{10}Be_{22.5}$ bulk metallic glass, *Physical Review B* 63 (5) (2001) 052204. DOI <http://dx.doi.org/10.1103/PhysRevB.63.052204>.
- [56] M. Yamasaki, S. Kagao, Y. Kawamura, Thermal diffusivity and conductivity of $Zr_{55}Al_{10}Ni_5Cu_{30}$ bulk metallic glass, *Scripta Materialia* 53 (1) (2005) 63-67. DOI <http://dx.doi.org/10.1016/j.scriptamat.2005.03.021>.
- [57] Q.K. Jiang, X.D. Wang, X.P. Nie, G.Q. Zhang, H. Ma, H.J. Fecht, J. Bendnarcik, H. Franz, Y.G. Liu, Q.P. Cao, J.Z. Jiang, Zr-(Cu, Ag)-Al bulk metallic glasses, *Acta Materialia* 56 (8) (2008) 1785-1796. DOI <http://dx.doi.org/10.1016/j.actamat.2007.12.030>.
- [58] J. Zhang, H.F. Zhang, M.X. Quan, Z.Q. Hu, effect of pressure on crystallization process of $Zr_{55}Al_{10}Ni_5Cu_{30}$ bulk metallic glass, *Materials Letter* 58 (7-8) (2004) 1389-1382. DOI <http://dx.doi.org/10.1016/j.matlet.2003.09.031>.

II. EVOLUTION OF CRYSTALLINE PHASE DURING LASER PROCESSING OF ZR-BASED METALLIC GLASS

Yiyu Shen, Yingqi Li, and Hai-Lung Tsai

Department of Mechanical and Aerospace Engineering

Missouri University of Science and Technology, Rolla, Missouri 65409, U.S.A.

ABSTRACT

Understanding the crystallization behavior of metallic glasses (MGs) during laser processing is important in additive manufacturing of MGs, which would overcome the section-thickness limitation. Experiments were conducted to study the crystalline phase evolution, particularly in the heat-affected zone (HAZ), during laser processing of LM105 ($Zr_{52.5}Ti_5Al_{10}Ni_{14.6}Cu_{17.9}$ (at. %)) MG plates. Three distinct regions in HAZ with different distributions of crystalline phases were found, which were caused by different thermal histories. The crystallization can be suppressed, however, by increasing the laser scan speed (100 mm/s in this study) while the laser power is fixed (100 W in this study). A complete model integrating the heat transfer and the classical nucleation/growth theory was developed to calculate the thermal history and the crystalline volume fraction evolution. Modeling predictions on the depth of fusion zone (FZ) and thickness of HAZ for different laser processing parameters were validated by comparing with the experimental measurements. This study has demonstrated that at a specific location in the MG material, the critical cooling rate alone is not adequate to determine if the material is crystallized; instead the thermal history that the material experiences during both the laser heating and cooling processes would determine the final crystallization. The model provides comprehensive understanding of the crystallization behavior during laser-MG interaction.

Keywords: Metallic glass, Laser material processing, Modeling, Crystallization

1. INTRODUCTION

Metallic glasses (MGs) have gained much research interest in recent decades due to their outstanding properties such as high tensile strength, hardness, wear resistance, and corrosion resistance [1–5]. From its molten state, an MG alloy must be cooled fast enough in order to prevent itself from crystallization, which is usually denoted as the critical cooling rate (R_c). By modifying the alloy compositions, material scientists have decreased the critical cooling rate from approximately 10^6 K/s when MGs were first discovered in the 1960s to less than 10 K/s nowadays [6,7].

Laser is a promising tool for processing MG alloys. In laser material processing (such as laser welding, cutting, or surface modification), as laser energy is tightly focused and controlled, the induced heating and cooling rates in materials are very high ($10^3\sim 10^5$ K/s) [8]. Non-contact processing of laser is also beneficial, which prevents, for example, possible heterogeneous crystallization from MG-mode contact. In laser-processed metals, there generally exists three zones: the fusion zone (FZ), where the material is once melted and re-solidified; the heat-affected zone (HAZ), where the material stays solid but is somehow affected by the heat from laser/molten metal; and the unaffected zone.

Laser processing of MGs has been studied intensively in recent years. Sun [9] investigated the microstructure evolution of Vitreloy 106a MG processed by laser engineered net shaping (LENS) technology. He claimed that although the required critical cooling rate to avoid crystallization is about 1.5 K/s, the crystallization phenomenon in HAZ took place even at a cooling rate as high as 10^3 K/s due to the complex thermal history that the material experienced. Thus, the main challenge is to prevent crystallization in HAZ rather than that in FZ. Zhang [10] and coworkers had discovered a similar phenomenon in

powder-based selected laser melting (SLM) and laser solid forming (LSF) additive manufacturing (AM) technologies.

Vora [11] conducted a detailed study on the laser-MG interaction based on the heat transfer theory. The crystallization was observed in the experiment even though the predicted temperature history remains far away from touching the TTT curve. Lu [12] separated the heating and cooling history during laser-MG interaction, and then compared them with the critical heating and cooling rate, respectively. By doing this, Lu pointed out that the crystallization during laser-MG interaction mainly happened in the HAZ during the heating process. There are some other similar studies [13–15] and all have yielded that crystallization in HAZ is the main problem in laser-MG interaction. Therefore, it is vital to understand the crystallization behavior of MG during laser processing, particularly in HAZ, which is different from that during casting [16-19]. More importantly, most presented works used an estimated cooling or heating rate as the criterion of crystallization rather than looking into the physics behind the crystallization process. The critical cooling rate is a simplified factor that is widely used for the casting process, but whether it is also suitable for the laser process remains questionable.

In this paper, the evolution of crystalline phase during laser processing of Zr-based MGs is investigated. For this purpose, we designed an experiment that looked into the HAZ evolution during laser processing at different laser parameters. To understand the mechanism behind it, a heat transfer model is developed to obtain the thermal history that is integrated with the classical nucleation/growth theory for the calculation of crystalline phase as a function of time and location in the MG during laser processing.

2. EXPERIMENTAL

An alloy, LM105 ($Zr_{52.5}Ti_5Al_{10}Ni_{14.6}Cu_{17.9}$ (at. %)), cast by Liquidmetal Technologies, Inc., was used in this study. The as-cast bulk samples with a thickness of 0.75 mm were machined to the dimensions of 10 mm in both length and width. The samples' surfaces were polished with 800-grit SiC paper right before the laser welding experiment (bead on plate).

The laser used in this study was a continuous-wave (CW) fiber laser (model YLR-1000, IPG Photonic Corp.) with a wavelength of 1070 μm . The laser beam diameter D on the focal plane was 430 μm . The motion of the laser beam was controlled by a scanner (hurrySCAN III, SCANLAB) with the maximum scan speed of 2000 mm/s at the focal plane. All experiments were conducted in an argon-shielded chamber. For the purpose of finding the suitable processing parameters, the laser power (P) was set to a constant 100 W, while the laser scan speed (v) was varied from 10 mm/s to 500 mm/s. To keep the phenomenon simple, the laser power was kept low to minimize possible fluid behavior.

The evaluation of the laser-processed MG was performed using optical microscopy (OM). To gather good images, the laser-processed MG samples were cross-sectioned, polished, and etched by a solution of 100 ml H_2O , 2 ml H_2O_2 , and 0.1 ml HF for 10 s. The freeware imageJ was used to analyze the volume fraction of crystalline phase. Microhardness tests were conducted on the cross section with 0.5 kgf load and 10 s duration (Duramin 5, Struers Inc.).

3. RESULTS AND DISCUSSION

Figure 1 shows the top and cross-sectional views that a laser beam scans along the top surface of an MG plate at laser power $P = 100$ W and scan speed $v = 10$ mm/s. As shown in Fig. 1(a), the FZ was measured as $700 \mu\text{m}$ wide, and the HAZ was measured as $100 \mu\text{m}$ wide. From Fig. 1(b), the depth of FZ was measured as $235 \mu\text{m}$ along the vertical centerline. The thickness of the HAZ reached a maximum of approximately $140 \mu\text{m}$ directly below the FZ. The pre-existing micro-crystalline (MC) phases, shown as the dark-spots in the image, can be clearly seen, which are embedded in the amorphous matrix. For the as-cast LM105, the volume fraction (VF) of the MC crystalline was measured as 2.14% based on the OM image of the etched cross section surface with ImageJ [20–23]. The selected area in HAZ in Fig. 1(b) is enlarged and shown in Fig. 1(c). There are clearly three distinct regions in HAZ. In region I, there are no obvious MC particles observed, and its thickness is $16.0 \mu\text{m}$. In region II, however, spherical-like MC crystals can be observed with an average diameter of $4.34 \mu\text{m}$. The thickness of region II is $64.4 \mu\text{m}$. In region III, sub-size crystalline phases can be clearly seen. The average diameter of the crystalline phase in region III is $1.34 \mu\text{m}$. The thickness of region III is $53.8 \mu\text{m}$. Note, the thickness of HAZ also depends on the direction of measurement. In order to keep consistent with further discussion, the downward direction for the measurement of HAZ thickness, as shown in Fig. 1(b), is used for the entire work. The distinct appearances of the three regions in HAZ are believed to be caused by different thermal histories during laser processing. Materials in region I are closest to FZ, so they experience a temperature that is close to the melting temperature of 1085 K [17]. This the temperature range where both nucleation and crystal grow are low, resulting in a relatively small crystal size (to be discussed in detail in

the model part). In region II, materials are rapidly heated to around 1000 K, at which point the crystal growth rate is near maximum (see Fig. 3; the maximum crystal growth rate is about 1030 K), and as a result, the size of the crystalline phase is larger than those in the other two regions. In region III, the materials reach the temperature at which the nucleation rate is near maximum (see Fig. 3; the maximum nucleation rate is about $5 \cdot 10^{14} \text{ m}^{-3}\text{s}^{-1}$ at the temperature of about 780 K). Hence, dense but smaller crystalline phases are expected. To understand the aforementioned phenomena, detailed analysis and explanation are included in the next section with the help of mathematical modeling.

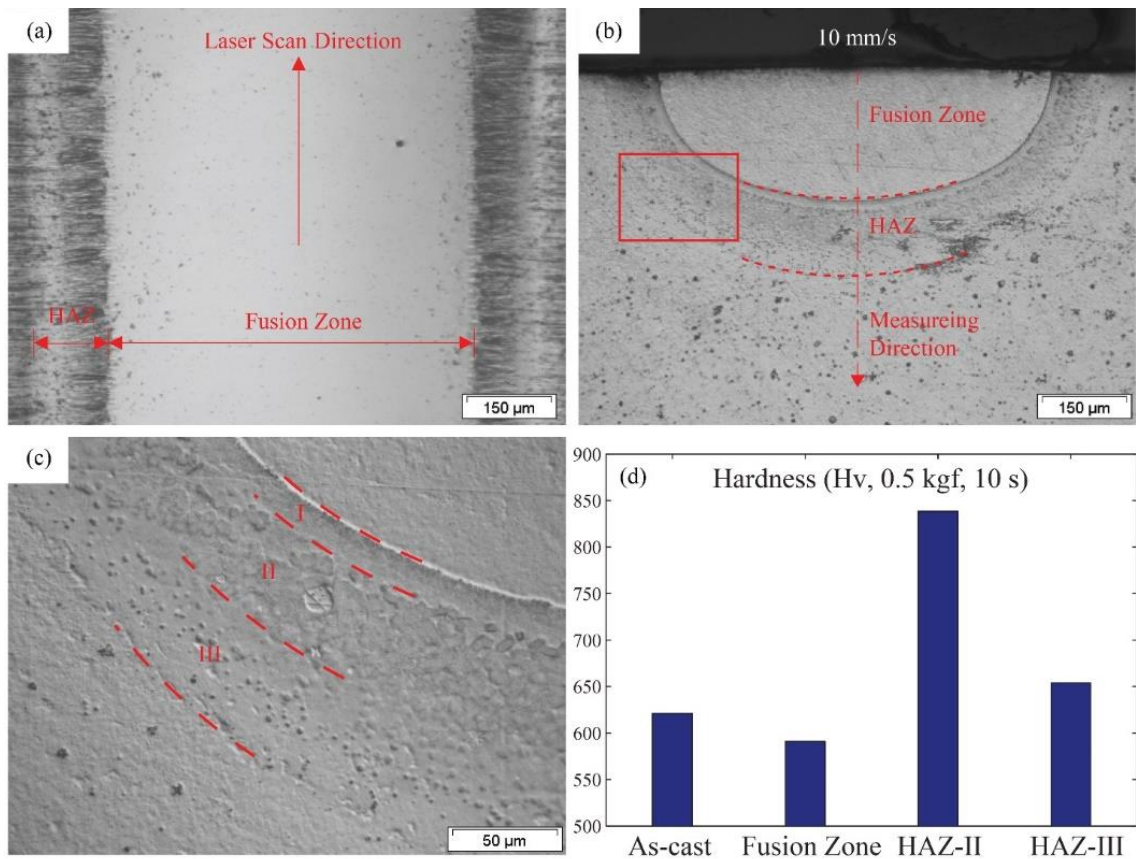


Figure 1. Top and cross-sectional OM images of a laser scanned MG; inset in Fig. 1(b) is an SEM image (X 2500); $P = 100 \text{ W}$ and $v = 10 \text{ mm/s}$.

The measured micro-hardness values are presented in Fig. 1(d). For Zr-based metallic glass alloys, the hardness of amorphous phase is close to 600 Hv, while the hardness increases to around 800 Hv after crystallization [9]. For the as-cast part, the hardness was measured as 610 Hv. For the laser processed sample, the hardness in FZ was measured as 590 Hv. The as-cast part has a slightly higher hardness because of the 2.14% MC phases embedded in the amorphous matrix. The lower hardness in FZ also implies that in FZ the possible crystallization was suppressed during the laser process. Limited by the size, only regions II and III in HAZ were tested for hardness. In region II, the hardness was measured as 830 Hv, which indicates the materials in region II were seriously, if not fully, crystallized during the laser process. The hardness in region III, however, was measured as 650 Hv. This indicates that in region III, there are more amorphous phases than that in region II. In general, the hardness results discussed above are consistent with the observation from the optical image.

Figure 2 shows laser processed cross sections at the laser power $P = 100$ W and laser scan speed $v = 30, 50,$ and 100 mm/s, respectively, for Figs. 2(a), 2(b), and 2(c). As expected, at constant laser power, the size of FZ decreases with the increase of laser scan speed. Fig. 2(d) is an enlarged image for $v = 100$ mm/s in Fig. 2(c). The size of HAZ also decreases with the increase of v . The HAZ is no longer observable in Figs. 2(c) and 2(d). Further increase of the laser scan speed causes a dramatic decrease of the size of FZ, and thus there is no need to increase the laser scan speed beyond 100 mm/s any further. From the results of Fig. 2, it can be concluded that the size of crystallized HAZ can be reduced/eliminated if proper laser processing parameters are selected.

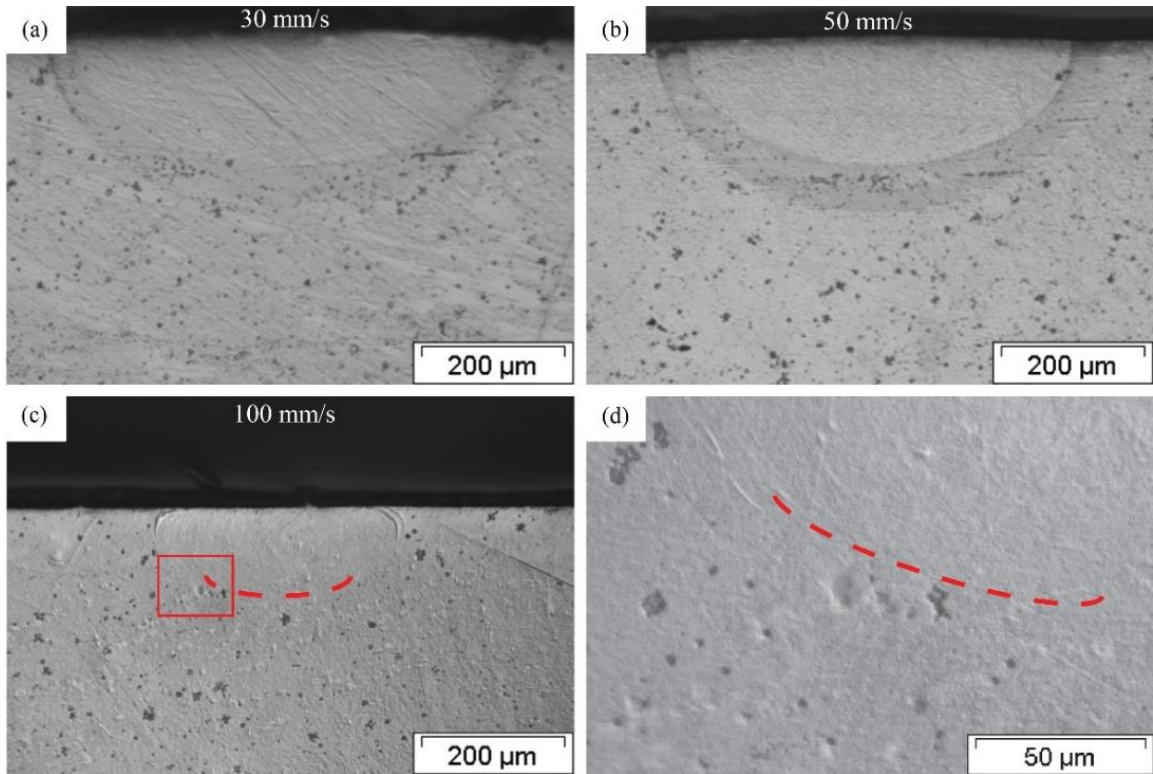


Figure 2. Cross-sectional OM images of laser-processed MG; $P = 100$ W, (a) $v = 30$ mm/s, (b) $v = 50$ mm/s, and (c) $v = 100$ mm/s.

4. MODELING AND ANALYSIS

The crystallization behavior in laser processing of MG is more complex than that in the casting process. During the casting process, crystallization starts from the molten phase, and hence the formation of the crystalline phase can be solely determined by the critical cooling rate from molten phase to solid. In laser processing of MG, however, the temperature first rapidly rises from room temperature to melting, and then is followed by rapid cooling to below the glass transition temperature. As a result, in laser MG processing, materials experience a more complex thermal history than that during the casting process. Thus, the use of a critical cooling rate to determine if crystalline phases have been formed may not be accurate. To better understand the crystallization evolution during laser processing of MG, we choose to describe the crystallization behavior by the classical nucleation theory (CNT). A heat transfer model is developed to calculate the thermal history during laser processing. Then, the CNT model is developed to calculate the evolution of crystalline phases in the amorphous matrix.

The heat transfer model and the related assumptions and validation have been given in our previous paper [24]. However, to facilitate the following discussion, it is briefly introduced below. For heat conduction, the governing differential equation can be written as (1):

$$\frac{\partial}{\partial x} \left(k \frac{\partial T}{\partial x} \right) + \frac{\partial}{\partial y} \left(k \frac{\partial T}{\partial y} \right) + \frac{\partial}{\partial z} \left(k \frac{\partial T}{\partial z} \right) = \rho C_p \frac{\partial T}{\partial t} \quad (1)$$

where T denotes the temperature, t is the time, k is the thermal conductivity, ρ is the material density, and C_p is the specific heat. The heat losses from the part's surfaces to the surroundings are assumed to be thermal radiation and heat convection:

$$-k \frac{\partial T}{\partial n} = \epsilon \sigma (T^4 - T_\infty^4) + h(T - T_\infty) \quad (2)$$

where n is the normal direction to the surface, ϵ is the surface emissivity, σ is the Stefan-Boltzmann constant, and h is the convective heat transfer coefficient. The laser energy input is assumed to be a Gaussian distribution at the top surface, which is expressed as (3):

$$I_{laser} = \alpha \cdot \frac{2 \cdot P}{\pi r^2} \cdot e^{\frac{-2[(x-vt)^2 + y^2]}{r^2}} \quad (3)$$

where I_{laser} represents the laser power density, α is the surface absorptivity, P is the laser power, r is the laser beam radius, and v is the laser scan speed. To compute the model, the x-, y-, z-coordinate system was established. The calculated domain was x (-5 mm, 5 mm), y (-5 mm, 5 mm), and z (0 mm, -0.75 mm). The laser scanned from (x = -5 mm, y = 0 mm, z = 0 mm) toward the positive x direction. From the heat transfer model, the temperature history at any location can be calculated.

For the nucleation model, the classical nucleation rate is written as (4) [25]:

$$I(T) = A \cdot D \cdot \exp\left(-\frac{\Delta G^*}{kT}\right) \quad (4)$$

where I is the nucleation rate, A is a constant, D is the effective diffusivity, k is Boltzmann's constant, T denotes the absolute temperature, and ΔG^* is the thermodynamic potential barrier of nucleation that obeys the following relation:

$$\Delta G^* = \frac{16\pi\sigma^3}{3\Delta G^2} \quad (5)$$

where σ denotes the interface energy between the nucleus and melt, and ΔG is the difference of the Gibbs free energy between the solid and liquid (amorphous) phase. The diffusion limited crystalline growth velocity U can be expressed by the following equation [25]:

$$U(T) = \frac{D}{a} \left[1 - \exp\left(-\frac{\Delta G}{kT}\right)\right] \quad (6)$$

where a is the average interatomic spacing. Considering diffusion limited crystal growth, the 3D time-dependent VF of crystallized phase $X(t)$ is expressed in (7) [9,26]:

$$X(t) = 1 - \exp \left\{ -\frac{4\pi}{3} \cdot \left[\int_0^t I(T, \tau) \cdot \left[\int_\tau^t U(T, t') dt' \right]^3 d\tau + N \cdot \left[\int_0^t U(T, t'') dt'' \right]^3 \right] \right\} \quad (7)$$

where I and U are each a function of temperature T . As T is a function of time and location from the heat transfer model, I and U are each a function of time and location. The symbol N represents the pre-existing nucleus density (unit in m^{-3}) in the sample. It is reset to 0 when $T > T_m$ due to melting, where $T_m = 1085$ K is used in this paper.

The aforementioned equations were numerically solved with the parameters determined below. Calculated from the weighted atomic percentage of LM105 alloy, the average interatomic spacing a of 2.6×10^{-7} mm was used. The temperature dependent effective diffusivity, D , was estimated from measured viscosity [27] by a method introduced in Refs [26,28]. This method employed a hybrid function, based on the Stork-Einstein relation, to fit the experimental results at high and low temperature ranges. The Gibbs free energy difference between undercooled liquid and corresponding crystal solid, ΔG , as a function of temperature given in [29] was used. The reported nose temperature of 860 K from [30] was used. By evaluating the maximum value of $I \times U^3$, which corresponds to the nose temperature in the TTT curve, σ can be determined as 0.076 J/m² [31]. Then, with the experimentally measured TTT data [26,30], the constant A was determined by running Eq. (7) with $N = 0$ at the nose temperature and examining the time of crystallization. The constant A was found to be 2.5×10^{33} . Using the VF of the crystalline phase in the sample (2.14%), the equivalent average cooling rate for casting the sample

was estimated of 50 K/s. Then, by integrating the nucleation rate w.r.t. time, N was found to be $1 \times 10^{14} \text{ m}^{-3}$. With the temperature history obtained from the heat transfer model and the thermal dynamic properties calculated from Eqs. (4) and (6), the VF of the crystalline phase, $X(t)$, as a function of time can be computed by Eq. (7). Note the aforementioned modeling analyses will not be affected by the initial VF of crystalline phase in the sample.

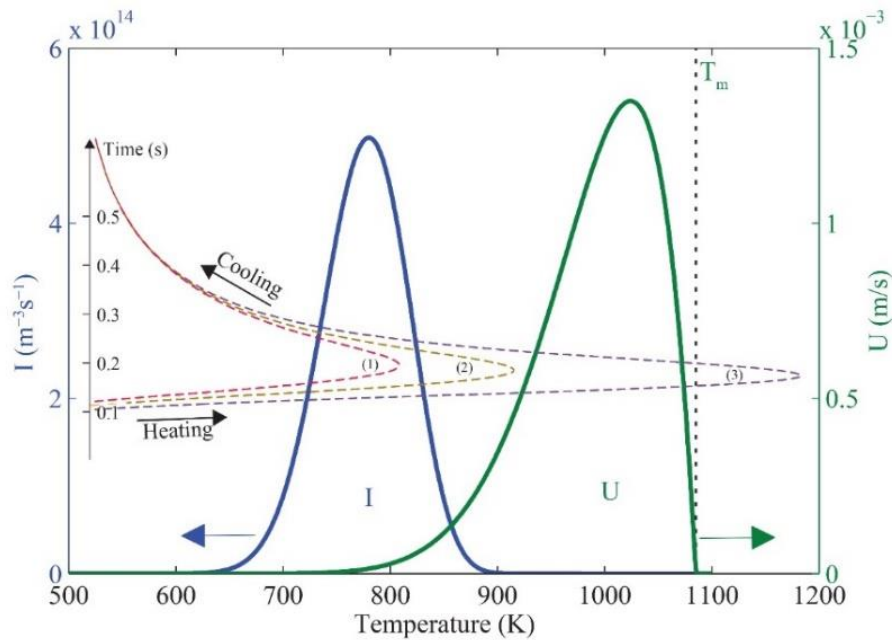


Figure 3. The calculated nucleation rate ($I(T)$) and crystalline growth rate ($U(T)$) as a function of temperature. Dashed lines: the calculated temperature history at different locations; Curve (1): bottom of HAZ (region III in Fig. 1(c)); Curve (2): middle of HAZ (region II in Fig. 1(c)); and Curve (3): FZ in Fig. 1(c). $P = 100 \text{ W}$ and $v = 10 \text{ mm/s}$.

Figure 3 plots the calculated I and U as a function of temperature for the LM105 alloy. The maximum nucleation rate occurs at around 780 K. On the other hand, the maximum crystal growth rate occurs at around 1030 K, and then drops rapidly to 0 at the

melting temperature $T_m = 1085$ K. Figure 3 also plots the calculated temperature histories for three points in the sample at laser power $P = 100$ W and scan speed $v = 10$ mm/s. Curve (1) represents the heating and cooling for point $(0, 0, -0.35)$, which is located in HAZ but far away from FZ (region III in Fig. 1(c)). The material is heated to about 810 K in 0.1 second and then followed by rapid cooling to back below 500 K in around 0.5 s. As shown in Fig. 3, Curve (1) experiences much nucleation, $I(T)$, while only a little bit of crystal growth, $U(T)$, which implies that there would be a higher amount but small particle size of crystalline phase generated in region III of Fig. 1(c). The point $(0, 0, -0.3)$, as presented in Curve (2) of Fig. 3 (region II in Fig. 1(c)), reaches about 920 K. This is the temperature where U is high, and one would expect larger sizes of crystalline phase to be observed here. For Curve (3), which is located in FZ $(0, 0, -0.18)$, the temperature exceeds the melting temperature in around 0.05 s. It is reasonable to assume that all crystalline phases/amorphous nuclei will be melted while melting occurs (see also in Fig. 4). In the cooling process for Curve 3, the liquid alloy first experiences the temperature range in which U is very high, 920 K - 1080 K. However, as it is free of nuclei in the newly solidified alloy, the growth of crystalline phase is not significant. Then, the alloy experiences the temperature range where nucleation is high, but the growth is low, leading to a certain amount of nuclei in the alloy after cooling to room temperature. The aforementioned discussions explain and are consistent with the results obtained from experiments shown in Fig. 1 at different locations in the sample.

As shown in Fig. 3, if an amorphous alloy is cooling down from its molten state, because there is no or low nucleation site when the cooling curve hits the crystal growth curve, the volume fraction of crystalline phase $X(t)$ is very minimum until it hits the

nucleation curve $I(t)$, at which nucleation sites start to be generated. However, at this time the crystal growth rate decreases, and hence the $X(t)$ is limited. The dependence of $X(t)$ is not very critical for cooling from the molten state, particularly during the manufacturing process (e.g., mold casting). However, if a solid amorphous alloy is heated up from room temperature, then both the heating and cooling rates would be very critical. Hence, in laser processing, if a point is located in the HAZ, its thermal history would pass through the $I(t)$ and $U(t)$ curves twice, one for during heating and another for during cooling, and hence the accumulated $X(t)$ is great. This explains the reason why crystallization may occur in HAZ for laser MG processing even though the cooling rate is much higher than the critical cooling rate for amorphous phase [9–13].

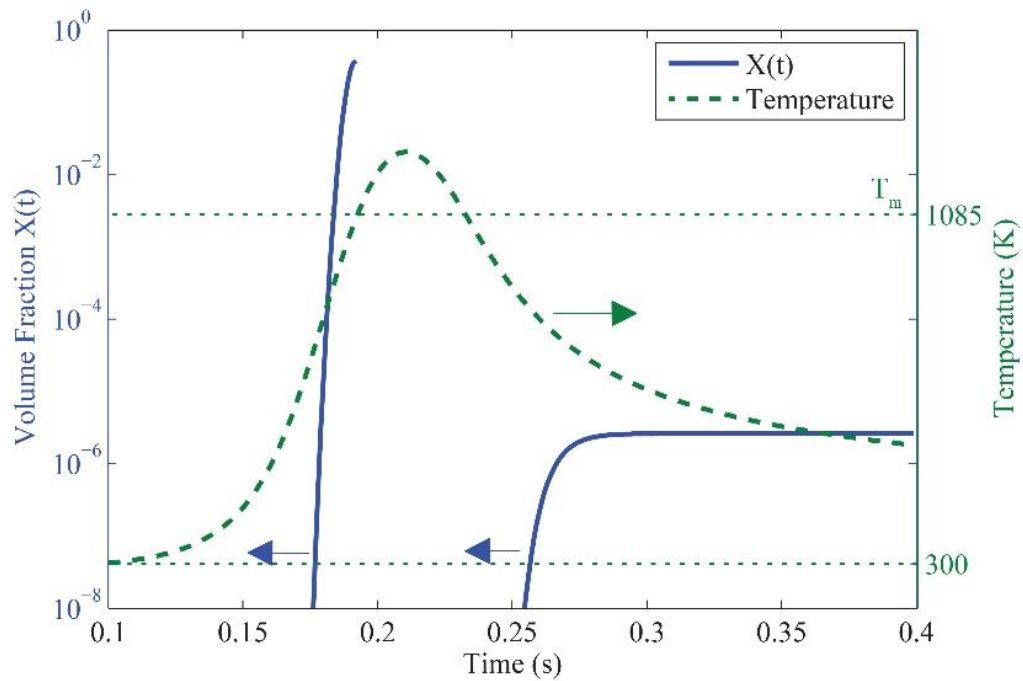


Figure 4. Calculated evolution of volume fraction of crystalline phase in FZ.

Based on the aforementioned discussion, it is easy to understand that the pre-existing nucleus density, N , would have a significant effect on the formation of crystalline phase in HAZ.

Figure 4 shows the calculated $X(t)$ in FZ for the same condition shown in Fig. 1(b) with laser power $P = 100$ W and scan speed $v = 10$ mm/s. The location studied is $(0, 0, -0.18)$, the same as Curve (3) in Fig. 3, which is located in the FZ (the calculated depth of the fusion zone is $230 \mu\text{m}$ from the top surface). The dashed curve represents the temperature history from the heat transfer model. The “discontinued” solid curve in Fig. 4 represents the evolution of $X(t)$ as a function of time. The VF of crystalline phase increases rapidly upon heating to about 38% at $t = 0.192$ s. Then, melting starts and clears the crystalline/nuclei at $t = 0.192$ to 0.232 s. Upon cooling and starting at $t = 0.232$ s, $X(t)$ grows from 0 again and ends up with a near constant value of 2.6×10^{-6} at $t = 0.4$ s. The final residual nucleus density in the sample, N_{res} , is calculated as $2.23 \times 10^{13} \text{ m}^{-3}$, which is only 22% as compared to the initial nucleus density $N = 1 \times 10^{14} \text{ m}^{-3}$. This number of residual nucleus density is equivalent to the pre-existing nucleus density for the later thermal circles.

Figure 5 plots the evolution of VF of crystalline $X(t)$ at different locations in HAZ shown in Fig. 1(b) with $P = 100$ W and $v = 10$ mm/s. In the experiment, the depth of FZ was measured as $235 \mu\text{m}$ and followed by a $140 \mu\text{m}$ thick HAZ (also see in Fig. 8). In the modeling, the depth of FZ was calculated as $230 \mu\text{m}$.

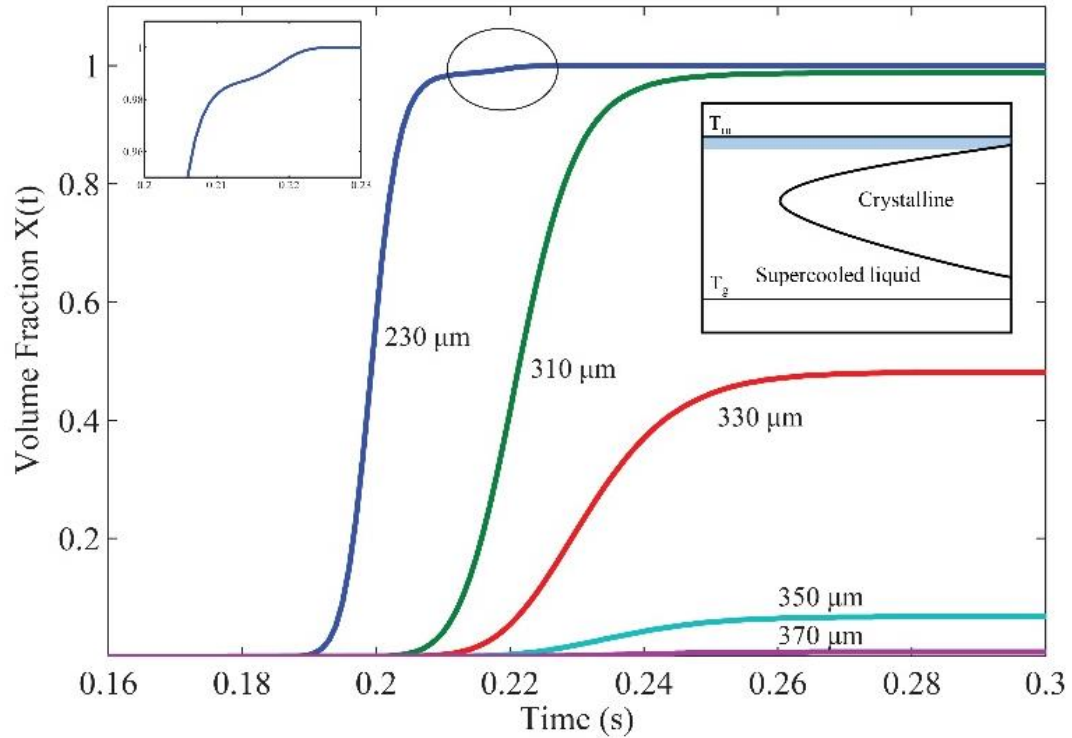


Figure 5. Calculated evolution of volume fraction of crystalline in HAZ at different depths.

As shown in Fig. 5, at a point in HAZ and just right below the FZ (i.e., 230 μm depth), $X(t)$ grows to 100% rapidly. In the FZ, melting occurred, which is able to reset the crystalline percentage back to 0. However, the value of $X(t)$ at any other location in HAZ increases and then reaches a steady-state constant value through the entire heating-cooling process. The final VF of crystalline phase ends up with 98.82%, 48.14%, 6.74%, and 0.76% at the depth of 310 μm , 330 μm , 350 μm , and 370 μm , respectively. At the depth of 370 μm , $X(t)$ is considered to be undetectable ($0.76\% < 2\%$). Thus, the calculated thickness of HAZ is around 135 μm ($\sim 365\ \mu\text{m}$ minus 230 μm), which agrees with the experimental value of 140 μm , as shown in Fig. 1(b).

The curve at the depth of 230 μm from $t = 0.21$ to $t = 0.23$ s, as shown in the enlarged inset on the top left, indicates a “dent” in the crystallization rate curve between $t = 0.21$ s and 0.22 s. This “retardation of crystallization” is in fact expected [32] and can be well explained with the help of Fig. 3. In Fig. 3, it can be seen that for temperatures below (but close to) T_m (e.g., 1035 K to $T_m = 1085$ K), the crystal growth rate, $U(t)$, decreases rapidly from its maximum to almost 0. Hence, for a point in HAZ and next to FZ that has heating history such that the maximum temperature is very close to the melting point (but not yet melted), the crystallization process suddenly “freezes.” Then, the crystallization process resumes as the cooling starts, resulting in a “dent” in the crystallization rate curve. The retardation of crystallization is also frequently observed from the well-known TTT curve of metallic glasses. As can be seen in the right inset image of Fig. 5, at temperatures just below T_m (the shaded area), the supercooled liquid can stay in its amorphous status for a long time because of the frozen of crystallization process. Thus, to the position next to FZ, the average crystalline size is expected to be smaller. This phenomenon may be only observed under rapid heating/cooling to the sub-melting temperatures, such as in laser welding. Under relatively slow heating/cooling, full crystallization would already be reached before the temperature gets high enough [33]. An example is given in Fig. 6 where the final VF of crystalline phase is plotted as a function of depth from the surface, as shown in the inset, for laser scan speeds of 10 and 30 mm/s. Note a slow laser scan speed (i.e., 10 mm/s) will lead to a slow heating/cooling rate. The region on the left where VF = 0 represents the fusion zone. For $v = 10$ mm/s, the VF of crystalline phase reaches 100% at a depth of 223 μm , which is the start of HAZ just below the FZ. With the increase of depth, the VF of crystalline phase first keeps steady (100%) and then starts to drop at a depth of

about 280 μm to below 2% at a depth of 346 μm . If the criteria of full amorphous is set to be the final VF of crystalline phase $< 2\%$, the thickness of HAZ is measured as 123 μm (346 μm minus 223 μm) under laser scan speed $v = 10$ mm/s. On the other hand, for scan speed $v = 30$ mm/s, the final VF of crystalline is found to be about 43% right below FZ at a depth of 175 μm . It is noticed that the final VF of crystalline phase increases to about 50% at a depth of about 182 μm and then drops back to 0 for higher depths, resulting in an HAZ thickness of 72 μm (247 μm minus 175 μm). The maximum VFs of crystalline phase at other laser scan speeds are given in Fig. 7. As calculated, when the laser scan speed is about 17 mm/s or lower, the maximum VF of crystalline phase reaches 100%.

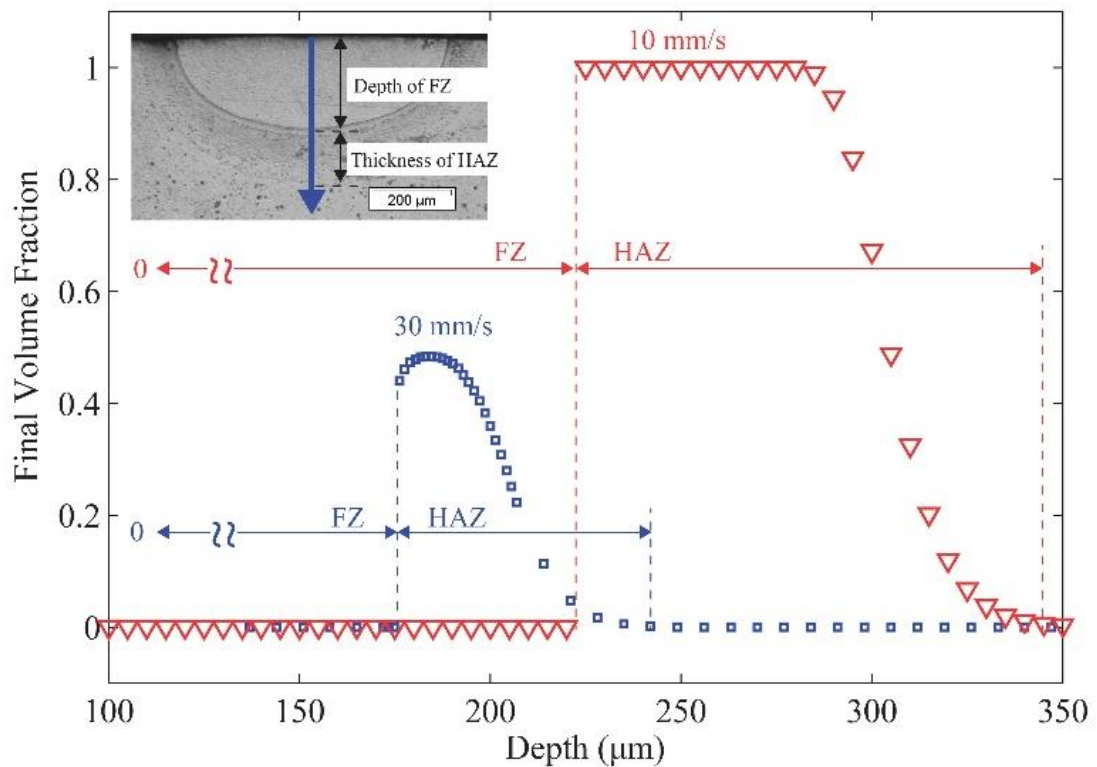


Figure. 6. Calculated final volume fraction of crystalline as a function of depth at different laser scan speeds.

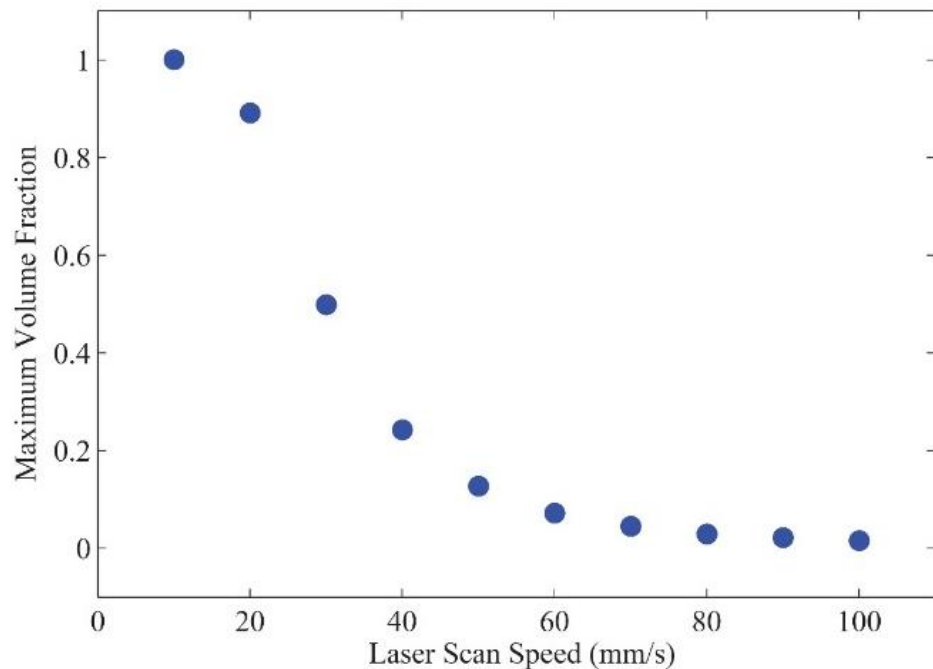


Figure 7. Calculated maximum crystalline VF at different laser scan speeds.

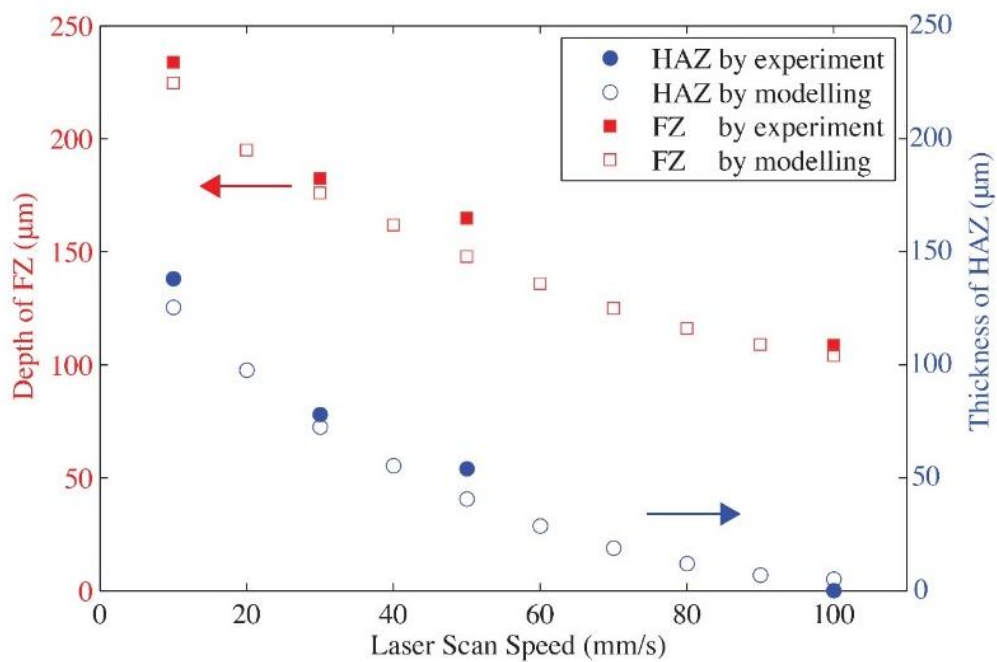


Figure 8. Calculated and measured depth of fusion zone (FZ) and thickness of heat-affected zone (HAZ) as a function of laser scan speed at a fixed laser power $P = 100$ W.

The depth of FZ and the thickness of HAZ as a function of laser scan speeds from experiments and modeling are summarized in Fig. 8. During calculation, the laser power was 100 W. The scan speed v increased from 10 mm/s to 100 mm/s with an increment of 10 mm/s. The depth of FZ in the modeling was counted from the top surface downward to the depth at where $T = 1085$ K, the melting temperature. The thickness of HAZ was counted from the bottom of FZ to the location where final crystalline VF went below 2% (see the inset of Fig. 6). The experimental data were measured from the cross-sectional images shown in Fig. 1 and Fig. 2.

It can be seen from Fig. 8 that for relatively slow scan speeds (10 mm/s and 20 mm/s), the HAZ is thicker than 100 μm . At the scan speed of 50 mm/s, the thickness of HAZ is about 50 μm . Further increases of laser scan speed lowers the HAZ thickness to almost 0 at 90 or 100 mm/s. Similarly, the depth of FZ also decreases as the laser scan speed increases, as expected. The depth of FZ at $P = 100$ W and $v = 100$ mm/s is 105 μm , which is close to the experimental result, 110 μm , shown in Fig. 2(c). Since at this speed, no crystallized HAZ is observed, it is not necessary to further increase the scan speed because it only decrease the size of FZ.

5. CONCLUSIONS

In this paper, the evolution of the crystalline phase in HAZ during laser processing of MG is studied. Using a model which coupled the heat transfer with the classical nucleation theory, the crystallization behavior during laser processing of MG is analyzed. Based on the aforementioned discussion, we can draw the following conclusions:

1) In laser processing of MG, the major challenge is to suppress the crystallization in HAZ. Generally, the size of crystallized HAZ can be reduced/eliminated by increasing the laser scan speed for a given laser power.

2) In HAZ, three distinct crystallized regions were observed. The phenomena were well explained by the induced different degrees of crystallization due to experiencing different temperature histories in each region.

3) The coupled heat transfer model and classical nucleation/growth theory was used to predict the thermal history and volume fraction of crystalline phase in the MG during laser processing. The crystallization behavior in FZ and HAZ can be well described by the classical nucleation theory. The predicted depths of FZ and thicknesses of HAZ at various laser scan speeds compared favorably with experimental results.

ACKNOWLEDGEMENTS

The authors would like to acknowledge the financial support by the Department of Energy (Grant Number: DE-FE0012272) and the UM Fast Track Funding Program.

REFERENCES

- [1] W.L. Johnson, Bulk metallic glasses – a new engineering material, *Current Opinion in Solid State and Materials Science* 1 (3) (1996) 383-386. DOI [http://dx.doi.org/10.1016/S1359-0286\(96\)80029-5](http://dx.doi.org/10.1016/S1359-0286(96)80029-5).
- [2] E.S. Park, D.H. Kim, Design of bulk metallic glasses with high glass forming ability and enhancement of plasticity in metallic glass matrix composites: A review, *Metals and Materials International* 11 (1) (2005) 19-27. DOI <http://dx.doi.org/10.1007/BF03027480>.
- [3] W.L. Johnson, Bulk amorphous metal – An emerging engineering material, *The Journal of The Minerals, Metals & Materials Society* 54 (3) (2002) 40-43. DOI <http://dx.doi.org/10.1007/BF02822619>.
- [4] W.H. Wang, C. Dong, C.H. Shek, Bulk metallic glasses, *Materials Science and Engineering: R: Reports* 44 (2-3) (2004) 45-89. DOI <http://dx.doi.org/10.1016/j.mser.2004.03.001>.
- [5] J. Schroers, Processing of bulk metallic glass, *Advanced Materials* 22 (14) (2010) 1566-1597. DOI <http://dx.doi.org/10.1002/adma.200902776>.
- [6] W.L. Johnson, Bulk glass-forming metallic alloys: Science and technology, *MRS Bulletin* 24 (10) (1999) 42-56. DOI <http://dx.doi.org/10.1557/S0883769400053252>.
- [7] A. Inoue, Stabilization of metallic supercooled liquid and bulk amorphous alloys, *Acta Materialia* 48 (1) (2000) 279-306. DOI [http://dx.doi.org/10.1016/S1359-6454\(99\)00300-6](http://dx.doi.org/10.1016/S1359-6454(99)00300-6).
- [8] D.D. Gu, W. Meiners, K. Wissenbach, R. Poprawe, Laser additive manufacturing of metallic components: materials, processes and mechanisms, *International Materials Reviews* 57 (3) (2012) 133-164. DOI <http://dx.doi.org/10.1179/1743280411Y.0000000014>.
- [9] H. Sun, Microstructure evolution of bulk metallic glasses via laser processing Doctoral dissertation, The Ohio State University (2010). https://etd.ohiolink.edu/pg_10?0::NO:10:P10_ACCESSION_NUM:osu1287025216.
- [10] Y.Y. Zhang, X. Lin., L.L. Wang, L. Wei, F.G. Liu, W.D. Huang, Microstructural analysis of $Zr_{55}Cu_{30}Al_{10}Ni_5$ bulk metallic glasses by laser surface remelting and laser solid forming, *Intermetallics* 66 (2015) 22-30. DOI <http://dx.doi.org/10.1016/j.intermet.2015.06.007>.

- [11] H. Vora, S. Mridha, S. Katakam, H. Arora, S. Mukherjee, N. Dahotre, Thermodynamics and kinetics of laser induced transformation in zirconium based bulk metallic glass, *Journal of Non-Crystalline Solids* 432 (2016) 237-245. DOI <https://doi.org/10.1016/j.jnoncrysol.2015.10.013>.
- [12] Y. Lu, H. Zhang, H. Li, H. Xu, G. Huang, Z. Qin, X. Lu, Crystallization prediction on laser three-dimensional printing of Zr-based bulk metallic glass, *Journal of Non-Crystalline Solids* 461 (2017) 12-17. DOI <https://doi.org/10.1016/j.jnoncrysol.2017.01.038>.
- [13] B. Li, Z.Y. Li, J.G. Xiong, L. Xing, D. Wang, Y. Li, Laser welding of $Zr_{45}Cu_{48}Al_{17}$ bulk glassy alloy, *Journal of Alloys and Compounds* 413 (1-2) (2006) 118-121. DOI <http://dx.doi.org/10.1016/j.jallcom.2005.07.005>.
- [14] H.K. Kim, C. Lee, D.M. Lee, J.H. Sun, S.Y. Shin, J.C. Bae, Pulsed Nd:YAG laser welding of $Cu_{54}Ni_6Zr_{22}Ti_{18}$ bulk metallic glass, *Materials Science and Engineering: A* 449-451 (2007) 872-875. DOI <http://dx.doi.org/10.1016/j.msea.2006.02.323>.
- [15] G. Wang, Y.J. Huang, M. Shagiev, J. Shen, Laser welding of $Ti_{40}Zr_{25}Ni_3Cu_{12}Be_{20}$ bulk metallic glass, *Materials Science and Engineering: A* 541 (2012) 33-37. DOI <http://dx.doi.org/10.1016/j.msea.2012.01.114>.
- [16] F. Jiang, Z.B. Zhang, L. He, J. Sun, H. Zhang, Z.F. Zhang, The effect of primary crystallizing phases on mechanical properties of $Cu_{46}Zr_{47}Al_7$ bulk metallic glass composites, *Journal of Materials Research* 21 (10) (2006) 2638-2645. DOI <http://dx.doi.org/10.1557/jmr.2006.0315>.
- [17] S.C. Glade, R. Busch, D.S. Lee, W.L. Johnson, R.K. Wunderlich, H.J. Fecht, Thermodynamics of $Cu_{47}Ti_{34}Zr_{11}Ni_8$, $Zr_{52.5}Cu_{17.9}Ni_{14.6}Al_{10}Ti_5$ and $Zr_{57}Cu_{15.4}Ni_{12.6}Al_{10}Nb_5$ bulk metallic glass forming alloys, *Journal of Applied Physics* 87 (10) (2000) 7242-7248. DOI <http://dx.doi.org/10.1063/1.372975>.
- [18] J. Schroers, R. Busch, A. Masuhr, W.L. Johnson, Continuous refinement of the microstructure during crystallization of supercooled $Zr_{41}Ti_{14}Cu_{12}Ni_{10}Be_{23}$ melts, *Applied Physics Letters* 74 (19) (1999) 2806-2808. DOI <http://dx.doi.org/10.1063/1.124020>.
- [19] E. Pekarskaya, J.F. Löffler, W.L. Johnson, Microstructural studies of crystallization of a Zr-based bulk metallic glass, *Acta Materialia* 51 (14) (2003) 4045-4057. DOI [http://dx.doi.org/10.1016/S1359-6454\(03\)00225-8](http://dx.doi.org/10.1016/S1359-6454(03)00225-8).
- [20] L. Zhang, S. Pauly, M.Q. Tang, J. Eckert, H.F. Zhang, Two-phase quasi-equilibrium in β -type Ti-based bulk metallic glass composites, *Scientific Reports*, 6 (2016) 19235. DOI <http://dx.doi.org/10.1038/srep19235>.

- [21] R.B. Dandliker, R.D. Conner, W.L. Johnson, Melt infiltration casting of bulk metallic-glass matrix composites, *Journal of Materials Research* 13 (10) (1998) 2896–290. DOI <https://doi.org/10.1557/JMR.1998.0396>.
- [22] Y. Wu, H. Wang, Z.Y. Zhang, X.D. Hui, G.L. Chen, D. Ma, X.L. Wang, Z.P. Lu, Formation of Cu–Zr–Al bulk metallic glass composites with improved tensile properties, *Acta Materialia* 59 (8) 2011 2928-2936. DOI <http://dx.doi.org/10.1016/j.actamat.2011.01.029>.
- [23] ASTM E1181-02(2015) Standard Test Methods for Characterizing Duplex Grain Sizes, ASTM International, West Conshohocken, PA, 2015. DOI <https://doi.org/10.1520/E1181-02R15>.
- [24] Y. Shen, Y. Li, C. Chen, H.L. Tsai, 3D printing of large, complex metallic glass structures, accepted for publication in *Materials and Design*.
- [25] W. Kurz, D.J. Fisher, *Fundamentals of solidification*, Trans Tech Publications 1st edition (1986) Rockport MA USA. ISBN: 0-87849-522-3
- [26] J. Schroers, W.L. Johnson, History dependent crystallization of $Zr_{41}Ti_{14}Cu_{12}Ni_{10}Be_{23}$ melts, *Journal of Applied Physics* 88 (1) (2000) 44-48. DOI <http://dx.doi.org/10.1063/1.373621>.
- [27] Z. Evenson, T. Schmitt, M. Nicola, I. Gallino, R. Busch, High temperature melt viscosity and fragile to strong transition in Zr–Cu–Ni–Al–Nb(Ti) and $Cu_{47}Ti_{34}Zr_{11}Ni_8$ bulk metallic glasses, *Acta Materialia* 60 (12) (2012) 4712-4719. DOI <http://dx.doi.org/10.1016/j.actamat.2012.05.019>.
- [28] A. Masuhr, T.A. Waniuk, R. Busch, W.L. Johnson, Time Scales for Viscous Flow, Atomic Transport, and Crystallization in the Liquid and Supercooled Liquid States of $Zr_{41.2}Ti_{13.8}Cu_{12.5}Ni_{10.0}Be_{22.5}$, *Physics Review Letter* 82 (1999) 2290-2293. DOI <https://doi.org/10.1103/PhysRevLett.82.2290>.
- [29] A.T. Patel, H.R. Shevde, A. Pratap, Thermodynamics of $Zr_{52.5}Cu_{17.9}Ni_{14.6}Al_{10}Ti_5$ bulk metallic glass forming alloy, *Journal of Thermal Analysis and Calorimetry*, 107 (1) (2011) 167-170. DOI <http://dx.doi.org/10.1007/s10973-011-1591-9>.
- [30] S. Mukherjee, Z. Zhou, J. Schroers, W.L. Johnson, W.K. Rhim, Overheating threshold and its effect on time–temperature–transformation diagrams of zirconium based bulk metallic glasses, *Applied Physics Letters* 84 (24) (2004) 5010-5012. DOI <http://dx.doi.org/10.1063/1.1763219>.

- [31] J. Schroers, A. Masuhr, W.L. Johnson, R. Busch, Pronounced asymmetry in the crystallization behavior during constant heating and cooling of a bulk metallic glass-forming liquid, *Physical Review B* 60 (17) (1999) 11855. DOI <http://dx.doi.org/10.1103/PhysRevB.60.11855>.
- [32] H. Kim, L. Mandelkern, Temperature dependence of the bulk crystallization rate of polymers, *Journal of Polymer Science Part B: Polymer Physics* 6 (4) (1968) 695-706. DOI <http://dx.doi.org/10.1002/pol.1968.160060405>.
- [33] G. Kaltenboeck, T. Harris, K. Sun, T. Tran, G. Chang, J.P. Schramm, M.D. Demetriou, W.L. Johnson, Accessing thermoplastic processing windows in metallic glasses using rapid capacitive discharge, *Scientific Reports* 4 (2014) 6441. DOI <http://dx.doi.org/10.1038/srep06441>.

III. THE EFFECT OF PRE-EXISTING NUCLEUS DENSITY ON CRYSTALLIZATION BEHAVIOR DURING LASER PROCESSING OF ZR-BASED METALLIC GLASS AND THE CORRESPONDING QUALITY FACTOR

Yiyu Shen, Yingqi Li, and Hai-Lung Tsai

Department of Mechanical and Aerospace Engineering

Missouri University of Science and Technology, Rolla, Missouri 65409, U.S.A

ABSTRACT

The effect of pre-existing nucleus density on the crystallization behavior of Zr-based BMG was investigated. An experiment was designed to demonstrate the different crystallization tendency a Zr-based BMG alloy with different nucleus densities. By using the classical nucleation theory, we discovered that a small amount of pre-existing nucleus density in a BMG can change the time-temperature-transformation (TTT) curve from a well-known 'C shape' to a 'ε shape.' This was consistent with the reported experimental results and provides fundamental understanding on why the shape of a TTT curve for heating process is different from that for cooling process. Based on the classical nucleation theory, two quality factors were proposed that can quantify the effect of pre-existing nucleus density. By integrating the heat transfer model with the classical nucleation theory, the crystalline phase evolution during laser welding was discussed, and the modeling predictions compared favorably with the experimental results.

Keywords: Metallic glass, Crystallization, Nucleation and growth, Laser processing

1. INTRODUCTION

Bulk metallic glasses (BMGs), also called amorphous alloys, have gained much research interest since their discovery in the 1960s. In the past a few years, several reviews have been published for this class of material. Löffler, (2003) discussed the history of BMG and their thermophysical/mechanical properties. Johnson (1999) and Park (2005), respectively, introduced the general principles of designing high performance BMG alloy. The review by Telfore (2004) discussed the potential application of BMG in the near future. It was highlighted that the limited size has delay the application of BMG for engineering applications. Due to the requirement of high cooling rate, BMGs are produced in the shapes of foil, plate, or rod with certain theoretical maximum section-thickness ranging from a few microns to a few centimeters. The production of BMGs is normally accomplished by casting methods such as the counter-gravity casting, die casting and injection molding. In order to obtain a thick BMG, laser welding may provide a possible solution. Furthermore, by using the laser-foil-printing additive manufacturing technology (Shen et al., 2017), metallic glass foils can be laser welded, layer-by-layer, to become 3D, large metallic glass structures with complex geometry. To study the welding of BMG, one needs to first understand the crystallization behavior of BMGs, which has been studied extensively in the past decades (Tkatch et al., 1997). Many criteria were proposed in order to evaluate the glass forming ability (GFA) of a given MG system. Example criteria include the critical thickness (Johnson, 1999), the critical cooling rate R_c (Wang et al., 2004), the reduced glass transition temperature T_{rg} ($= T_g/T_x$) (Inoue, 2000) in which T_g is the glass transition temperature and T_x is the crystallization temperature, the supercooled liquid region ΔT_{xg} ($= T_g - T_x$) Löffler, (2003), the γ value ($= T_x/(T_g + T_l)$) (Lu et al., 2000) in which T_l is the

liquidus temperature, $(T/T_g)^{2/3}$ (Johnson and Samwer, 2005) and the average elastic shear limit criterion (Lu and Liu, 2002). However, for laser processing (welding, cutting or surface modification), the above criteria failed. For example, in the reported work on laser processing of BMGs, crystallization was observed, particularly in the heat-affected zone (HAZ), even if the cooling rate was two orders of magnitude larger than the reported critical cooling rate (Williams and Lavery, 2017).

The reason of this deviation is that in all the proposed criteria, solidification process is assumed to start from liquid phase in a perfect amorphous condition. Here, the term perfect amorphous stands for the status with zero nucleus or zero VF of crystalline phase. This is certainly true for most casting technologies in which BMGs are cooled down from liquid phase such like presented by Schroers (1999). However, in laser processing of cast BMG foils/plates, the BMGs begin with solid phase and then experience melting and re-solidification. During the casting process, since solidification of liquid amorphous is not an instant but starting from the surface and progressively toward the inside of the BMG, there must a finite amount of nuclei in the BMG. In other words, it is extremely difficult, if not impossible, to cast a BMG part with free nuclei, particularly at locations away from the surface. This amount of nuclei acts as the pre-existing nuclei in the subsequent laser processing of the cast BMGs. So far, there is no direct evidence that the existing nuclei will decompose back to their amorphous phase without melting (Schroers, 2010). According to the classical nucleation theory, both the pre-existing nuclei and the quenched-in nuclei contribute to the crystallization. Here, the term quenched-in nuclei stands for the nuclei that are generated during solidification for a process such as the laser welding process. Thus, if BMG foils/plates are assumed to be perfect amorphous before laser welding, the

contribution from pre-existing nuclei would be ignored, leading to an expected inaccuracy in determining the crystallization behavior.

There is yet no universal technique developed to quantify the degree of crystallization for a BMG, particularly when the VF of crystalline phase is low, say $< 2\%$. The common methods for testing crystallization of a BMG include X-ray diffraction (XRD), differential scanning calorimetry (DSC), and transmission electron microscope (TEM). These methods can give qualitative information about the existence of amorphous phase, but not quantitatively the percentage of amorphous phase or crystalline phase. The detection limit of an XRD is around 2% of crystalline phase, while the DCS test is good in analyzing the thermodynamic behavior of the BMG, but not for quantitatively estimate the percentage of amorphous phase. TEM has the ability of acutely capturing the nuclei core within the sample. However, due to a small sampling volume (typically $500 \times 500 \times 50 \text{ nm}^3$ or below), TEM is not a suitable tool when nucleus density is not very high or uniform in the sample.

In this paper we first setup a laser processing experiment on a Zr- based BMG plate to demonstrate the effect of pre-existing nuclei on the crystallization behavior. Based on the classical nucleation theory (CNT), a time-temperature-transformation (TTT) diagram is drawn to show the differences between a perfect BMG and an imperfect BMG with different levels of pre-existing nuclei. Then, two ‘quality factors’ are proposed to indicate the quantity of pre-existing nuclei within a metallic glass solid. The physical meaning behind the pre-existing nucleus density, the related quality factors as well as methods to determine their values are further discussed.

2. EXPERIMENTAL

A cast Zr-based BMG plate, LM105 (PS30, $Zr_{52.5}Ti_5Al_{10}Ni_{14}Cu_{17.9}$, at.%, by Liquidmetal Technologies, Inc.) with 2.5 mm thickness was used in this study. The as-cast BMG plate was prepared by the counter-gravity casting method with copper mold. The alloy was machined to blocks, each has dimensions of 10 mm in length and width (denoted as Sample in later discussion). The machined samples were laser welded (bead-on-plate) by a CW laser (YLR-1000, IPG Inc.) with a wavelength of 1070 μm . The laser beam diameter D on the focal plane at the surface of the BMG plate was about 430 μm . The motion of the laser beam was controlled by a scanner (hurrySCAN III, SCANLAB Inc.) with a maximum scan speed of 2000 mm/s at the focal plane. All experiments were conducted in an argon chamber in order to avoid possible oxidization during laser welding.

Two samples, Sample 1 and Sample 2, were tested in this experiment. Sample 1 was the original as-cast BMG. Sample 2, however, was obtained by sealing and annealing of an as-cast BMG plate by DSC (TA Instruments DSC 2010) via the following procedure: heating up from room temperature to 680 K at 20 K/min, keeping steady for 30 min at 680 K, and then cooling down to room temperature. The objective of annealing Sample 2 at a low temperature is to generate additional nuclei but still at a low VF of crystalline phase. Note both Sample 1 and Sample 2 contain a certain amount of nuclei inherited from casting, but Sample 2 contains additional nuclei due to annealing. Also, the nucleus density should be a distribution in the BMG, but in this study it is assumed constant. Both samples' surfaces were polished with 800-grit SiC paper right before laser processing. For each sample, a laser beam is scanned over its top surface along the same path at the center multiple times with constant preselected processing parameters: laser output power $P =$

100 W and laser scan speed $v = 100$ mm/s. The setup can be seen in Fig. 1 (a). An interval time of 30 s was applied between any two laser scans in order to avoid possible heat accumulation. Also, a thermocouple was attached to the sample to ensure the temperature of the sample drops back to room temperature before next laser scan. After the experiment, the samples were cross-sectioned, polished, etched by a solution of 100 ml H₂O, 2 ml H₂O, and 0.1 ml HF, and then examined by optical microscope (OM) and scanning electron microscope (SEM, Helios S600).

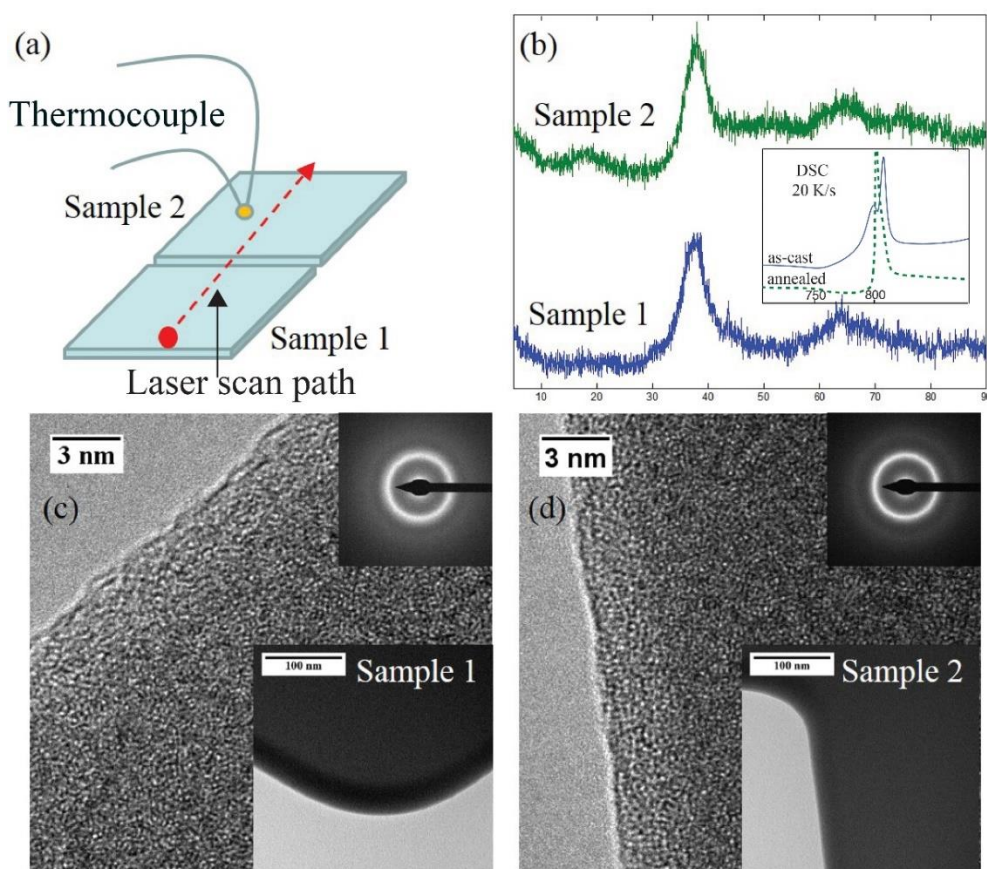


Figure 1. (a) Experimental setup, (b) XRD test results for Sample 1 & 2, and (c) and (d) TEM images for Sample 1 and Sample 2 before the experiment.

The XRD (Panalytical X'pert Pro, with Cu K α wavelength driven at 45 kV and 40 mA) was applied on both the original and annealed sample surfaces before laser welding, as given in Fig. 1 (b). It can be seen that for both the original and annealed samples, the diffraction patterns show only a clear shallow halo which implies that within the detection limit of XRD, two samples are not distinguishable. Note, when the BMG contains a high VF of crystalline phase, the XRD curve shows several spikes indicating that the crystallization has occurred (Wang et al., 2004), and the VF of crystalline phase can be estimated from the OM image of the etched cross section surface with imaging method (such like ImageJ software (Zhang et al., 2016)). This study focuses on the condition that the VF of crystalline phase is very low which even cannot be detected by XRD. The DSC curves in the inset of Fig. 1 (b) have shown a clear difference between the two samples which, however, cannot estimate the difference of the percentage of amorphous phase between the two tested samples. The TEM (Tecnai F20) images are given in Fig. 1 (c) and (d) for Sample 1 and Sample 2, respectively. It is seen that no nano-nuclei core is observed for either sample. The high-resolution images of the two samples also show the randomly distributed atoms without any long-range order. The TEM results lead to the conclusion that Sample 1 and Sample 2 are indistinguishable. The results shown in Fig. 1 are consistent with our previous discussion that all existing technologies cannot tell the degree of crystallization and the difference between two BMGs which are in a low degree of crystallization.

3. EXPERIMENTS AND DISCUSSION

Figure 2 presents the OM images at the cross section perpendicular to the laser scan path. The OM images indicate that both Sample 1 and Sample 2 are free of crystalline phase before laser processing (at the resolution of OM images). In all cases, crystallization was only observed in the heat-affected zone (HAZ), while all fusion zones (FZ) were free of crystalline phase. In Sample 1, no crystalline phase was observed in HAZ at the laser scan number equals to or less than 7. At the scan number equals to 10, a very thin crystallized HAZ can be observed (though still hardly noticeable). At the scan number equals to 13, the crystalline band became obvious. The crystallized HAZ was thicker at the center of the FZ compared to those at the side. The crystallized HAZ expanded with the increase of scan number before the scan number reached 19. Then, the crystallized HAZ did not change much at higher scan numbers. To compare, the crystallized HAZ in Sample 2 became visible after the 4th laser scan as shown in Fig. 2(b). The size of crystallized HAZ remained almost constant after around the 10th scan.

The crystallization behaviors presented in Fig. 2 have shown a clear difference between Sample 1 and Sample 2, although all the used laser parameters were identical for both samples. The XRD and TEM results given in Fig. 1 have also shown that the two samples are fully amorphous and indistinguishable in degree of crystallization before laser processing. If simply considered from the viewpoint of thermal history, the two samples experienced the same heating/cooling thermal history, thus they should have led to an expecting same progression of crystallization. The only difference was that Sample 2 was annealed before the experiment.

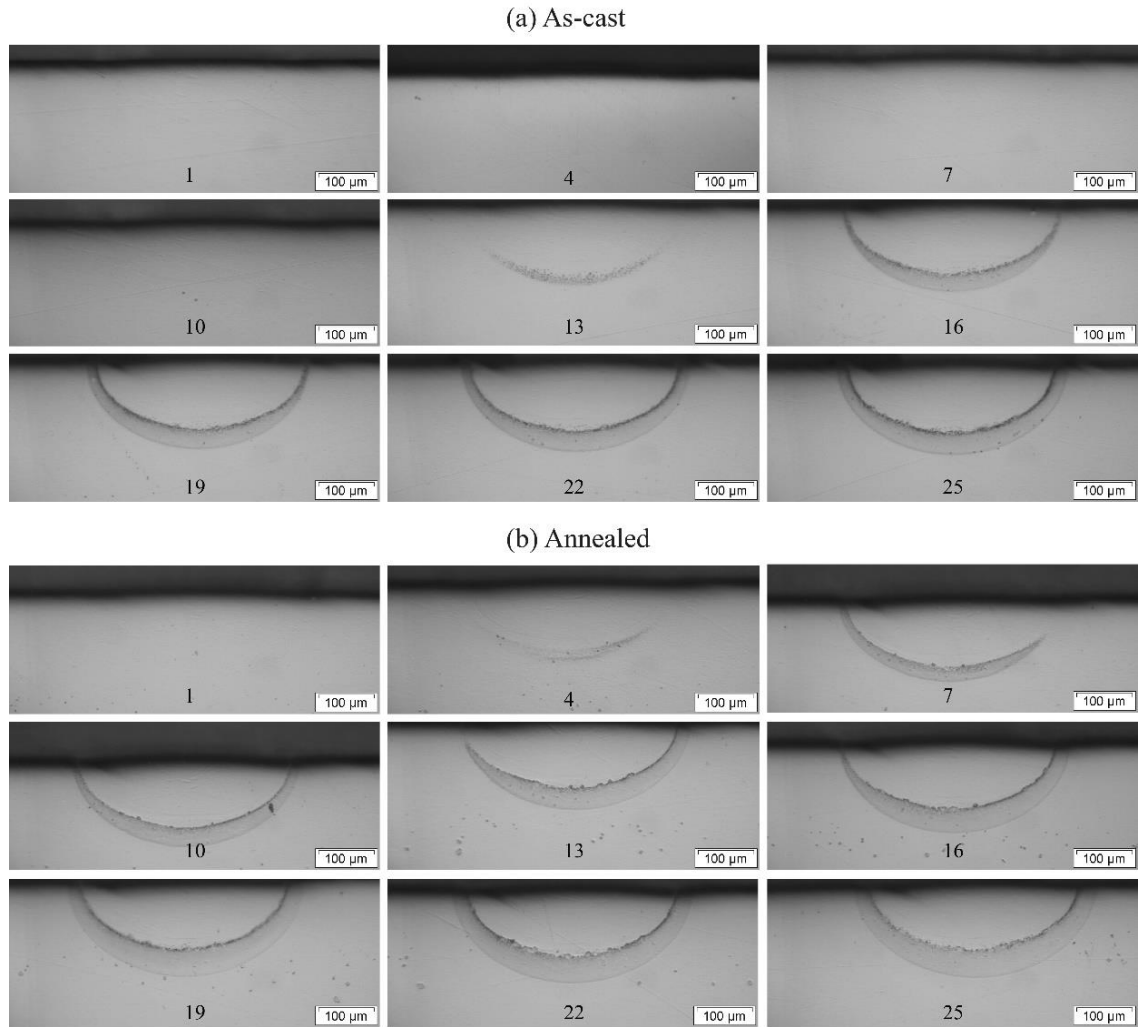


Figure 2. OM images of cross-sectional view of laser scanned a) Sample 1 and b) Sample 2.

In the free volume theory (Li et al., 2007), the difference between the two samples can be described by the variation of free volume due to annealing or so called “relaxation.” However, the density of free volume is difficult to determine (Schroers, 2010). Since the scope of this work is to focus on the crystallization process, we consider the difference between Sample 1 and Sample 2 using the classical nucleation theory (CNT). From CNT,

the difference between the two samples is the generated nucleus density in Sample 2 during the annealing process. Because the generated nuclei don't have a chance to grow significantly at low annealing temperature, the overall VF of crystalline phase is still low. As a result, the XRD result is not able to tell the difference between the two samples. The nucleus density generated by annealing in Sample 2 is predicted to be about 2×10^5 $1/\text{mm}^3$ (see later discussion), which is equivalent to 2×10^{-4} $1/\mu\text{m}^3$. Considering the typical size of TEM, $150 \times 150 \times 10$ nm^3 , under the given nucleus density, the possibility that a TEM image to include a single nucleus core is around 4.5×10^{-6} percent. Therefore, it is not surprised that the TEM images are not able to distinguish the two samples.

The aforementioned discussion on the difference of crystallization behavior naturally leads to the conclusion that the “quality” of the two samples is different. More specifically, the ability of the two samples retaining in amorphous phase against further heating/cooling is different. Quantifying this ability of BMG is valuable and important for laser welding of BMGs.

4. NUCLEATION KINETICS

For the crystallization process during laser welding, it is assumed that the crystallization behavior of a given MG obeys the CNT. In CNT, the nucleation is driven by two processes, the generation of nucleus cores (rate of crystal nucleation, I) and the growth of nuclei (rate of crystal growth, U). The following assumptions are made for the nucleation kinetics:

1. The crystallization process follows and only follows the CNT; no any other mechanism, such as decomposition of nuclei, is taken into consideration.
2. Temperature-dependent crystallization behavior of MG is considered, while higher-orders (temperature-gradient related) are not (Schroers et al., 1999; Schroers and Johnson, 2000).
3. Nuclei and crystal phases in the metallic glass system transferred back to amorphous liquid at, and only at, temperatures above melting temperature, $T > T_m$.

Based on the above assumptions, the temperature-dependent nucleation rate $I(T)$ can be written as (Tkatch et al., 1997):

$$I(T) = A \cdot D(T) \cdot \exp\left(-\frac{\Delta G^*}{kT}\right) \quad (1)$$

where $I(T)$ is the temperature-dependent nucleation rate, A is a constant, $D(T)$ is the effective diffusivity, k is the Boltzmann's constant, T denotes the absolute temperature, and ΔG^* is the thermodynamic potential barrier of nucleation. ΔG^* has the following relation:

$$\Delta G^* = \frac{16\pi\sigma^3}{3\Delta G^2} \quad (2)$$

where σ denotes the interface energy between nucleus and melt and ΔG is the difference of Gibbs free energy between the solid and liquid (amorphous) phase. Since the fluid flow

is ignored, only the diffusion-limited crystalline growth is considered. The temperature-dependent crystalline growth velocity $U(T)$ can be expressed by the following (Sun, 2010):

$$U(T) = \frac{D(T)}{a} \left[1 - \exp\left(-\frac{\Delta G}{kT}\right) \right] \quad (3)$$

where a is the average interatomic spacing. The aforementioned equations, Eqs. (1) through (3), were numerically solved with the LM105 parameters given below. The temperature-dependent effective diffusivity D was calculated from measured viscosity (Evenson et al., 2012) by a Stokes-Einstein relation based hybrid function introduced by Schroers and Johnson (2000). The Gibbs free energy difference between undercooled liquid and corresponding crystal solid, ΔG , as a function of temperature reported by Patel et al. (2011) was used. The average interatomic spacing a of 2.6×10^{-7} mm was used, calculated from the weighted atomic percentage of LM105 alloy. The numerical value of σ was estimated as of 0.076 J/m^2 by the nose temperature of experimentally measured TTT curve reported by Mukherjee et al. (2004). Finally according the crystallization time at the nose temperature (Mukherjee et al., 2004), the constant A was estimated as 2.5×10^{33} .

Considering the diffusion limited crystal growth only, the three-dimensional time and temperature dependent VF of the crystallized phase of an initially perfect amorphous alloy, $X_p(T, t)$, is (Tkatch et al., 1997):

$$X_p(T, t) = 1 - \exp\left\{-\frac{4\pi}{3} \cdot \left[\int_0^t I(T, \tau) \left[\int_\tau^t U(T, t') dt' \right]^3 d\tau \right]\right\} \quad (4)$$

By expanding the exponential function in Eq. (4) and if the value of the exponent in the exponential function is small as compared with unit (which also implies the VF of crystalline phase is small), Eq. (4) can be further simplified to the following equation (Tkatch et al., 1997):

$$X_p(T, t) = \frac{4\pi}{3} \cdot \left[\int_0^t I(T, \tau) \left[\int_\tau^t U(T, t') dt' \right]^3 d\tau \right] \quad (5)$$

If temperature is constant (an isothermal process), both I and U are constant, and Eq. (5) can be integrated w.r.t. time and simplified as (Uhlmann, 1972):

$$X_p = \frac{\pi}{3} \cdot I \cdot U^3 \cdot t^4 = \frac{\pi}{3} \cdot U^3 \cdot t^3 \cdot (I \cdot t) \quad (6)$$

For an imperfect amorphous alloy, however, also consider only the diffusion limited crystal growth, a pre-existing nucleus density N is added to Eq. (4) leading to the following equation (Tkatch et al., 1997):

$$X_a(T, t) = 1 - \exp \left\{ -\frac{4\pi}{3} \cdot \left[\int_0^t I(T, \tau) \left[\int_\tau^t U(T, t') dt' \right]^3 d\tau + N \cdot \left[\int_0^t U(T, t'') dt'' \right]^3 \right] \right\} \quad (7)$$

where X_a denotes the VF of crystalline phase in an imperfect amorphous. With a small X_a , Eq. (7) can be simplified as:

$$X_a(T, t) = \frac{4\pi}{3} \cdot \left[\int_0^t I(T, \tau) \left[\int_\tau^t U(T, t') dt' \right]^3 d\tau + N \cdot \left[\int_0^t U(T, t'') dt'' \right]^3 \right] \quad (8)$$

Equation (8) can also be simplified to the following equation if both I and U are assumed constant for an isothermal process:

$$X_a(t) = \frac{\pi}{3} \cdot U^3 \cdot t^3 \cdot (I \cdot t + 4N) \quad (9)$$

The pre-existing nucleus density N for a BMG during its casting process can be estimated by integrating the nucleation rate with respect to time via the following equation:

$$N(t) = \int_0^t I(T, t) dt \quad (10)$$

Note the reported critical cooling rate for a BMG was usually obtained for a very small sample in the laboratory, such like the work done by Pogatscher et al. (2014). For a

large BMG part, such as the one used in this experiment, which was obtained by a casting process, the cooling rate is a function of location in the part and time. For a given location in the BMG, if its thermal history (i.e., the temperature as a function of time) is known, then Eq. (10) can be used to calculate the nucleus density N at that specific location. Unfortunately, the thermal history of a large BMG in an actual casting process is normally unavailable; instead an approximate “averaged” cooling rate is reported. The liquid amorphous LM105 starts to solidify at the melting temperature $T_m = 1085$ K and the time is counted as zero at this instant. If an “averaged” constant cooling rate for a casting process is available, for example 100 K/s, and if it is assumed that the cooling starts from T_m until 485 K in 6 s, then N can be calculated in Eq. (10). Hence, cooling rates discussed in this study can be for a very small sample at which it truly represents the cooling rate or a large piece of BMG part at which it represents an averaged constant cooling rate. Based on the above discussion, for any given cooling rate, the corresponding pre-existing nucleus density value, N , can be calculated. Note the pre-existing nucleus can not only be generated during the casting process from liquid, but may also be generated by any other following solid-state heat treatment such like annealing. To keep the discussion simple in this paper, we assumed the laser processed BMG samples only experienced the casting process from liquid with constant cooling rate.

If a small VF of crystalline phase is assumed (1% is used in this paper), for any given temperature in an isothermal process (i.e., the temperature is held constant), the required crystallization time, t , can be calculated by Eq. (6) for a perfect amorphous, and by Eq. (9) for an imperfect amorphous with N pre-existing nucleus density. Thus, with an increment of 1 K, for each temperature the corresponding crystallization time can be

calculated and a complete TTT diagram can be obtained. Note here the selection of 1% as the critical VF of crystalline phase for drawing the TTT diagram may be controversial. To experimentally measuring the TTT diagram, people use either onset of crystallization or peak of crystallization to draw the point as discussed by Pogatscher et al. (2014). While what really matters is the detection limit of the equipment used in those measurements, which varies case by case. In the theory presented in this paper, the critical VF of crystalline phase can be linked to the detection limit of the equipment used in experiment. Choosing to use the value of 1% is just showing a simple example for the process of obtaining TTT curve from Eq. (6) and Eq. (9).

5. RESULTS AND DISCUSSION

How the pre-existing nucleus density affecting the crystallization process of a BMG is of ultimate interest. Taken LM105 alloy as an example, the calculated TTT curves with and without pre-existing nucleus density are plotted in Fig. 3. The temperature dependent I and U obtained from Eq. (1) and (3), are shown in the inset of Fig. (3) (detailed discussion can be found in our previous reported work: Shen et al, 2017). In Fig. (3), the dashed TTT curve is for the LM105 alloy without pre-existing nuclei, in another world an ideal perfect amorphous. As expected, it is a well-known C-shaped TTT curve. The nose temperature of the perfect amorphous LM105 alloy is 860 K, and the $t_{\text{nose-p}}$ is 0.78 s. It is seen in the inset of Fig. (3), at low temperatures (e.g., $T < 600$ K), both I and U are very low and, hence, it takes a long crystallization time to reach 1% of crystalline phase. As temperature increases, the nucleation rate, I , increases to its maximum at about 780 K, while the crystal growth rate, U , starts to increase significantly at about 800 K. As a result, the crystallization time decreases as the temperature increases. Although U increases significantly after 900 K, I decreases rapidly after 880 K, which results in the great increase of crystallization time thereafter.

Similarly, the TTT curves with different pre-existing nucleus densities can be determined and plotted as solid curves shown in Fig. 3. For a given pre-existing nucleus density, $N = 10^{-3} \text{ 1/mm}^3$, the TTT curve overlaps the dashed curve at temperatures below around 934 K. For the upper part of the curve at temperatures above 934 K, the TTT curve “peels off” from the “C” shape and yields to the left-hand side, reaching to another nose at the temperature of 1030 K, resulting in an overall “ε” shaped TTT curve.

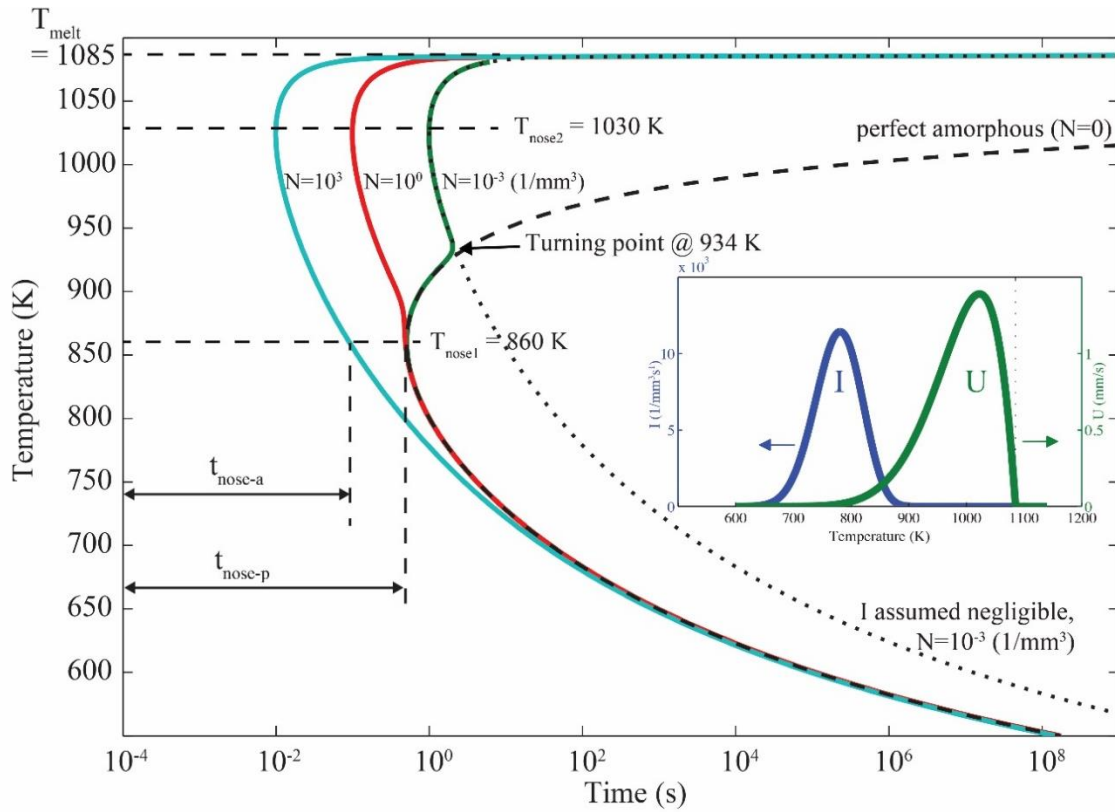


Figure 3. The calculated TTT curves of a “perfect” amorphous and “imperfect” amorphous LM105 with different pre-existing nucleus densities.

A case when $N = 10^{-3} \text{ 1/mm}^3$ and the I effect is ignored (also see Eq. (9)), a dotted TTT curve was calculated and shown in Fig. (3). Note in this case, only the pre-existing nucleus density is considered while the quenched-in nucleus density is ignored. As seen in Fig. 3, at low temperatures where $T < 934 \text{ K}$, the TTT curve for $N = 10^{-3} \text{ 1/mm}^3$ only, fits the dashed curve well, indicating that the effect of pre-existing nucleus density on crystallization is negligible. On the other hand for high temperatures where $T > 934 \text{ K}$, the TTT curve for $N = 10^{-3} \text{ 1/mm}^3$ fits the dotted curve well, indicating that at these temperatures the effect of quenched-in nucleus can be ignored and the crystallization process is dominated by the pre-existing nuclei. For larger pre-existing nucleus density

values, the overall TTT curves yields toward the left-hand side. All TTT curves are merged at the temperature when the BMG melts, i.e., at $T_m = 1085$ K. A similar TTT diagram was recently experimentally obtained by Pogatscher et al. (2014) on Au based metallic glass. In their results, the TTT curve for cooling process from liquid phase has the same C shape, while for heating process from solid phase, the TTT curve has a ε shape. This is because when the BMG cools from liquid phase, there is no pre-existing nuclei, while heating from solid phase that inevitably contains some amount of nuclei. Hence, the modeling prediction in this study are consistent with their experimental results.

When the pre-existing nucleus density becomes higher, the peering-off happens at lower temperatures. The overall shape of the TTT curve is determined by the competition of the two parts in the term $(I \cdot t + 4N)$. When $4N$ is small and ignorable, Eq. (9) yields back to Eq. (6), which is the equation for a perfect amorphous. At this condition, the TTT curve plotted based on Eq. (9) would be expected to be identical to the C shape. When $I \cdot t$ equals to $4N$, the contribution of pre-existing nuclei and the quenched-in nuclei balanced, the TTT curve starts to change its shape. Note N is constant while I decreases rapidly for temperatures higher than 700 K. When $4N$ is large enough so that the term $I \cdot t$ can be ignored, Eq. (9) yields to the equation below:

$$X_a(t) = \frac{\pi}{3} \cdot U^3 \cdot t^3 \cdot 4N \quad (11)$$

In Eq. (11), when X_a is set to the critical value (1% in this paper), the crystallization time is only determined by U . As shown in the inset of Fig. 3, the maximum value of U appears at 1030 K. This explains why a second nose of the “ ε -shape” curve is located at $T = 1030$ K in Fig. 3.

As calculated in Eq. (10), to obtain a BMG with pre-existing nucleus density $N = 10^{-3} \text{ 1/mm}^3$, the required cooling rate is $5 \times 10^7 \text{ K/s}$ during the casting process, which is considerably impossible to achieve. As a result, the phenomenon of “peering-off” for a cast BMG seems to be unavoidable. Thus, for an actual BMG with certain amounts of pre-existing nuclei, one may always expect to find a deformed TTT curve rather than the original one.

Further discussion is worth drawing on the nucleus density. With higher nucleus density, the TTT curve peered off at lower temperature. It is determined by the competition of the two parts in term $(I \cdot t + 4N)$. The I related term is material itself dependent. While the N related term describes the thermal history of the MG experienced, usually in the casting process. When the two terms are compared, it reminds us that for a given solid BMG part, simply reporting a pre-existing nucleus density number remains as a number it is. What really matters is how it is compare to the nucleation rate of the material itself. For example, given the pre-existing nucleus density of $N = 10^0 \text{ 1/mm}^3$ for the LM105 alloy as shown in Fig. 3, the level of pre-existing nucleus density has almost no effect on the crystallization behavior of the LM105 alloy up to the nose temperature. However, the same value of $N = 10^0 \text{ 1/mm}^3$ can be significant to the alloy system when nucleation rate (I) is much lower, such as the well-known Vit 1 MG alloy ($\text{Zr}_{41}\text{Ti}_{14}\text{Cu}_{12}\text{Ni}_{10}\text{Be}_{23}$, at%) (Matin et al. 2004; Peker and Johnson, 1993).

To quantify the effect of pre-existing nuclei, we propose the definitions of two quality factors, Q_x and Q_t , for any cast BMG. For a BMG in its perfect amorphous, the nose temperature is denoted as $T_{\text{nose-p}}$, and the corresponding crystallization time to a certain percentage VF of crystalline, X_c (e.g., $X_c = 1\%$) is denoted as $t_{\text{nose-p}}$, as shown in Fig. 3. For

an actual BMG with pre-existing nucleus density, the crystallization time to reach the same X_c value at the same $T_{nose,p}$ temperature is denoted as t_{nose-a} , as shown in Fig. 3. The quality factor Q_t is then defined as t_{nose-a} divided by t_{nose-p} .

$$Q_t = \frac{t_{nose-a}}{t_{nose-p}} \quad (12)$$

Here, the subscriptions p and a stand for the “perfect amorphous BMG” and the “imperfect BMG,” respectively.

In a simple word, Q_t is the ratio of the nose time between a perfect BMG and an imperfect BMG. Note the “VF of crystalline phase,” X_c , needs to be selected subjectively. From the experimental point of view, it is reasonable to set it equal to the detection limit of a testing method, $X_c = X_{detection}$. Since the Q_t can be different under different X_c values, the used X_c is also important to report along with Q_t . For example, $Q_t = 0.8 @ X_c = 1\%$.

Alternatively, another quality factor Q_x can be defined in the following. For a selected VF of crystalline phase, for example, $X_p = 1\%$, for a BMG in its perfect amorphous, as discussed above, the nose temperature $T_{nose,p}$, and the corresponding crystallization time t_{nose-p} can be determined. For an actual BMG, the sample is placed under an isothermal condition at $T = T_{nose-p}$ for a period of time $t = t_{nose-p}$, and the resulting VF of crystalline phase is determined as X_a . Then, the quality factor Q_x is defined as X_p divided by X_a . Actually, Q_x can be simply calculated by dividing Eq. (6) by Eq. (9):

$$Q_x = \frac{I_{nose} \cdot t_{nose}}{I_{nose} \cdot t_{nose} + 4N} \quad (13)$$

where I_{nose} is the nucleation at the temperature T_{nose-p} .

The two defined factors, Q_t and Q_x , have some similarities. They are both unitless values and are between 0 and 1. Being closer to 1, means the quality of imperfect MG part is closer to the perfect amorphous. The difference is that Q_t is more straightforward from

experimental point of view. To experimentally measure the Q_t of a BMG, one may first rapidly heat up the sample from room temperature to T_{nose} , keeping the isothermal condition at T_{nose} , and counting the time for crystallization as t_{nose-a} . A possible example of heating method can be found in the published work done by Pogatscher et al. (2014) and Kaltenboeck et al. (2014). Then, for the same BMG alloy, cool the molten alloy rapidly down to T_{nose} , keeping the isothermal condition at T_{nose} , and counting the time of crystallization and denoted as t_{nose-p} . This is usually how the TTT diagram of a BMG sample is determined. A possible example can be found in the published work done by Pogatscher et al. (2014) and Busch (2000). Then, as shown in Eq. (12), Q_t is defined as the ratio between t_{nose-p} and t_{nose-a} .

The quality factor Q_x is a competition between two terms: $I_{nose} \cdot t_{nose}$ and $4N$. When $4N$ is relatively small, the value of Q_x will be close to 1, meaning the pre-existing nuclei in the tested sample are not significant compared to the quantity of quenched-in nuclei at nose temperature. Thus, the quenched-in nuclei dominate the crystallization process, and the sample can be considered as perfect amorphous. On the other hand, when Q_x is close to 0, the amount of pre-existing nuclei in the tested sample is large enough that the effect of crystallization will be dominated by pre-existing nuclei during the laser welding process.

For an LM105 alloy, the calculated Q_t and Q_x are plotted as a function of pre-existing nucleus density as shown in Fig. 4, calculated from Eqs. (12) and (13). It can be seen that both Q_t and Q_x have the same tendency against the increase of pre-existing nucleus density. They are close to 1 when N is smaller than 10^2 1/mm³. Both of the two quality factors decrease dramatically for higher N values. The value Q_x drops faster than

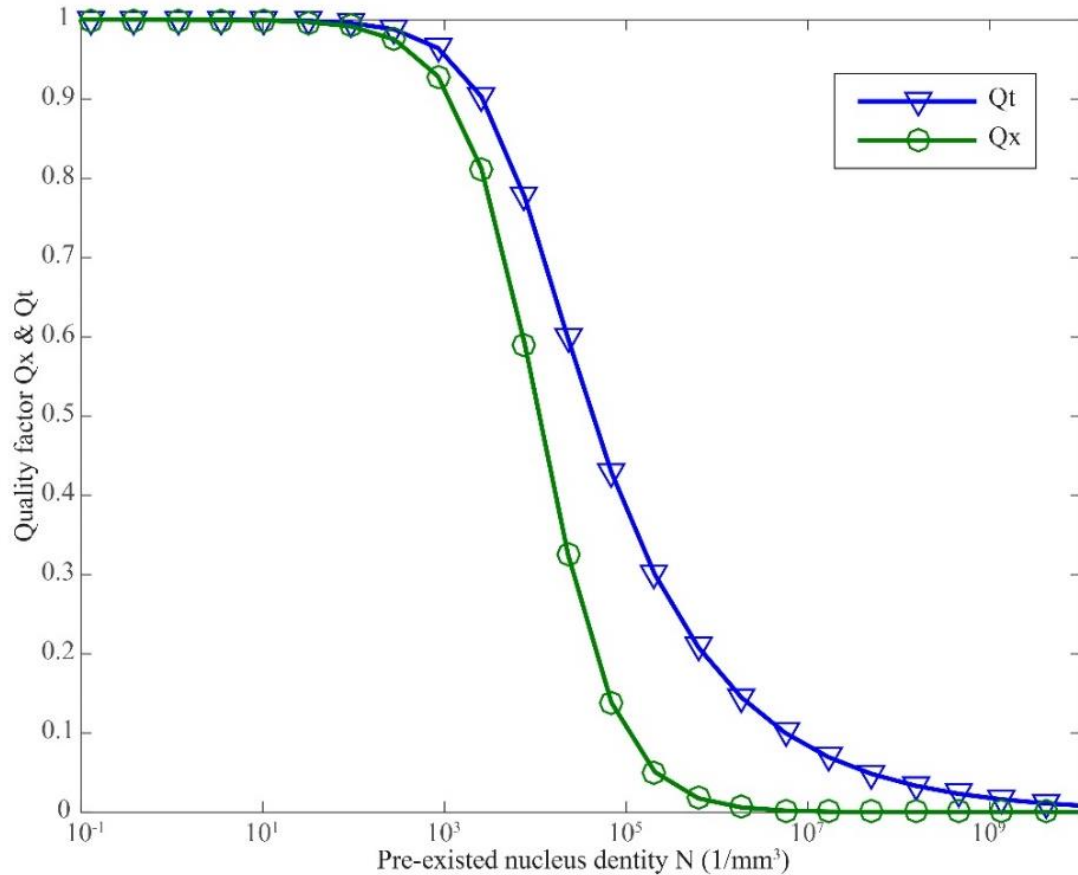


Figure 4. The calculated quality factors Q_t and Q_x against pre-existing nucleus density for LM105 alloy.

Q_t and reaches almost 0 at $N = 10^7$ 1/mm³, while the value of Q_t is about 0.1 at $N = 10^7$ 1/mm³ and continues decreasing for higher N values. For any metallic glass system, a higher pre-existing nucleus density is equivalent to a lower quality factor.

The quality factors are related to the pre-existing nucleus density. These pre-existing nuclei are actually the quenched-in nuclei generated during the cooling process when they were cast. Then, the cooling rate, or more accurately, the temperature history during casting process, determines the pre-existing nucleus density in the sample. Figure 5 shows the calculated evolution of nucleus density, from Eq. (10), with respect to different cooling

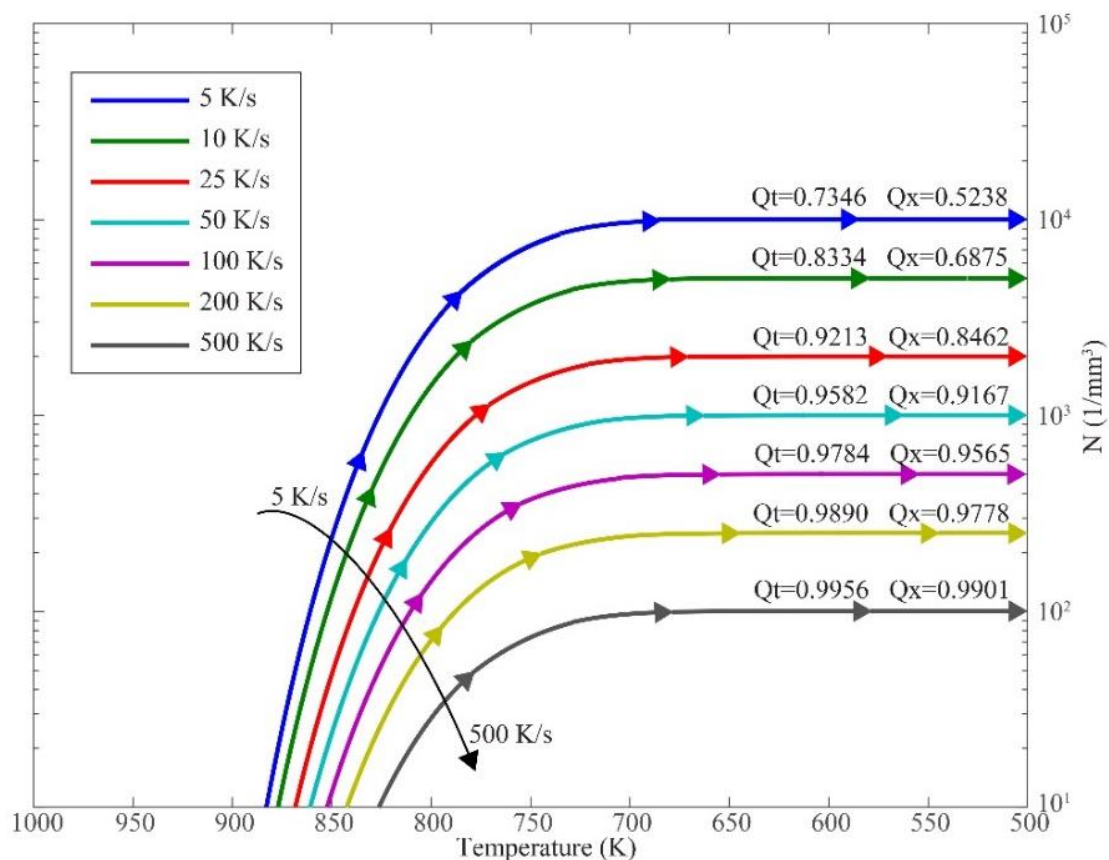


Figure 5. The effect of cooling rate on the quality factors and nucleus density during cast process from molten LM105.

rates (assumed constant) during casting process, as well as the final quality factor of the cast BMGs. For the cooling rates below 50 K/s, nucleus density higher than 10^3 1/mm³ is found in the cast part. The resulting quality factors are 0.9582 for Q_t and 0.9167 for Q_x . The cooling rate of 50 K/s is higher than the critical cooling rate of 10 K/s that was reported for LM105. It would then be considered for fully amorphous at a cooling rate of 50 K/s. However, further increasing the cooling rate is still meaningful. As can be seen from Fig. 5, when the cooling rate increases from 50 K/s to 500 K/s, the nucleus density decreases one order of magnitude. This result indicates that enhancing the cooling rate during casting

process, even when it is already beyond the critical cooling rate, is always useful. A higher cooling rate always results in less nucleus density in the cast BMG and, hence, enhances the ability of the cast BMG in retaining its amorphous status under further heating process, for example, laser welding.

6. CRYSTALLINE EVOLUTION DURING LASER WELDING

In the above discussion, the alloy temperature is assumed to be constant (isothermal) in order to determine the TTT curves. In laser welding experiment as shown in Fig. 2, temperature in the BMG sample is a function of time and space which can be obtained by a heat transfer model. In heat transfer model the following assumptions are made:

1. Latent heat is ignored because the melting and solidification are very rapid, and there is a very short time-lag between melting and solidification. Also, the latent heat energy is smaller than the laser energy.
2. Only heat conduction is considered and there is no melt flow. This can be justified that there is a very short melt life, due to rapid melting and immediately rapid solidification. In addition, as laser power is low and scan speed is high, the melt pool is relatively shallow and possible melt flow is minimized. In other words, this is a conduction mode but not a keyhole mode laser welding.

Based on the above assumptions, the energy transport in the BMG is a heat conduction equation which can be written as:

$$\frac{\partial}{\partial x} \left(k \frac{\partial T}{\partial x} \right) + \frac{\partial}{\partial y} \left(k \frac{\partial T}{\partial y} \right) + \frac{\partial}{\partial z} \left(k \frac{\partial T}{\partial z} \right) = \rho C_p \frac{\partial T}{\partial t} \quad (14)$$

where T denotes the temperature, t is the time, k is the thermal conductivity, ρ is the material density, and C_p is the specific heat. The heat losses from the part's surfaces to the surroundings are assumed to be thermal radiation and heat convection:

$$-k \frac{\partial T}{\partial n} = \epsilon \sigma (T^4 - T_\infty^4) + h(T - T_\infty) \quad (15)$$

where n is the surface direction (normal to surface and outward) which can be the x-, y- or z-direction, ϵ is the surface emissivity, σ is the Stefan-Boltzmann constant, and h is the

convective heat transfer coefficient. The laser intensity is assumed to be a Gaussian distribution at the top surface (z -plane), which is expressed as:

$$I_{laser} = \alpha \cdot \frac{2 \cdot P}{\pi r^2} \cdot e^{-\frac{2[(x-vt)^2 + y^2]}{r^2}} \quad (16)$$

where I represents the laser power density, α is the surface absorptivity, P is the laser power, r is the laser beam radius at $1/e^2$ of laser intensity and v is the laser scan speed. The initial temperature is assumed to be uniform and at $T = 300$ K.

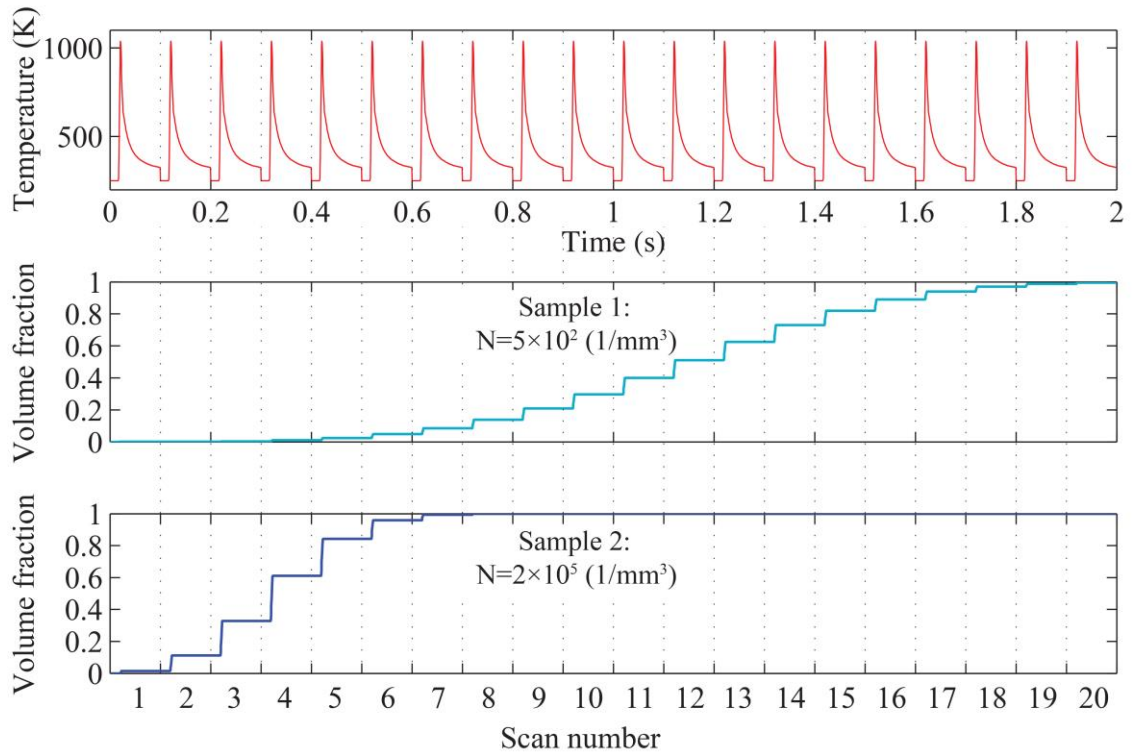


Figure 6. Calculated crystalline phase evolution in HAZ during laser welding.

The time and space dependent temperature, $T(x, y, z, t)$, in the BMG during laser welding can be computed by solving Eq. (14) with boundary conditions Eqs. (15) and (16) and initial condition. The calculated domain was: x (-5 mm, 5 mm), y (-5 mm, 5 mm), and z (0 mm, -0.75 mm). For a selected location in the BMG, the time-dependent temperature can be used to obtain the nucleation rate, I , and crystal growth rate, U , via Eqs. (1) and (3), respectively. These time-dependent I and U values are then plugged into Eq. (7) and a numerical integration is performed to calculate the VF of crystalline phase. Note as the laser scans several times and there is a time lag between any two sequential scans, the percentage of crystalline phase obtained in the previous scan would be considered as the pre-existing nucleus density. As the FZ was melted every time during the laser scan, the pre-existing and quenched-in nuclei in FZ do not accumulate. In HAZ, however, temperatures were not high enough to reach the melting point, so the quenched-in nuclei accumulated through the whole process. In the presented temperature history shown in Fig. 6, we chose a point along the center line just below FZ ($x = 0$ mm, $y = 0$ mm, $z = -0.105$ mm) whose highest temperature has reached 1080 K in each laser scan but not yet melted ($T < T_m = 1085$ K). In the experiment, there was a 30 s interval time between two adjacent laser scans in order to avoid any heat accumulation. The laser scan speed is 100 mm/s and the laser power is 100 W. The cooling rate of Sample 1 during casting is estimated at 100 K/s provided by the manufacturer. Thus, from Eq. (10), the nucleus density for Sample 1 is estimated to be 5×10^2 $1/\text{mm}^3$. Sample 2 in the experiment was annealed at 690 K for 30 min, and the rate of crystal nucleation $I_{T=690K} = 10^2$ $1/\text{mm}^3\text{s}$. Also, from Eq. (10), for Sample 2 it is estimated the pre-existing nucleus density is 2×10^5 $1/\text{mm}^3$ in the calculation.

The evolution of VF of crystalline phase under multiple laser scans is plotted in Fig. 6, calculated from Eq. (7). For Sample 1, the VF increases a little before scan number < 6 . After that, the VF increase gradually to VF = 80% at the 16th scan. After that, the VF increment per laser scan starts to decrease, following the tendency of the Avrami equation (Avrami, 1939; Avrami, 1940), due to the saturation of crystallization. This calculated result yields the same tendency as the experimental observation shown in Fig. 2 (a). In the experiment, the crystallized HAZ becomes observable at the scan number of 10 to 16, and then almost freezes after numbers greater than 20. For Sample 2, the crystallization appears earlier than that of Sample 1 under the exact same temperature history, shown in the lower image in Fig. 6. It can be seen that the VF of crystalline phase increases rapidly to over 50% after the first 4 scans and then quickly yields to saturation after the 7th scan. This calculated result also agrees with the experimental observation shown in Fig. 2 (b), where the crystallized HAZ appears after the 4th scan and almost stops growing after the 7th scans.

The comparison has shown that the CNT is able to describe the crystallization process of a metallic glass alloy with pre-existing nuclei under laser welding conditions. The value of nucleus density in Sample 2 is estimated. As can be seen in the inset of Fig. 5, the gradient of I is large at $T = 690$ K, and thus a small inaccuracy in the temperature may cause a large difference in the N value. To experimentally measure the value of pre-existing nucleus density can be challenging as discussed above. More fundamental research is needed before really understanding the laser welding of metallic glass.

7. CONCLUSIONS

We investigated the effect of pre-existing nucleus density on the crystallization behavior of Zr- based BMG. For two BMG samples, the one with higher pre-existing nucleus density has shown a higher tendency of crystallization compare with the one with lower nucleus density subjected to the same laser process. Two quality factors, Q_t and Q_x , are defined to help quantifying the ability of a cast BMG part to against crystallization under further heat process.

Due to the continuity of temperature, pre-existing nuclei cannot be avoided in any cast BMG part. Increasing the cooling rate can reduce the nucleus density in the cast part. Thus, increasing the cooling rate is always beneficial, even when it is already beyond the critical cooling rate of a given BMG.

Classical nucleation theory is used to analyze the crystallization behavior of BMGs. A ε -shape TTT curve was discovered for a BMG with pre-existing nuclei, which is different from the well-known C-shape TTT curve for a perfect BMG. The results from this study provide fundamental understanding to the experimentally measured TTT diagram for a BMG that the TTT curve for the heating process is different from the TTT curve for the heating process.

ACKNOWLEDGEMENTS

The authors would like to acknowledge the financial support by the Department of Energy (grant number DE-FE0012272), and the University of Missouri System (award number Fast Track-16002R).

REFERENCES

- Avrami, M., 1939. Kinetics of phase change. I. General theory. *Journal of Chemical Physics* 7 (12), 1103–1112. DOI <http://dx.doi.org/10.1063/1.1750380>.
- Avrami, M., 1940. Kinetics of Phase Change. II. Transformation-Time Relations for Random Distribution of Nuclei. *Journal of Chemical Physics* 8 (2), 212–224. DOI <http://dx.doi.org/10.1063/1.1750631>.
- Busch, R., 2000. The thermophysical properties of bulk metallic glass-forming liquids. *The Journal of The Minerals, Metals & Materials Society* 52 (7), 39-43. DOI <https://doi.org/10.1007/s11837-000-0160-7>.
- Evenson, Z., Schmitt, T., Nicola, M., Gallino, I., Busch, R., 2012. High temperature melt viscosity and fragile to strong transition in Zr-Cu-Ni-Al-Nb (Ti) and Cu₄₇Ti₃₄Zr₁₁Ni₈ bulk metallic glass. *Acta Materialia* 60 (12), 4712-4719. DOI <http://dx.doi.org/10.1016/j.actamat.2012.05.019>.
- Inoue, A., 2000. Stabilization of metallic supercooled liquid and bulk amorphous alloys. *Acta Materialia* 48 (1), 279-306. DOI [http://dx.doi.org/10.1016/S1359-6454\(99\)00300-6](http://dx.doi.org/10.1016/S1359-6454(99)00300-6).
- Johnson, W.L., 1999. Bulk glass-forming metallic alloys: Science and technology. *MRS Bulletin* 24 (10), 42-56. DOI <http://dx.doi.org/10.1557/S0883769400053252>.
- Johnson, W.L., Samwer, K., 2005. A universal criterion for plastic yielding of metallic glasses with a $(T/T_g)^{2/3}$ temperature dependence. *Physical review letters* 95 (19), 195501. DOI <http://link.aps.org/doi/10.1103/PhysRevLett.95.195501>.
- Kaltenboeck, G., Harris, T., Sun, K., Tran, T., Chang, G., Schramm, J.P., Demetriou, M.D., Johnson, W.L., 2014. Accessing thermoplastic processing windows in metallic glasses using rapid capacitive discharge. *Scientific Reports* 4, 6441. DOI <https://doi.org/10.1038/srep06441>.
- Li, N., Liu, L., Pan, J., Chan, K.C., 2007. The effect of free volume on the deformation behaviour of a Zr-based metallic glass under nanoindentation. *Journal of Physics D Applied Physics* 40, 6055-6059. DOI <http://dx.doi.org/10.1088/0022-3727/40/19/043>.
- Löffler, J.F., 2003. Bulk metallic glasses. *Intermetallics* 11 (6), 529-540. DOI [http://dx.doi.org/10.1016/S0966-9795\(03\)00046-3](http://dx.doi.org/10.1016/S0966-9795(03)00046-3).

- Lu, Z.P., Li, Y., Ng, S.C., 2000. Reduced glass transition temperature and glass forming ability of bulk glass forming alloys. *Journal of Non-Crystalline Solids* 270 (1–3), 103-114. DOI [http://dx.doi.org/10.1016/S0022-3093\(00\)00064-8](http://dx.doi.org/10.1016/S0022-3093(00)00064-8).
- Lu, Z.P., Liu, C.T., 2002. A new glass-forming ability criterion for bulk metallic glasses. *Acta Materialia* 50 (13), 3501-3512. DOI [http://dx.doi.org/10.1016/S1359-6454\(02\)00166-0](http://dx.doi.org/10.1016/S1359-6454(02)00166-0).
- Martin, I., Ohkubo, T., Ohnuma, M., Deconihout, B., Hono, K., 2004. Nanocrystallization of $Zr_{41.2}Ti_{13.8}Cu_{12.5}Ni_{10.0}Be_{22.5}$ metallic glass. *Acta Materialia* 52 (15), 4427-4435. DOI <http://dx.doi.org/10.1016/j.actamat.2004.05.038>.
- Mukherjee, S., Zhou, Z., Schroers, J., Johnson, W.L., Rhim, W.K., 2004. Overheating threshold and its effect on time–temperature–transformation diagrams of zirconium based bulk metallic glasses. *Applied Physics Letters* 84 (24), 5010-5012. DOI <http://dx.doi.org/10.1063/1.1763219>.
- Park, E.S., Kim, D.H., 2005. Design of bulk metallic glasses with high glass forming ability and enhancement of plasticity in metallic glass matrix composites: A review. *Metals and Materials International* 11 (1), 19-27. DOI <http://dx.doi.org/10.1007/BF03027480>.
- Patel, A.T., Shevde, H.R., Pratap, A., 2011. Thermodynamics of $Zr_{52.5}Cu_{17.9}Ni_{14.6}Al_{10}Ti_5$ bulk metallic glass forming alloy. *Journal of Thermal Analysis and Calorimetry* 107 (1), 167-170. DOI <http://dx.doi.org/10.1007/s10973-011-1591-9>.
- Peker, A., Johnson, W.L., 1993. A highly processable metallic glass: $Zr_{41.2}Ti_{13.8}Cu_{12.5}Ni_{10.0}Be_{22.5}$. *Applied Physics Letters* 63 (17), 2342-2344. DOI <http://dx.doi.org/10.1063/1.110520>.
- Pogatscher, S., Uggowitzer, P.J., Löffler, J.F., 2014. In-situ probing of metallic glass formation and crystallization upon heating and cooling via fast differential scanning calorimetry. *Applied Physics Letters* 104 (25), 251908. DOI <http://dx.doi.org/10.1063/1.4884940>.
- Schroers, J., Busch, R., Masuhr, A., Johnson, W.L., 1999. Continuous refinement of the microstructure during crystallization of supercooled $Zr_{41}Ti_{14}Cu_{12}Ni_{10}Be_{23}$ melts. *Applied Physics Letters* 74 (19), 2806-2808. DOI <http://dx.doi.org/10.1063/1.124020>.
- Schroers, J., Masuhr, A., Johnson, W.L., Busch, R., 1999. Pronounced asymmetry in the crystallization behavior during constant heating and cooling of a bulk metallic glass-forming liquid. *Physical Review B* 60 (17), 11855. DOI <http://dx.doi.org/10.1103/PhysRevB.60.11855>.

- Schroers, J., Johnson, W.L., 2000. History dependent crystallization of $Zr_{41}Ti_{14}Cu_{12}Ni_{10}Be_{23}$ melts. *Journal of Applied Physics* 88 (1), 44-48. DOI <http://dx.doi.org/10.1063/1.373621>.
- Schroers, J., 2010. Processing of bulk metallic glass. *Advanced Materials* 22 (14), 1566-1597. DOI <https://dx.doi.org/10.1002/adma.200902776>.
- Shen, Y., Li, Y., Chen, C., Tsai, H.L., 2017. 3D printing of large, complex metallic glass structures. *Materials and Design* 117, 213-222. DOI <http://dx.doi.org/10.1016/j.matdes.2016.12.087>.
- Shen, Y., Li, Y., Tsai, H.L., 2017. Evolution of crystalline phase during laser processing of Zr-based metallic glass. *Journal of non-Crystalline Solids* under review, Submitted on Aug 1st.
- Sun, H., 2010. Microstructure evolution of bulk metallic glasses via laser processing. Doctoral dissertation, The Ohio State University.
- Telford, M., 2004. The case for bulk metallic glass. *Materials Today* 7 (3), 36-43. DOI [http://dx.doi.org/10.1016/S1369-7021\(04\)00124-5](http://dx.doi.org/10.1016/S1369-7021(04)00124-5).
- Tkatch, V.I., Limanovskii, A.I., Kameneva, V.Y., 1997. Studies of crystallization kinetics of $Fe_{40}Ni_{40}P_{14}B_6$ and $Fe_{80}B_{20}$ metallic glasses under non-isothermal conditions. *Journal of materials science* 32 (21), 5669-5677. DOI <http://dx.doi.org/10.1023/A:1018601330212>.
- Uhlmann, D.R., 1972. A kinetic treatment of glass formation. *Journal of Non-Crystalline Solids* 7 (4), 337-348. DOI [https://doi.org/10.1016/0022-3093\(72\)90269-4](https://doi.org/10.1016/0022-3093(72)90269-4).
- Wang, W.H., Dong, C., Shek, C.H., 2004. Bulk metallic glasses. *Materials Science and Engineering: R: Reports* 44 (2-3), 45-89. DOI <http://dx.doi.org/10.1016/j.mser.2004.03.001>.
- Williams, E., Lavery, N., 2017. Laser processing of bulk metallic glass: A review. *Journal of Materials Processing Technology* 247, 73-91. DOI <https://doi.org/10.1016/j.jmatprotec.2017.03.034>.
- Zhang, L., Pauly, S., Tang, M.Q., Eckert, J., Zhang, H.F., 2016. Two-phase quasi-equilibrium in β -type Ti-based bulk metallic glass composites. *Scientific Reports* 6, 19235. DOI <http://dx.doi.org/10.1038/srep19235>.

IV. THE EFFECT OF OVERLAP ON CRYSTALLIZATION OF BULK METALLIC GLASS DURING ADDITIVE MANUFACTURING

Yiyu Shen, Yingqi Li, and Hai-Lung Tsai

Department of Mechanical and Aerospace Engineering

Missouri University of Science and Technology, Rolla, MO 65409, U.S.A.

ABSTRACT

Additive manufacturing (AM) offers a possibility of producing large, complex bulk metallic glass (BMG) parts without the limitation of critical thickness. To prevent crystallization which ruins the mechanical properties of the BMGs, the processing parameters during AM are critical. In this paper, we investigate the effect of overlap on the crystallization behavior of Zr- based metallic glass ($Zr_{52.5}Ti_5Al_{10}Ni_{14}Cu_{17.9}$, at. %) during laser based additive manufacturing. We also discussed the difference between ‘single laser track’ and ‘multi- laser track’ using a general mathematical model including heat transfer and nucleation. This bridge the knowledge between fundamental research and the real world additive manufacturing application.

Key words: Bulk Metallic Glass, Laser Material Processing, Additive Manufacturing, Nucleation

1. INTRODUCTION

Bulk metallic glasses (BMGs) have tracked many research interests in the past few decades because of their unique mechanical properties. However, because of the requirement of fast cooling, the maximum casting size of BMGs are limited. Laser based additive manufacturing (AM) can be an alternative method to achieve large size BMG parts. This is the main driven force that there is increasing quantity of results reported within the field of laser BMG interaction.

The study on laser welding of BMG with ‘single laser track’ can be date back to 2000s [1-10]. A common agreement been made is that the crystalline phase in laser welded BMG is more likely occur in the heat-affected zone (HAZ) rather in the fusion zone (FZ). Here the FZ is defined as the location where the material is once melted, while the HAZ is defined as the material surrounds the FZ that has not been melted during the welding process but somehow affected by the high temperature of melting pool. A more detailed review is given by E. Williams [11] recently. However, it has been a long time before the report of the success in manufacturing large BMG part with acceptable density and amorphous. The early quest on AM for BMG starts on 2010s [12 - 14] while the part quality at that time is still unsatisfied. In early 2017, our group have demonstrated a successful manufacturing of Zr- based BMG structure with a novel developed AM technology namely Laser-Foil-Printing [15]. In late 2017, Pauly et al. reported the large BMG part produced by commercialized SLM methods [16]. The time delay is mainly caused by the difference between ‘single laser track’ and ‘multi- laser track’ during laser processing. During the AM, in order to continuously weld the entire layer of material onto the substrate or previous layer, weld bead have to overlap each other. Thus, the AM process essentially stands for

the ‘multi- laser track’ mode. This ‘multi- laser track’ mode causes an unavoidable reheating of the BMG substrate. The reheating process made the crystallization behavior of BMG during additive manufacturing different from those reported work for the case of ‘bead on plate’ condition with single laser track.

The laser BMG interaction is still a new research area and most of the experimental works remains in the try-error stage. Most of the discussion in this area simply remains on the argument of cooling rate, an over- simplified parameter for the casting process. However, the temperature evolution during laser processing is much more complex than casting. Thus, the application of critical cooling rate in laser BMG interaction is questionable. To describe the phase evolution during laser BMG interaction, one may need a theory more fundamental. Recently, we included classical nucleation theory (CNT) in heat transfer model to study the phase evolution during laser BMG interaction and the results matches well with the experimental observation done by our own [17, 18] and other groups [19].

In this paper, the developed model is used to demonstrate the gap between ‘single laser track’ and ‘multi- laser track’ modes. Both ‘single laser track’ and ‘multi- laser track’ experiments are conducted in order to demonstrate the effect of laser bead overlap on the crystallization behavior of BMG. Then by using the numerical model combining heat transfer and CNT, the cutting-edge processing parameters against crystallization during laser based additive manufacturing is discussed.

2. EXPERIMENT

Bead-on-plate laser welding are carried out on casted BMG substrates. Counter gravity casted LM105 ($Zr_{52.5}Ti_5Al_{10}Ni_{14}Cu_{17.9}$, at. %) provided by Liquidmetal Technologies, Inc., is used as substrate. A CW laser (YLR-1000, IPG Inc.) with wavelength of 1070 μm is used as laser source. The laser beam diameter D on the focal plane is 430 μm . The motion of the laser beam is controlled by a scanner (hurrySCAN III, SCANLAB Inc.) with the maximum scan speed of 2000 mm/s at the focal plane. All experiments are conducted in an argon chamber in order to avoid any possible oxidization during welding.

The laser welding experiment are separate into two parts. The first part is designed to demonstrate the crystallization behavior of selected BMG under single laser track. The second part includes different level of overlap for several laser tracks. In the first part of the experiment, laser power (P) is controlled as 200 W, the weld speed (v) is set to 20, 50, 100 and 200 mm/s. For the second part, laser power and laser weld speed are set to pre-selected values of to 200 W and 100 mm/s, respectively. The laser hatch space (h) is set to 20, 50, 200 and 250 μm . Between each laser track, 30 seconds interval time are added. This interval time is added in order to avoid any accumulation of heat. After the experiment, the samples are cross-sectioned, polished, etched by a solution of 100 ml H_2O , 2 ml H_2O , and 0.1 ml HF, and then examined by optical microscope (OM).

Table 1. Selected parameters applied in the experiments.

Single laser track	Laser power (W)	200
	Scan speed (mm/s)	20, 50, 100, 200
Multi- laser track	Laser power (W)	200
	Scan speed (mm/s)	100
	Interspace (μm)	20 50 200 250

3. RESULTS

Fig. 1 presents the cross-sectional image of laser welded LM105 at laser power of 200 W and laser scan speed of 20, 50, 100 and 200 mm/s. The direction for laser track is perpendicular toward the paper. For all four cases, there is not crystallization phase obtained in the FZ. While in the HAZ, a clear crystallized phase is observed at laser scan speed of 20 mm/s and 50 mm/s. For scan speed of 100 mm/s and above, crystallized HAZ is not observed. By increasing laser scan speed, crystallization in HAZ can be sufficiently limited. The size of FZ, both the width and the depth, decrease with the increase of scan speed as expected. Clearly from the experiments results, for single laser track, at $P = 200$ W and $v = 100$ & 200 mm/s the crystallization phenomenon can be avoided. Then the next question rises at: can these parameters been used for 'multi- laser track' situation, and if not where is the difference in fundamental. To address this question, $P = 200$ W and $v = 100$ mm/s is applied for 'multi- laser track' experiment.

Fig. 3 shows the cross-sectional image of 'multi- laser track' welded BMG with 20, 50, 200 and 250 μm interspace. The direction for each laser track is perpendicular toward the paper. The first laser track is located on the very left, and each next track is placed on the right of the previous laser track with a certain interspace. The interspaces are 20, 50, 200 and 250 μm from Fig. 2 (a) to Fig. 3 (d). Laser power is 200 W and laser scan speed is 100 mm/s. Again the FZ for all cases are remained in amorphous. At 20 μm interspace as shown in Fig. 2 (a), the whole HAZ below the FZ is crystallized. At 50 μm interspace as shown in Fig. 2 (b), the left part of the HAZ is observed crystallized. While there is no crystalline phase observed on the right part of the HAZ area. When the interspace is increased to 200 μm , the crystalline phase separates into small, discontinued blocks as

shown in Fig. 2 (c). The size of the crystalline blocks are decreased when the interspace is increased to 250 μm as shown in Fig. 2(d), but is still not fully suppressed.

Clearly, for the same set of laser parameters, crystallization phase those observed in ‘multi- laser track’ case is not shown in the ‘single laser track’ case. Kim [9] have observed a similar case in the work published in 2006. He concluded the reason as the accumulation of heat between two laser scans. However, in the presented work, accumulation of heat is taken care of by addressing enough time gap (30 seconds) between

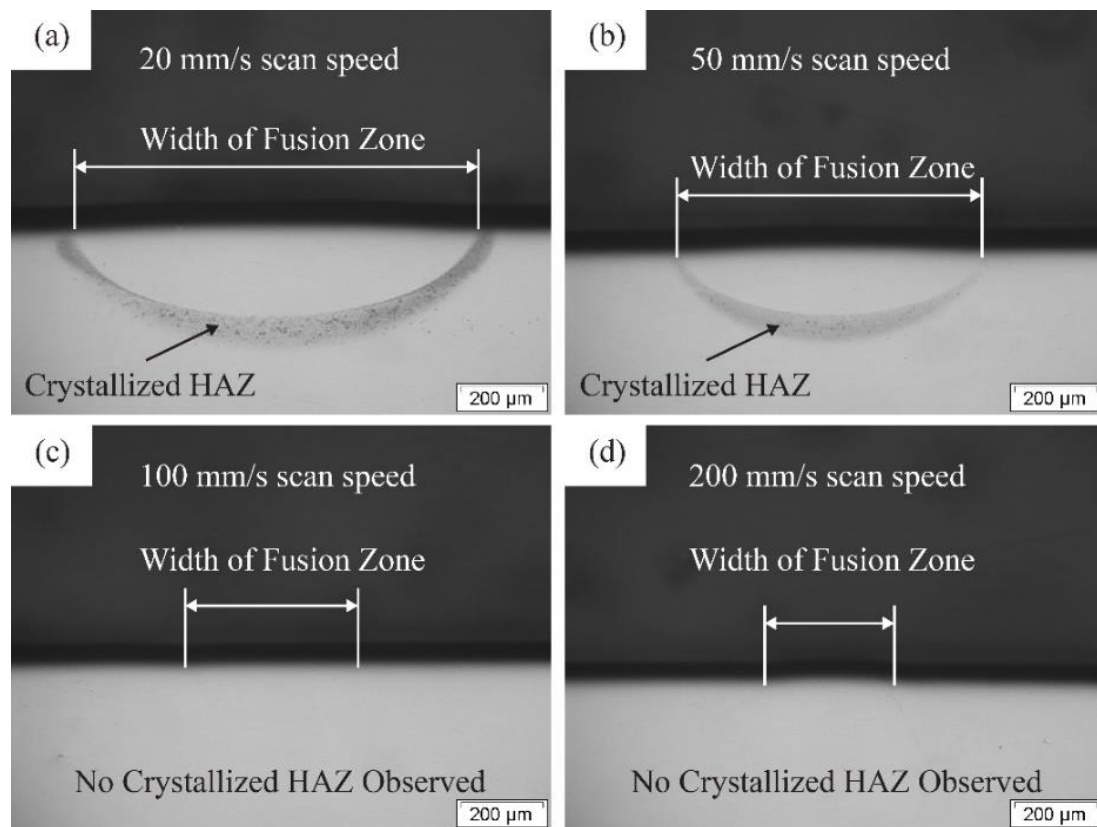


Figure 1. OM photography on cross-section of laser welded LM105 sample with 200 W laser power and 20, 50, 100 and 200 mm/s scan speed.

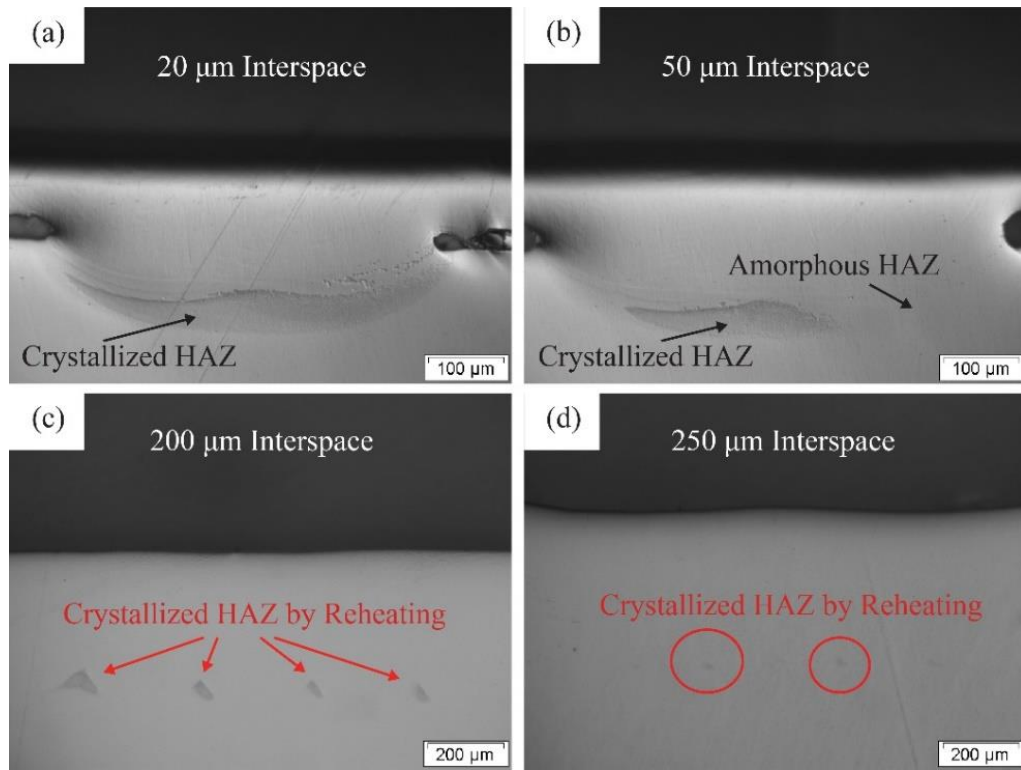


Figure 2. OM photography on cross-section of 'multi-laser track' on LM105 sample with 200 W laser power, 100 mm/s scan speed and different interspaces.

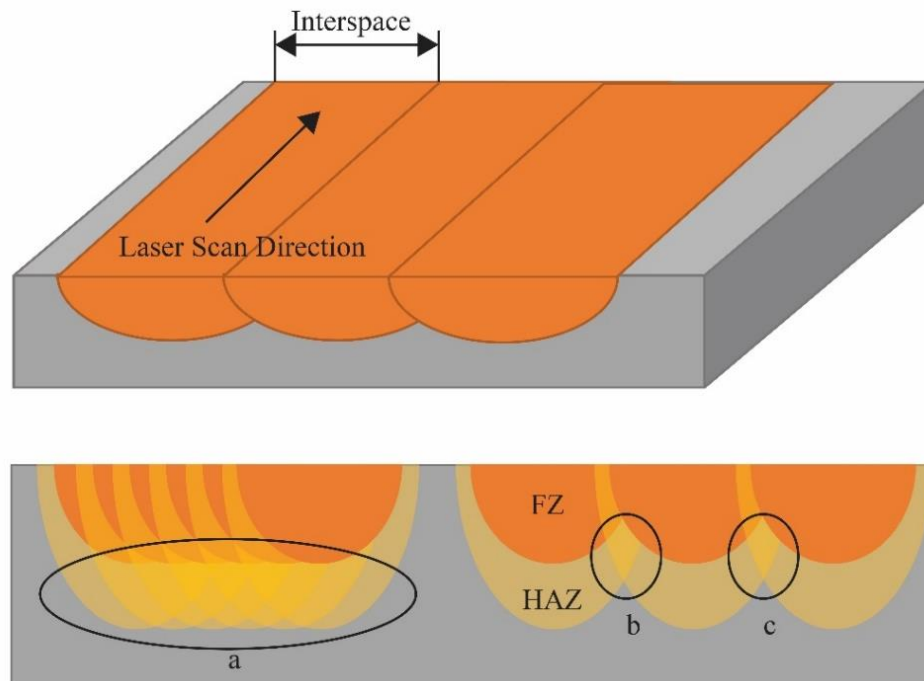


Figure 3. Schematic experimental setup and the orientation of 'multi-laser track'.

any two laser scans. Thus, the sample is ensured at room temperature at the starting of each laser scan and the pre- or post- heating effect is excluded. From the classical nucleation theory point of view, we conclude the difference in generating the crystalline phase is due to the accumulation of nuclei cores. Within the framework of CNT [20, 21], the crystallization process can be divided into two process: the formation of nuclei and their subsequent growth. The nucleation process is described by the factor I , the nucleation rate, with a unit of $\text{mm}^{-3}\text{s}^{-1}$. It stands for the rate of nuclei core generation and for the most of case, temperature dependent. The diffusion limited growth process is described by the factor U , the crystalline grow velocity, with a unit of mm/s . It stand for the one dimensional growth velocity of each individual nuclei core and also temperature dependent. Since there is so far no evident that the crystalline phase in BMG decompose back to its amorphous phase, it is reasonable to assume that the crystalline phase and nuclei core in BMG only return to its amorphous status at melting. Then at the HAZ where BMG remains solid during the laser welding process, the generated nuclei cores accumulates at where they are and are going to affect the future crystallization processing as the pre-existing nuclei cores.

Whit the CNT in mind, the experimental results shown in Fig. 2 can be explained. A schematic illustration of the experiment is given in Fig. 3. Affected by the accumulated nuclei, material in the HAZ has a higher crystallization tendency [18]. When the interspace is small, the whole HAZ beneath the FZ are reheated several times and get crystallized as a whole part. This is the situation as shown bottom left of Fig. 3. When the interspace is large, only part of the HAZ is reheated. Therefor a periodic, discontinued crystallization spots are expected as shown in Fig. 3.

To conclude from this point, the amorphous/crystalline phase due to laser based processing of BMG depends not only on processing parameters, but also the design of laser scan path, in another word the scanning strategy. This effect need to be fully considered in a real AM process case. When the overlap interspace is too small, the crystallization in HAZ can be accelerated due to accumulation of nuclei; while when the interspace is too large, insufficient bonding may take place.

4. DISCUSSION

As discussed, to produce a BMG part with laser based AM technology, it always follows the ‘multi- laser track’ case with a certain degree of overlap for each individual ‘single laser track’. According to our experimental results, the crystallization behavior of LM105 alloy during laser processing depends on both laser parameters and the scanning strategy. Numerical model would be helpful in further investigate the AM process.

To quantitatively study the crystallization during laser welding of BMG, a coupled model which combines the heat transfer theory and the classical nucleation/growth theory (CNT) is used. The heat transfer model is used to estimate the thermal history at the selected point, while the CNT model is used to estimate the evolution of volume fraction of crystalline phase in the HAZ. Detail of the model was discussed in our earlier publications [15, 17, 18]. To better conduct the discussion here, the model is also briefly introduced here.

Within the frame of CNT, crystallization process includes nuclei formation and their subsequent growth. For an under cooled liquid, the temperature dependent nucleation rate I writes [17, 20]:

$$I = A \cdot D \cdot \exp\left(-\frac{\Delta G^*}{kT}\right) \quad (1)$$

where A is a constant, D is the effective diffusivity, k is the Boltzmann’s constant, T denotes the absolute temperature and ΔG^* is the thermodynamic potential barrier of nucleation. ΔG^* can be calculated as:

$$\Delta G^* = \frac{16\pi\sigma^3}{3\Delta G^2} \quad (2)$$

where σ denotes the interface energy between nucleus and melt, and ΔG is the difference of Gibbs free energy between the solid and liquid (amorphous) phase. Considering the

diffusion limited crystalline growth only, the crystalline growth velocity U can be expressed by [17, 20]:

$$U = \frac{D}{a} [1 - \exp(-\frac{\Delta G}{kT})] \quad (3)$$

where a is the average interatomic spacing. Here only diffusion limited crystalline growth is considered because from the experiment, the crystallization is taken place at the HAZ. Since the BMG in HAZ remains solid, the fluid behavior is not significant and can be ignored. Then the three dimensional evolution of volume fraction for the crystalline phase writes [17, 18]:

$$X(T, t) = 1 - \exp \left\{ -\frac{4\pi}{3} \cdot \left[\int_0^t I(T, \tau) \cdot \left[\int_\tau^t U(T, t') dt' \right]^3 d\tau \right] + N \cdot \left[\int_0^t U(T, t'') dt'' \right]^3 \right\} \quad (4)$$

Here X denotes the volume fraction of crystalline phase evolution of a BMG, and N is the pre-existed nucleus density. The I and N related terms in Eq. (4) represents, respectively, the effect of quenched-in and pre-existing nuclei on crystallization. The temperature-dependent effective diffusivity D is calculated from measured viscosity [22] by Stork-Einstein relation [21]. The Gibbs free energy difference between undercooled liquid and corresponding crystal solid, ΔG , as a function of temperature reported by Patel [23] is used. The average interatomic spacing a of 2.6×10^{-7} mm is used calculated from the weighted atomic percentage. $\sigma = 0.076$ J/m² and $A = 2.5 \times 10^{33}$ are used in calculation I and the determination of these values are expressed in our previous paper [17, 18].

The double integral in Eq. (4) considers each nuclei core forms at time τ , and its growth from time τ to the terminate time, t , for the whole process. The pre-existing nuclei cores within BMG matrix is also considered in Eq. (4) as N . For constant cooling such like casting case, the Eq. (4) can be simply solved using an assumed cooling rate from the

melting temperature with N set to 0. For the laser welding process, on the other hand, the temperature is more complex. Therefore, another heat transfer model is employed to obtain the thermal history.

Again because from experiment, the crystallization is taken place at the HAZ and the HAZ remains solid during laser processing, only heat conduction is taken into consideration while fluid behavior in FZ is not included. For heat conduction only, the governing differential equation can be written as:

$$\frac{\partial}{\partial x} \left(k \frac{\partial T}{\partial x} \right) + \frac{\partial}{\partial y} \left(k \frac{\partial T}{\partial y} \right) + \frac{\partial}{\partial z} \left(k \frac{\partial T}{\partial z} \right) = \rho C_p \frac{\partial T}{\partial t} \quad (5)$$

where T denotes the temperature, t is the time, k is the thermal conductivity, ρ is the material density and C_p is the specific heat. The heat losses are:

$$-k \frac{\partial T}{\partial n} = \epsilon \sigma (T^4 - T_\infty^4) + h(T - T_\infty) \quad (6)$$

where n is the normal direction to the surface which can be the x-, y- or z-direction, ϵ is the surface emissivity, σ is the Stefan-Boltzmann constant h is the convective heat transfer coefficient and T_∞ is the ambient temperature. The laser power is assumed to be a Gaussian distribution at the top surface (z-plane) which is expressed as:

$$I_{laser} = \alpha \cdot \frac{2 * P}{\pi r^2} \cdot e^{\frac{-2[(x-vt)^2 + y^2]}{r^2}} \quad (7)$$

where I_{laser} represents the laser power density, α is the surface absorptivity, P is the laser power, r is the laser beam radius and v is the laser scan speed. In this study, the heat transfer model is computed with commercial software package COMSOL Multi-physics 5.0 with constants introduced in our earlier paper [15]. The x-, y-, z-coordinate system was established at the center of the top surface for the plate with the dimensions of 10 mm by

10 mm by 0.75 mm. The calculated domain was: x (-5 mm, 5 mm), y (-5 mm, 5 mm), and z (0 mm, -2.5 mm).

Both the ‘single laser track’ and ‘multi- laser track’ cases are calculated. For the ‘single laser track’, the laser scanned from ($x = -5$ mm, $y = 0$ mm, $z = 0$ mm) toward the positive x direction at different speeds listed in Table. 1. Since temperature history is highly location dependent, we carefully chose a point along the center line just below FZ ($[0, 0, -d]$, d is the depth and is different at each laser scan speed) whose highest temperature has reached 1080 K in each laser scan but not yet melted ($T < T_m = 1085$ K). Hence this point represents the HAZ during laser processing that not melted. For the ‘multi- laser track’ cases, the first laser track scans from ($x = -5$ mm, $y = -1$ mm, $z = 0$ mm) toward the positive x direction. Then the following laser tracks scan from ($x = -5$ mm, $y = -1+n*y_i$ mm, $z = 0$ mm) toward the positive x direction, where n represents the scan number and y_i is the interspace value of each case listed in Table. 1. There are in total 10 scans for each selected interspace value. The HAZ points for ‘multi- laser track’ cases are carefully selected where most reheated that as demonstrated in Fig. 3 point b and c.

The calculated temperature history from the heat transfer model for 4 different scan speeds presented in Fig. 2 are plotted in Fig. 4. The temperature dependent I and U are also plotted, from Eqs. (1) - (3), and the details of calculation I and U have been included in our earlier publication. According to Eq. (4), the resulting volume fraction of crystalline phase depends on the I and U values, and I and U are temperature dependent. Then degree of crystallization depends on the period of time that the material is held within the temperature range where the values of I and U are significant. Taken 1% of the Maximum value as the criteria, the I value is significant at the range (665 K, 890 K), and the U value is significant

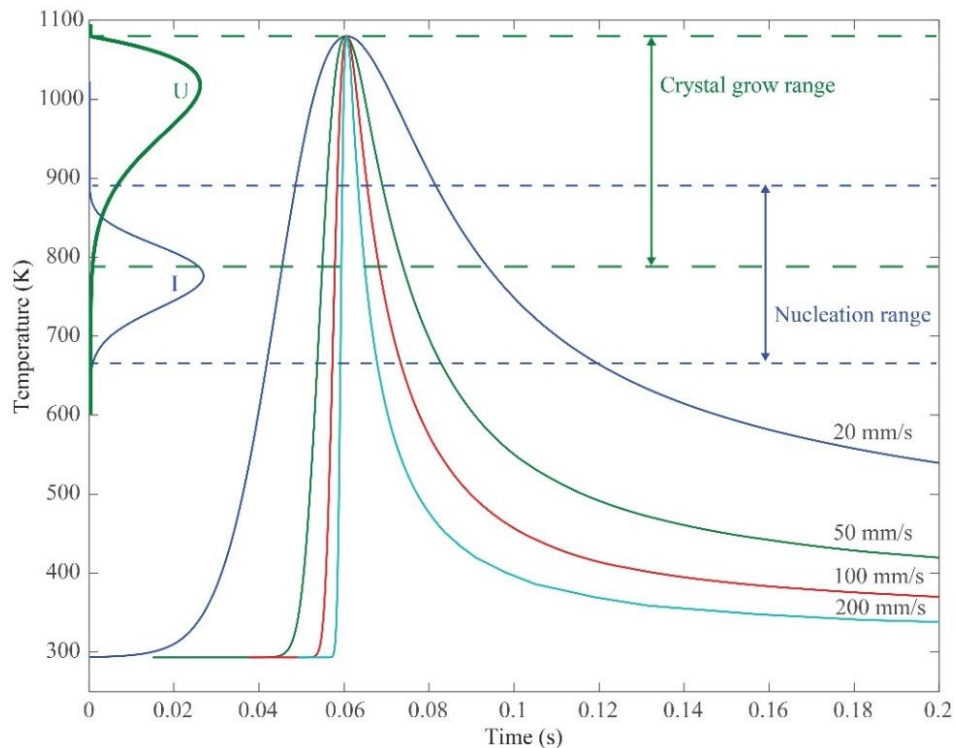


Figure 4. Calculated temperature history with 200 W laser power and 20, 50, 100 and 200 mm/s scan speed. Comparison of the calculated and experimental measured width and depth of FZ.

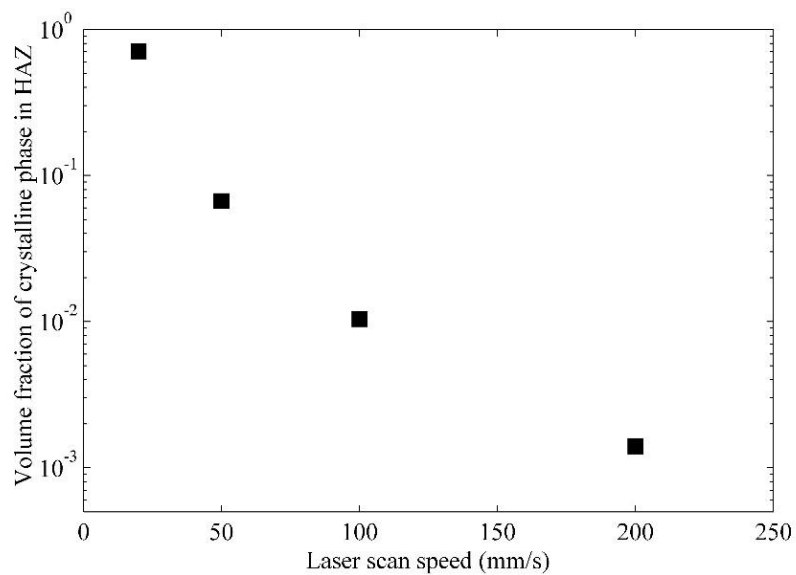


Figure 5. Calculated crystalline volume fraction in HAZ against laser scan speed.

at (785 K, 1080 K). Therefore, we consider the temperature range (665 K, 1080K) as the range where crystallization is most significant.

From Fig. (4), the time period with the critical temperature range heavily depends on the laser scan speed. For the speed of 20, 50, 100, 200 mm/s, the time periods are 78, 34, 16, and 7 ms, respectively. The resulting volume fraction of crystalline phase are calculated as 70.06%, 6.69%, 1.04%, and 0.14%, respectively as shown in Fig. 5.

The calculated temperature history and the corresponding VF evolution of crystalline phase for 'multi- laser track' is plotted in Fig. 6 for laser power of 200W, laser scan speed of 100 mm/s and interspace of 20 μm (Fig.6 (a)), 200 μm (Fig. 6 (b)), and 250 μm (Fig.6 (c)). There are more than 7 reheating circles been calculated. Only 7 of them (most serious heated) are presented here because it is able to show the crystallization tendency in a clear order. In a heat transfer model for the laser BMG interaction case, the temperature history is different from place to place. Thus the selection the position of interest can be somewhat arbitrarily. In this work for different overlap interspaces, we carefully pick the position in HAZ that between to FZ case by case. This is the position where theoretically most heat affected, and where crystallization is observed in experiment as shown in Fig. 2 (c) and (d). Also in the experiment shown in Fig. 3, there is 30 second interval time between each two laser track in order to avoid possible heat accumulation. In the model, the crystallization process is almost freeze at temperature below 500 K. Thus in order to reduce the computational time, the calculation terminates while temperature drops back and immediately rolls into the next welding circle.

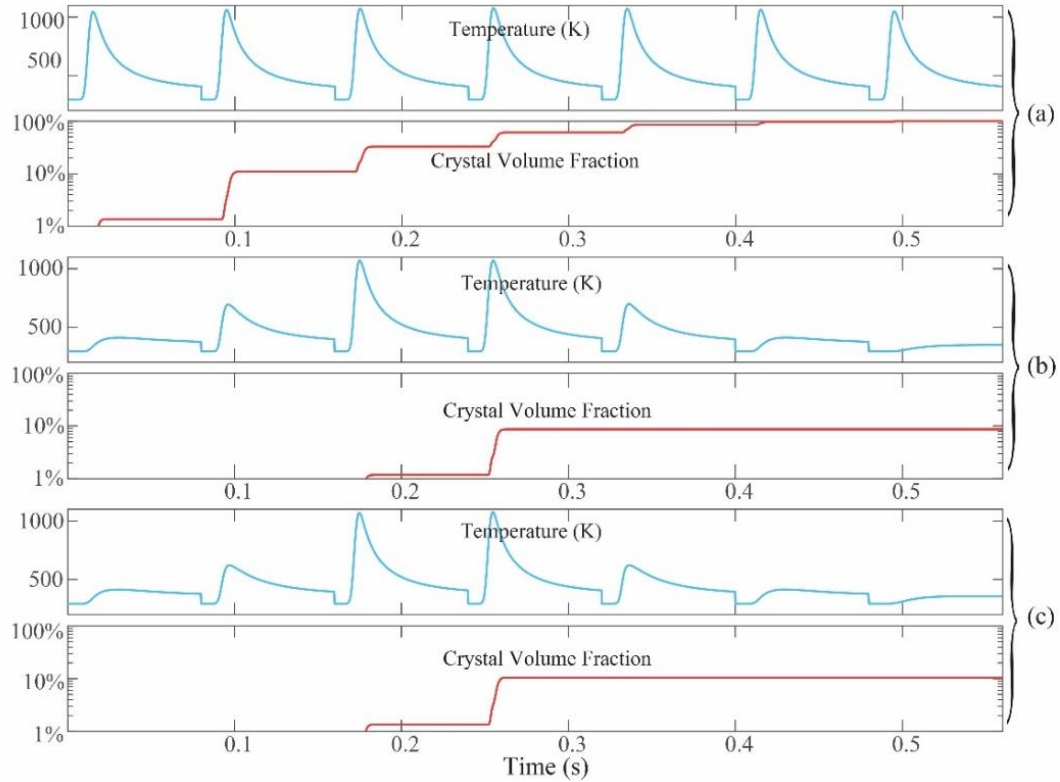


Figure 6. Calculated temperature history and corresponding crystallization for interspace of (a) 20 μm , (b) 200 μm and (c) 250 μm .

Fig. 6 (a) presents the temperature and crystalline percentage evolution at the overlap of 20 μm . The peak temperatures reached in 7 scans are all over 1000 K, indicating that the HAZ is reheated seriously. Due to the nuclei accumulation in the HAZ, the HAZ crystallized fast and reaches almost fully crystal after the 5th laser weld. When the interspace is increased to 200 μm , the overlap of HAZ is decreased significantly. The calculated temperature history is shown in Fig. 6 (b). Only 2 of the laser scans have risen the temperature to over 1000 K (No. 3 and No. 4). The laser welds except these 2 scans, however, only push the temperature up to around 500 K, which has almost no contribution on the crystallization process. The final VF of crystallization phase ends up at around 10%. When the interspace is further rise to 250 μm , the temperature history doesn't change much

as shown in Fig. 6 (b). Thus the corresponding crystallization process has yield a similar result and ends up with around 10%, too.

It is then realized that 2 is the minimum number of thermal circle to sub-melting temperature that a BMG would experience during AM process. This is because in order to achieve a fully welded part by AM, each FZ of laser weld have to overlap with each other, at some degree, to ensure the solid bonding. HAZ would always exist and surround the FZ because of continuity of temperature distribution. Thus the overlap of HAZ cannot be avoided, too. As a result, like the point b and c highlighted in Fig. 3, the overlapped HAZ would then be heated up twice to sub-melting temperature.

5. CONCLUSION

The general difference of ‘single laser track’ and ‘multi- laser track’ mode in laser BMG interaction is studied in this paper experimentally and numerically. This bridges the fundamental research between laser welding of metallic glass and the laser based additive manufacturing of metallic glass. The following conclusions are drawn:

1. The processing parameters who does not cause crystallization in ‘single laser track’ model, may leads to observable crystallization under ‘multi- laser track’ mode.
2. The overlap of laser track causes reheating in HAZ, which enhances the crystallization. To suppress crystallization in the AM produced BMG part, the parameters need to be carefully selected.

The use of laser in processing BMG have shown a decent potential. The research of the laser based AM of BMG should continue to grow for several areas such like new material, mechanical properties, functional part and laminated structures. The layer thickness can be another critical effect in laser based AM for BMG and further study is demanded. The math model introduced in this paper offers a general method in understanding the fundamental mechanism during laser BMG interaction. Further investigations can also been applied into the model such like adding the effect of fluid effect, vaporization and plasma effect, which is not a minor challenge.

ACKNOWLEDGEMENTS

The authors would like to acknowledge the financial support by the Department of Energy (grant number DE-FE0012272), and the University of Missouri System (award number Fast Track-16002R).

REFERENCES

- [1] B. Li, Z.Y. Li, J.G. Xiong, L. Xing, D. Wang, Y. Li, Laser welding of Zr₄₅Cu₄₈Al₇ bulk glassy alloy, *Journal of Alloys and Compounds* 413 (1–2) (2006) 118–121. DOI <http://dx.doi.org/10.1016/j.jallcom.2005.07.005>.
- [2] G. Wang, Y.J. Huang, M. Shagiev, J. Shen, Laser welding of Ti₄₀Zr₂₅Ni₃Cu₁₂Be₂₀ bulk metallic glass, *Materials Science and Engineering: A* 541 (2012) 33–37. DOI <http://dx.doi.org/10.1016/j.msea.2012.01.114>.
- [3] Y. Kawahito, T. Terajima, H. Kimura, T. Kuroda, K. Nakata, S. Katayama, A. Inoue, High-power fiber laser welding and its application to metallic glass Zr₅₅Al₁₀Ni₅Cu₃₀, *Materials Science and Engineering: B* 148 (1–3) 2008 105–109. DOI <http://dx.doi.org/10.1016/j.mseb.2007.09.062>.
- [4] B. Chen, T.L. Shi, M. Li, F. Yang, F. Yan, G.L. Liao, Laser welding of annealed Zr₅₅Cu₃₀Ni₅Al₁₀ bulk metallic glass, *Intermetallics* 46 (2014) 111–117 DOI <http://dx.doi.org/10.1016/j.intermet.2013.11.008>.
- [5] B. Chen, T. Shi, M. Li, Z. Zhang, Z. Zhu, G. Liao, Laser welding of Zr₄₁Ti₁₄Cu₁₂Ni₁₀Be₂₃ bulk metallic glass: experiment and temperature field simulation, *Advanced Engineering Materials* 15 (5) (2013) 407–413. DOI <http://dx.doi.org/10.1002/adem.201200308>.
- [6] H. Sun, K.M. Flores, Microstructural analysis of a laser-processed Zr-based bulk metallic glass, *Metallurgical and Materials Transactions A* 41(7) (2010) 1752–1757. DOI <http://dx.doi.org/10.1007/s11661-009-0151-4>.
- [7] H.S. Wang, H.G. Chen, J.S.C. Jang, M.S. Chiou, Combination of a Nd:YAG laser and a liquid cooling device to (Zr₅₃Cu₃₀Ni₉Al₈)Si_{0.5} bulk metallic glass welding, *Materials Science and Engineering: A* 528 (1) (2010) 338–341. DOI <http://dx.doi.org/10.1016/j.msea.2010.09.014>.
- [8] H.S. Wang, H.G. Chen, J.S.C. Jang, Microstructure evolution in Nd:YAG laser-welded (Zr₅₃Cu₃₀Ni₉Al₈)Si_{0.5} bulk metallic glass alloy, *Journal of Alloys and Compounds* 495 (1) (2010) 224–228. DOI <http://dx.doi.org/10.1016/j.jallcom.2010.01.132>.
- [9] J. Kim, D. Lee, S. Shin, C. Lee, Phase evolution in Cu₅₄Ni₆Zr₂₂Ti₁₈ bulk metallic glass Nd:YAG laser weld, *Materials Science and Engineering: A* 434 (1–2) (2006) 194–201. DOI <http://dx.doi.org/10.1016/j.msea.2006.06.118>.

- [10] G. Yang, X. Lin, F. Liu, Q. Hu, L. Ma, J. Li, W. Huang, Laser solid forming Zr-based bulk metallic glass, *Intermetallics* 22 (2012) 110-115. DOI <http://dx.doi.org/10.1016/j.intermet.2011.10.008>.
- [11] E. Williams, N. Lavery, Laser processing of bulk metallic glass: A review, *Journal of Materials Processing Technology* 247 (2017) 73-91. DOI <https://doi.org/10.1016/j.jmatprotec.2017.03.034>.
- [12] H. Sun, Microstructure evolution of bulk metallic glasses via laser processing Doctoral dissertation, The Ohio State University (2010). https://etd.ohiolink.edu/pg_10?0::NO:10:P10_ACCESSION_NUM:osu1287025216.
- [13] S. Pauly, L. Löber, R. Petters, M. Stoica, S. Scudino, U. Kühn, J. Eckert, Processing metallic glasses by selective laser melting, *Materials Today* 16 (1–2) (2013) 37-41. DOI <http://dx.doi.org/10.1016/j.mattod.2013.01.018>.
- [14] H.Y. Jung, S.J. Choi, K.G. Prashanth, M. Stoica, S. Scudino, S. Yi, U. Kühn, D.H. Kim, K.B. Kim, J. Eckert, Fabrication of Fe-based bulk metallic glass by selective laser melting: A parameter study, *Materials & Design* 86 (2015) 703-708. DOI <http://dx.doi.org/10.1016/j.matdes.2015.07.145>.
- [15] Y. Shen, Y. Li, C. Chen, H.L. Tsai, 3D printing of large, complex metallic glass structures, *Materials and Design* 117 (2017) 213-222. DOI: <http://dx.doi.org/10.1016/j.matdes.2016.12.087>.
- [16] S. Pauly, C. Schricker, S. Scudino, L. Deng, U. Kühn, Processing a glass-forming Zr-based alloy by selective laser melting, *Materials and Design* 135 (2017) 133-141. DOI <https://doi.org/10.1016/j.matdes.2017.08.070>.
- [17] Y. Shen, Y. Li, H.L. Tsai, Evolution of crystalline phase during laser processing of Zr-based metallic glass, *Journal of non-Crystalline Solids*, Under review Submitted on Aug 1st.
- [18] Y. Shen, Y. Y. Li, H.L. Tsai, Effect of pre-existing nucleus density on crystallization behavior during laser processing of Zr-based metallic glass and the corresponding quality factor, *Journal of Material Processing Technology*, Under review.
- [19] S. Pogatscher, P.J. Uggowitzer, J.F. Löffler, In-situ probing of metallic glass formation and crystallization upon heating and cooling via fast differential scanning calorimetry, *Applied Physics Letters* 104 (25) (2014) 251908. DOI <http://dx.doi.org/10.1063/1.4884940>.

- [20] J. Schroers, A. Masuhr, W.L. Johnson, R. Busch, Pronounced asymmetry in the crystallization behavior during constant heating and cooling of a bulk metallic glass-forming liquid, *Physical Review B* 60 (17) (1999) 11855. DOI <http://dx.doi.org/10.1103/PhysRevB.60.11855>.
- [21] J. Schroers, W.L. Johnson, History dependent crystallization of $Zr_{41}Ti_{14}Cu_{12}Ni_{10}Be_{23}$ melts, *Journal of Applied Physics* 88 (1) (2000) 44-48. DOI <http://dx.doi.org/10.1063/1.373621>.
- [22] Z. Evenson, T. Schmitt, M. Nicola, I. Gallino, R. Busch, High temperature melt viscosity and fragile to strong transition in Zr–Cu–Ni–Al–Nb(Ti) and $Cu_{47}Ti_{34}Zr_{11}Ni_8$ bulk metallic glasses, *Acta Materialia*, 60 (12) (2012) 4712-4719. DOI <http://dx.doi.org/10.1016/j.actamat.2012.05.019>.
- [23] A.T. Patel, H.R. Shevde, A. Pratap, Thermodynamics of $Zr_{52.5}Cu_{17.9}Ni_{14.6}Al_{10}Ti_5$ bulk metallic glass forming alloy, *Journal of Thermal Analysis and Calorimetry* 107 (1) (2011) 167-170. DOI <http://dx.doi.org/10.1007/s10973-011-1591-9>.

SECTION

2. CONCLUSION

The size limitation has been a great restrict for metallic glass alloys of being widely applied as engineering material despite their tremendous mechanical properties. The research presented in this thesis issues on the fundamental of additive manufacturing technology for metallic glass alloys. Experiments were conducted to investigate the laser-metallic glass interaction process. A new additive manufacturing technology, Laser-Foil-Printing, was developed from scratch specifically for metallic glass alloys. The Laser-Foil-Printing technology was demonstrated a decent feasibility in producing metallic glass structures. The relationship between processing parameters and phase evolution of metallic glass must be discovered fundamentally in order to predict, control, and optimize the additive manufacturing process. Thus, a systematic approach for analyzing the crystallization generation within the amorphous matrix was established.

Experimental works on phase transformation investigations discovered that for laser welding of Zr-based LM105 ($Zr_{52.5}Ti_5Al_{10}Ni_{14}Cu_{17.9}$, nominal at. %) metallic glass, crystallization highly depends on the location as well as the laser processing parameters.

The fusion zone (FZ), where the materials were once melted during the laser welding process, retains amorphous nature in all laser parameters applied in this study. The key to the amorphous status in the FZ is the occurrence of melting, who clears the nuclei and the crystalline phase accumulated in the solid material. As a result, the phase evolution within the FZ can be simplified to the well-studied casting case. Obviously, the cooling rate in FZ, during laser welding ($\sim 10^4$ K/s), is orders of magnitude higher than that required for the LM 105 alloy (~ 10 K/s). This result shows the potential of laser as a manufacturing

tool for metallic glass alloys. On the other hand, the crystallization behavior in the heat-affected-zone (HAZ) was found highly related to the laser processing parameters. The critical difference between HAZ and FZ is the materials in HAZ kept solid during the whole laser welding process. Thus, the formed nuclei and crystalline phases, before and during the laser processing, accumulates all over the entire welding, resulting in an accelerated crystallization.

In order to better understand and analyze the fundamental science behind the phase evolution within metallic glass during the additive manufacturing process, we have developed a general mathematical method for simulate the whole process. The model includes two different parts: the heat transfer and the nucleation.

The material behavior was simulated by a classical nucleation theory (CNT) model. In the frame work of CNT, the crystallization is described by two individual processes, the nucleation and the growth of nuclei. First, in the amorphous matrix, tens and hundreds of atoms cluster together into a stable core as nucleus. The formation of nuclei per unit volume and time is described by a temperature-dependent factor named as the rate of nucleation (I). Then, each nuclei works as a 'seed' that grows individually, at a certain rate that is named as the growth rate (U , also temperature-dependent). The growth of the nuclei increase the volume of crystalline phase, and once its size is large enough, it is detected.

The temperature history during laser processing was obtained by a FEM simulation. Extra care was focused on the temperature history in HAZ. It was found that both the heating and cooling rates within HAZ were at the magnitude of 10^4 K/s. By combining the temperature history and the CNT model, the crystalline phase evolution during laser-MG interaction was observed. In the fusion zone, the occurring of melting was able to clear the

generated nuclei and crystalline phase upon heating. This explained why all FZ remained in amorphous nature. On the other hand, the materials in HAZ retained in solid during the whole process. Hence, the nuclei and crystalline phase accumulated over the whole process, resulting the potential crystallization within the HAZ.

In addition, with the developed mathematical model, the crystallization behavior of BMG during additive manufacturing was investigated. We found even with the laser parameters that can avoid crystallization for single track welding, crystalline phase may still be found for continues AM process. This was concluded to be associated with the re-heating in HAZ because of the overlap of laser tracks.

BIBLIOGRAPHY

- [1] W.L. Johnson, Bulk metallic glasses – a new engineering material, *Current Opinion in Solid State and Materials Science* 1 (3) (1996) 383-386. DOI [http://dx.doi.org/10.1016/S1359-0286\(96\)80029-5](http://dx.doi.org/10.1016/S1359-0286(96)80029-5).
- [2] J. Schroers, Processing of bulk metallic glass, *Advanced Materials* 22 (2010) 1566-1597. DOI <http://dx.doi.org/10.1002/adma.200902776>.
- [3] W.L. Johnson, Bulk amorphous metal – An emerging engineering material, *The Journal of The Minerals, Metals & Materials Society* 54 (3) (2002) 40-43. DOI <http://dx.doi.org/10.1007/BF02822619>.
- [4] J.F. Löffler, Bulk metallic glasses, *Intermetallics* 11 (6) (2003) 529-540. DOI [http://dx.doi.org/10.1016/S0966-9795\(03\)00046-3](http://dx.doi.org/10.1016/S0966-9795(03)00046-3).
- [5] W.H. Wang, C. Dong, C.H. Shek, Bulk metallic glasses, *Materials Science and Engineering R* 44 (2-3) (2004) 45-89. DOI <http://dx.doi.org/10.1016/j.mser.2004.03.001>.
- [6] A. Brenner, D.E. Couch, E.K. Williams, Electrodeposition of Alloys of Phosphorus with Nickel or Cobalt, *Journal of Research of the National Bureau of Standards* 44 (1) (1950) 109. DOI <http://dx.doi.org/10.6028/jres.044.009>.
- [7] D. Turnbull, M.H. Cohen, Concerning reconstructive transformation and formation of glass, *The Journal of Chemical Physics* 29 (5) (1958) 1049-1054. DOI <http://dx.doi.org/10.1063/1.1744654>.
- [8] M.H. Cohen, D. Turnbull, Molecular transport in liquids and glasses, *The Journal of Chemical Physics* 31 (5) (1959) 1164-1169. DOI <http://dx.doi.org/10.1063/1.1730566>.
- [9] D.R. Uhlmann, Glass formation, *Journal of Non-Crystalline Solids* 23 (1-3) (1977) 42-85. DOI [http://dx.doi.org/10.1016/0022-3093\(77\)90090-4](http://dx.doi.org/10.1016/0022-3093(77)90090-4).
- [10] W. Klement, R.H. Willens, P. Duwez, Non-crystalline structure in solidified gold-silicon alloys, *Nature* 187 (4740) (1960) 869-870. DOI <http://dx.doi.org/10.1038/187869b0>.
- [11] W.L. Johnson, Bulk glass-forming metallic alloys: Science and technology, *MRS Bulletin* 24 (10) (1999) 42-56. DOI <http://dx.doi.org/10.1557/S0883769400053252>.

- [12] A. Inoue, Stabilization of metallic supercooled liquid and bulk amorphous alloys, *Acta Materialia* 48 (1) (2000) 279-306. DOI [http://dx.doi.org/10.1016/S1359-6454\(99\)00300-6](http://dx.doi.org/10.1016/S1359-6454(99)00300-6).
- [13] A. Inoue, B. Shen, N. Nishiyama, Development and applications of late transition metal bulk metallic glasses, in: *Bulk Metallic Glasses*, Springer US, (2008) 1-25. DOI http://dx.doi.org/10.1007/978-0-387-48921-6_1.
- [14] A. Peker, W.L. Johnson, A highly processable metallic glass: $Zr_{41.2}Ti_{13.8}Cu_{12.5}Ni_{10.0}Be_{22.5}$ *Applied Physics Letters* 63 (17) (1993) 2342-2344. DOI <http://dx.doi.org/10.1063/1.110520>.
- [15] C.C. Hays, J. Schroers, W.L. Johnson, T.J. Rathz, R.W. Hyers, J.R. Rogers, M.B. Robinson, Vitrification and determination of the crystallization time scales of the bulk metallic-glass-forming liquid $Zr_{58.5}Nb_{2.8}Cu_{15.6}Ni_{12.8}Al_{10.3}$, *Applied Physics Letters* 79 (11) (2001) 1605-1607. DOI <http://dx.doi.org/10.1063/1.1398605>.
- [16] C.C. Hays, J. Schroers, U. Geyer, S. Bossuyt, N. Stein, W.L. Johnson, Glass forming ability in the Zr-Nb-Ni-Cu-Al bulk metallic glasses, *Journal of Metastable and Nanocrystalline Materials* 8 (2000) (2000) 103-108. DOI <http://dx.doi.org/10.4028/www.scientific.net/MSF.343-346.103>
- [17] C.C. Hays, W.L. Johnson, Undercooling of bulk metallic glasses processed by electrostatic levitation, *Journal of Non-Crystalline Solids* 250 (2) (1999) 596-600. DOI [http://dx.doi.org/10.1016/S0022-3093\(99\)00139-8](http://dx.doi.org/10.1016/S0022-3093(99)00139-8).
- [18] X.H. Lin, W.L. Johnson, Formation of Ti-Zr-Cu-Ni bulk metallic glasses, *Applied Physics Letters* 78 (11) (1995) 6514-6519. DOI <http://dx.doi.org/10.1063/1.360537>.
- [19] T. Terry, G. Tim, History of additive manufacturing, Wohlers Report Wohlers Associates, Inc. <https://wohlersassociates.com/>.
- [20] K.V. Wong, A. Hernandez, A review of additive manufacturing, *ISRN Mechanical Engineering* (2012). DOI <http://dx.doi.org/10.5402/2012/208760>.
- [21] M. Vaezi, H. Seitz, S. Yang, A review on 3D micro-additive manufacturing technologies, *The International Journal of Advanced Manufacturing Technology* 67 (5) (2013) 1721-1754. DOI <http://dx.doi.org/10.1007/s00170-012-4605-2>.
- [22] R.M. Miranda, G. Lopes, L. Quintino, J.P. Rodrigues, S. Williams, Rapid prototyping with high power fiber lasers, *Materials & Design* 29 (10) (2008) 2072-2075. DOI <http://dx.doi.org/10.1016/j.matdes.2008.03.030>.

- [23] ASTM F2792-12a, "Standard terminology for additive manufacturing technologies," ASTM International, West Conshohocken, PA, 2012. DOI <http://dx.doi.org/10.1520/F2792-12A>.
- [24] M. He, K. Song, H. Mo, J. Li, D. Pan, Z. Liang, Progress on photosensitive resins for 3D printing, *Journal of Functional Polymers* 28 (2015) 102-108. DOI <http://dx.doi.org/10.14133/j.cnki.1008-9357.2015.01.018>.
- [25] M. He, Y. Zhao, B. Wang, Q. Xi, J. Zhou, Z. Liang, 3D printing fabrication of amorphous thermoelectric materials with ultralow thermal conductivity, *Small* 11 (44) (2015) 5889-5894. DOI <http://dx.doi.org/10.1002/sml.201502153>.
- [26] G. Tapia, A. Elwany, A review on process monitoring and control in metal-based additive manufacturing, *Journal of Manufacturing Science and Engineering* 136 (6) (2014) 060801. DOI <http://dx.doi.org/10.1115/1.4028540>.
- [27] W.E. Frazier, Metal additive manufacturing: a review, *Journal of Materials Engineering and Performance* 23 (6) (2014) 1917-1928. DOI <http://dx.doi.org/10.1007/s11665-014-0958-z>.
- [28] J.P. Kruth, A.P. Mercelis, A.J. Van Vaerenbergh, A.L. Froyen, A.M. Rombouts, Binding mechanisms in selective laser sintering and selective laser melting, *Rapid Prototyping Journal* 11 (1) (2005) 26-36. DOI <http://dx.doi.org/10.1108/13552540510573365>.
- [29] X. Gong, T. Anderson, K. Chou, Review on powder-based electron beam additive manufacturing technology, *Manufacturing Review* 1 (2014) 507-515. DOI <http://dx.doi.org/10.1051/mfreview/2014001>.
- [30] S. Kumar, J.P. Kruth, Composites by rapid prototyping technology, *Materials & Design*, 31 (2) (2010) 850-856. DOI <http://dx.doi.org/10.1016/j.matdes.2009.07.045>.
- [31] H. Sun, Microstructure evolution of bulk metallic glasses via laser processing Doctoral dissertation, The Ohio State University (2010).
- [32] Y.Y. Zhang, X. Lin., L.L. Wang, L. Wei, F.G. Liu, W.D. Huang, Microstructural analysis of Zr55Cu30Al10Ni5 bulk metallic glasses by laser surface remelting and laser solid forming *Intermetallics* 66 (2015) 22-30. DOI <http://dx.doi.org/10.1016/j.intermet.2015.06.007>.

- [33] S. Pauly, L. Löber, R. Petters, M. Stoica, S. Scudino, U. Kühn, J. Eckert, Processing metallic glasses by selective laser melting, *Materials Today* 16 (1) (2013) 37-41. DOI <http://dx.doi.org/10.1016/j.mattod.2013.01.018>.
- [34] B. Li, Z.Y. Li, J.G. Xiong, L. Xing, D. Wang, Y. Li, Laser welding of $Zr_{45}Cu_{48}Al_{17}$ bulk glassy alloy, *Journal of Alloys and Compounds* 413 (1-2) (2006) 118-121. DOI <http://dx.doi.org/10.1016/j.jallcom.2005.07.005>.
- [35] J.H. Kim, C. Lee, D.M. Lee, J.H. Sun, S.Y. Shin, J.C. Bae, Pulsed Nd: YAG laser welding of $Cu_{54}Ni_6Zr_{22}Ti_{18}$ bulk metallic glass, *Materials Science and Engineering: A* 449 (2007) 872-875. DOI <http://dx.doi.org/10.1016/j.msea.2006.02.323>.
- [36] G. Wang, Y.J. Huang, M. Shagiev, J. Shen, Laser welding of $Ti_{40}Zr_{25}Ni_3Cu_{12}Be_{20}$ bulk metallic glass, *Materials Science and Engineering: A* 541 (2012) 33-37. DOI <http://dx.doi.org/10.1016/j.msea.2012.01.114>.

VITA

Yiyu Shen was born in Jiashan, Zhejiang, China. He received his Bachelor of Science degree in Mechanical Engineering in June 2009 from China Jiliang University, Hangzhou, China. In 2012, he received his Master of Science degree in Mechanical Engineering from University of Liverpool, Liverpool, United Kingdom. In May 2018, he received his Doctor of Philosophy in Mechanical Engineering from Missouri University of Science and Technology, Rolla, Missouri, USA. He won: the first place award for the poster presentation entitled '*A novel foil based additive manufacturing technology for metal parts*' at the 10th Intelligent System Center (ISC) poster presentation in 2014, November; the first place award for the poster presentation entitled '*Mechanical Properties and Surface Finish Improvement for Metal Parts Fabricated by the Foil-Based AM Technology*' at the 11th ISC poster presentation in 2015, November; the second place award for the poster presentation entitled '*Additive Manufacturing of Metallic Glass Structures*' at the 12th ISC poster presentation in 2016, November; the first place award for the research entitled '*The evolution of crystallization in laser welding of metallic glass*' at the 10th ISC research symposium in 2017, April. During his Ph.D. study, he authored four journal papers and one conference papers. Also, he co-authored four journal papers and two conference papers. Yiyu Shen also co-authored two patents during his Ph.D. study.